The Dissertation Committee for Robert Jason Scharff
certifies that this is the approved version of the following dissertation:

Adsorbate Interactions at Organic/Metal Interfaces

Committee:

Alan Campion, Supervisor

Jennifer S. Brodbelt

Charles B. Mullins

John F. Stanton

David A. Vanden Bout

Adsorbate Interactions at Organic/Metal Interfaces

by

Robert Jason Scharff, B.S., M.S.

DISSERTATION
Presented to the Faculty of the Graduate School of
The University of Texas at Austin
in Partial Fulfillment
of the Requirements
for the Degree of

DOCTOR OF PHILOSOPHY

THE UNIVERSITY OF TEXAS AT AUSTIN
May 2005

To my loving wife, Jackie.

Acknowledgments

I wish to thank the multitudes of people who helped me. I am certainly appreciative that those who been associated with me over these many years have been able to over-look or tolerate my undying fascination with pessimism and skepticism. I am sure I have frustrated you all to your wits end and then back again. This has been quite a long journey for me and I certainly owe a tremendous amount of gratitute to my graduate advisor, Professor Alan Campion. Professor Campion, unlike many others, allows his students to find their own way and develop their own intuition and independence. Often, I have wondered whether this approach is the best way, but now, I think I have seen the proverbial "light". Scientific discovery is exactly what it is – discovery – and having scientific phenomena demonstrated is far less satisfying than making the discovery on your own.

I would also like to ackowledge Professor John T. Yates, Jr., my first graduate advisor while I was at the University of Pittsburgh. Although we may have parted on less than amicable terms, I have appreciated and made signicant use of the approach that you take towards solving scientific problems. Perfection may not be obtainable, but it should certainly be the goal.

My collegue in the Department, Brad Flowers, has a very bright future ahead. Although tragedy made a feable attempt to derail his scientific plans, he rebounded with the grace of Bird, and has become arguably the most productive student in the Department under the supervision of Professor John F. Stanton. I have great amount of respect for Brad both personally and professionally. His interests in science and life are boundless and I aspire to have his enthusiasm for both.

I thank Don Perry, a post doctoral fellow in our group for a while, for the much needed help in the early days of the HREELS experiments. As many know or will come to find out, UHV science is not for the faint at heart and often demands long hours and lots of elbow grease just to get things to turn on. You always entertained many of my hair-brained ideas. My fellow graduate students, Greyhm and Michelle, are the most deserving of my gratitude since they must bear the brunt of my daily rant on science, golf, or politics. Best of luck and much happiness is wished upon you in the days to come.

Outside of the Chemistry Department, there are many friends and family members that have always been supportive and offerered a tremendous amount of encouragement expecially when there seemed to be no end in sight for me. Of course, I would not be here today without my mother, Marsha Parsons Jameson, and my father and step-mother Davis and Peggy Scharff. All of you have encouraged me to no end to walk on my own path and set my goals as high as possible. Let this manuscript be a small token of my love and gratitude for you all and hopefully the best has yet to come for me.

And finally, to my wife Jackie, I truly do not know where I would be or who I would be without your unwavering love, support, and steadfast resolve.

I can not begin to express what you mean to me and I would almost certainly be lost in the great big world without you.

Adsorbate Interactions at Organic/Metal Interfaces

Publication No. __________________

Robert Jason Scharff, Ph.D.
The University of Texas at Austin, 2005

Supervisor: Alan Campion

The vibrational and electronic structure of 2-12Å thick films of pyromellitic dianhydride (PMDA) adsorbed on clean and H_2O pre-covered Cu(111) surfaces have been measured at 110K and 295K using high resolution electron energy loss spectroscopy (HREELS) and surface Raman spectroscopy. On both surfaces at low temperature, the adsorption geometry favors a flat-lying orientation. Adsorption at 295K results in an upright orientation that is consistent with previous accounts in the literature. The adsorption at 110K leads to the now well documented ring-opening reaction of one of the anhydride groups producing a carboxylate and carbonyl species, whereas, at room temperature CO is lost to the gas phase. The presence of pre-adsorbed H_2O at 110K results in a hydrogen bonded complex with the carboxylate group, dramatically altering the electronic structure of the PMDA film. Surface Raman scattering experiments of the H_2O-PMDA co-adsorbate complex exhibit resonant scattering behavior that is attributed to the so-called "first layer"

or “chemical” SERS effect due to dynamical charge transfer excitations on “atomically smooth” Cu(111) at 110K.

Table of Contents

List of Tables

List of Figures

Chapter 1

Introduction

The seminal work of Fleischman [1] in 1974 provided the first experimental observation of an enhanced Raman scattering spectrum from molecules adsorbed on a metal electrode surface. The surface-enhanced Raman scattering (SERS) spectrum of pyridine adsorbed on a roughened silver electrode was attributed to the large increase in the electrode surface area (due to successive oxidation-reduction cycles), hence increasing the number of adsorbed molecules sampled in the experiment. Jeanmaire and Van Duyne [2, 3] and Albrecht and Creighton [4] later reported Raman intensities for pyridine adsorbed on roughened silver electrodes to be about a factor of 10^6 times greater than the Raman spectrum for pyridine in solution. It was soon realized that substrate morphology was a crucial aspect for SERS since only nonplanar surfaces exhibited sufficient SERS intensity [4–7].

However, it was also recognized that the large enhancement of the Raman intensities could not be accounted for solely on the basis of the number of adsorbed scatterers. These early findings started the debate regarding the nature of the SERS enhancement mechanism. The work of Jeanmaire and Van Duyne [2, 3] proposed an electric field enhancement mechanism whereas the work of Albrecht and Creighton speculated on the formation of hybrid molecular electronic states due to intimate interactions between the adsorbate and the substrate. The work of Pettinger et al. [8, 9] seemed to support the latter mechanism with regards to pyridine adsorption on "atomically smooth" Ag(111) or Ag(100) surfaces. The fact that the silver surfaces were planar ruled out the possibility that the observed SER spectra were due to optically excited surface plasmons of the substrate and pointed towards the importance of the metal-adsorbate bonding interactions.

Over the years, two distinct models for SERS have been developed which are classified as an "electromagentic" (EM) and "chemical" or "charge-transfer" (CT) mechanism. The former is associated with surface morphology via the optical excitation of the surface plasmon resonance of a metal substrate leading to large electromagnetic fields at the interface. Surface plasmons are, by definition, the collective excitation of the electron gas confined to the near-surface region of a conducting substrate. Surface plasmons may propagate along the surface, as is the case for gratings, or may be localized on the surface, as is the case for a spherical particle. Generally, the EM mechanism is described by the problem of the metal sphere in an applied, external electric field. For a spherical particle whose radius is much smaller than the wavelength of light, the electric field is uniform across the surface of the sphere and static. Thus, within the Raleigh approximation, the field induced at the surface of the metal sphere is related to the external potential by the expression

$$E_{induced} = E_{external} \frac{\varepsilon_1(\omega) - \varepsilon_2}{\varepsilon_1(\omega) + 2\varepsilon_2} \tag{1.1}$$

where $\varepsilon_1(\omega)$ is the frequency-dependent dielectric function of the metal and ε_2 is the dielectric constant of the surrounding media. Obviously, a resonant condition is obtained at $\Re(\varepsilon_1(\omega)) = -2\varepsilon_2$. The excitation of the surface plasmon will increase the local electric field experienced by any molecule adsorbed at the surface of the sphere. This has been conceptualized as a localized dipolar field centered on the metal sphere which decays away from the surface in all directions according to the dipole decay law. The sphere enhances both the external applied field and the Raman scattered field with the total enhancement proportional to $E^4 = E^2_{external}E^2_{Raman}$ [10].

A second mechanism operating independently from the EM contribution is based on the formation of adsorption induced electronic resonances. The SER spectrum is thought to arise from a resonance in the *effective* polarizability of the molecule-metal adsorption complex, and it is sensitive to the presence of "active sites" on the metal surface and the nature of the bonding interactions between the adsorbate and substrate [11–13]. The concept of the "charge-transfer" (CT) excitation was invoked in the experimental work by Demuth and Sanda [14] who identified a CT excitation using electron energy loss spectroscopy (EELS) for pyridine adsorbed on Ag(111) in ultrahigh vacuum. In addition to a weakly perturbed molecular state, a new, broad onset electronic excitation feature was observed near 1.9 eV for chemisorbed pyridine and attributed to a metal-molecule CT excitation [14]. The observation of the 1.9 eV CT excitation by EELS was argued to be directly related to SERS since the excitation of this new metal-molecule state could enhance the *effective* polarizability of the adsorption complex [14].

Otto [11, 15] has long held the position that SERS cannot be supported on "atomically smooth" surfaces and that atomic scale roughness (ASR) is necessarily required for strong Raman enhancement. Otto distinguishes between ASR and the roughness features that produce the giant EM enhancement, however, it is not clear what minumum size is required to produce the EM enhancement effect. The so-called "adatom–charge-transfer" model was believed to enhance the surface Raman scattering by increasing the magnitude of the three matrix elements of the Raman cross-section of the adsorbed molecule in the expression

$$\sigma(\omega_v) \propto \sum_{ij} \frac{\langle 0|H_{e-p}|j\rangle\langle 1,j|H_{ev}|0,i\rangle\langle i|H_{e-p}|0\rangle^2}{(\omega_L-\omega_v-\omega_j)(\omega_L-\omega_i)} \tag{1.2}$$

where H_{ev} describes the interaction between the metal electrons and the adsorbate vibration with frequency ω_v, and H_{e-p} describes the electron-photon interaction term $e(\boldsymbol{pA}+\boldsymbol{Ap})/2mc$. Otto argues that H_{e-p} is increased due to additional momentum available for scattering electron-hole pairs at ASR. Also, the H_{ev} term is argued to be increased due to the "relaxation of momentum conservation by the presence of the adatom to which the adsorbate is bound" [11, 15]. Simply put, the ASR creates additional electron-hole pairs and couples the excited electrons to the vibrations of the adsorbate.

The electron-hole pair mechanism is now generally replaced with the concept of "active sites" on the surface that are capable of forming a charge-transfer complex ($\mathrm{M^+L^-}$; M $\equiv$ metal atom(s) and L $\equiv$ surface ligand) such that adsorption leads to the creation of new states in resonance with the exciting photon. The formation of the CT complex is regarded as the “chemical” contribution to SERS.

Past work in our group [16–20] has demonstrated the existence of SERS-CT by the “chemical” mechanism for pyromellitic dianhydride (PMDA) chemisorbed on “atomically smooth” copper and silver surfaces. A very narrow and intense CT excitation was observed using EELS at 1.9 eV for PMDA adsorbed on Cu(111) below 120K and was attributed to a molecule-to-metal charge-transfer excitation [16–20]. Frequency dependent surface Raman scattering experiments exhibited resonance Raman scattering behavior at 647 nm and was argued to be due only to the chemical contribution to SERS as a result of a photon induced charge hopping (dynamical) process between the metal substrate and chemisorbate. It is now speculated that co-adsorbed water played a significant role in in the previously observed optical and electronic spectra.

Recent criticism by Otto [21] has re-kindled the controversy regarding the “chemical” contribution to SERS for molecules adsorbed on flat or “atomically smooth” metal surfaces. Otto has vehemently argued against the existance of a contribution to SERS from a “chemical” effect due to dynamical charge-transfer (DCT) at a smooth surface. Instead, the so-called “first layer” SERS phenomenon can occur if the DCT process comes before or after an elastic electron scattering event at sites of ASR [21]. He proposes that the interaction of adsorbed molecules with metal electrons is detrimental to

Raman scattering from surfaces. Up to this point, the previous work in our group did not focus on the role of adatoms or (foreign) molecules.

The motivation of the work detailed in the present manuscript is to provide evidence of the existence of the SERS-CT mechanism by “chemical” enhancement for PMDA adsorbed on “atomically smooth” Cu(111) and Ag(111). I demonstrate that the CT excitation associtated with chemical enhancement is due to interactions between water, PMDA, and the substrate, using high-resolution electron energy loss spectroscopy (HREELS). I show that temperature dependent adsorption geometry changes are important features associated with the PMDA electronic structure on clean and H_2O pre-covered surfaces. These experiments demonstrate that the SERS intensity for adsorbed PMDA is analogous to molecular resonance Raman scattering from chemisorbed PMDA radical anion formed only in the presence of the electron donating solvents H_2O and pyridine.

Quantum chemical calculations via density functional methods are used to understand the chemical and electron properties associated with neutral and radical anions of PMDA. The electronic structure calculations of H_2O adsorbed on small copper clusters qualitatively predict the decrease in the surface work function of the Cu(111) surface due to the adsorption of H_2O. I show that changes in the energetic position of the HOMO of cluster model for the H_2O/Cu(111) surface becomes higher in energy than the LUMO of gas-phase PMDA and suggests that H_2O co-adsorption promotes substrate-mediated CT into the LUMOs of adsorbing PMDA molecules to form radical anions of chemisorbed PMDA during the adsorption process. It is argued that PMDA adsorption in the presence of co-adsorbed H_2O or pyridine forms a stable CT complex with the substrate due to electron donation mediated by those substrate atoms interacting with chemisorbed PMDA molecules. It is also argued that the observed electronic CT excitation and SER spectra are likely due to an intra-molecular electronic excitation of the stable surface anion, $C_{10}H_2O_6^-$.

Chapter 2

Experimental Methods

2.1 Auger Electron Spectroscopy.

2.1.1 The Auger Process

Elemental analysis of the surface is obtained by Auger electron spectroscopy (AES). The Auger transition is induced by directing a primary beam of high energy electrons (1-5 keV) towards the sample surface and collecting the spectrum of backscattered electrons. In the excitation process, the primary beam excites an atom in the substrate to a high ionic state by removing an electron from a stable core level state, e.g., the 1s shell with binding energy E_{1s}. An electron from a less tightly bound level, e.g., the 2s shell with binding energy E_{2s}, preferentially fills the core hole by a radiationless process and the excess energy from the relaxation transition causes the emission of a second electron, the Auger electron, from another, less tightly bound state, e.g., the 2p shell with binding energy E_{2p}. Energy conservation stipulates that the kinetic energy of the outgoing electron is,

$$E_{kin} = E_{1s} - E_{2s} - E_{2p} - e\phi \tag{2.1}$$

where ϕ is defined as the work function of the surface [22]. The core-hole decay process is illustrated schematically in Figure 2.1.

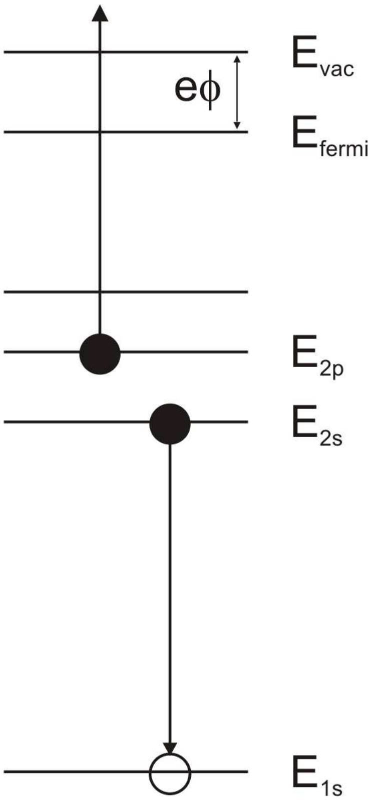

Figure 2.1: Schematic representation of the Auger core-hole decay process.

The backscattered electrons, ejected with an energy distribution $N(E)$, include the elastic peak of the primary beam plus electrons that have undergone an Auger transition. In addition, emission of secondary electrons that have undergone multiple inelastic events contributes to the broad tail of the experimental signal near a kinetic energy of zero. The distribution, $N(E)$ are energy analyzed by a retarding field analyzer (RFA) or cylindrical mirror analyzer (CMA), the latter illustrated schematically in Figure 2.2.

The CMA consists of three concentric electrostatic deflectors with the

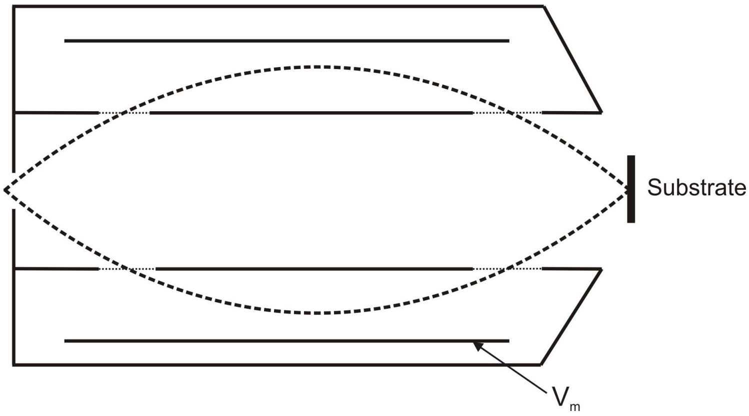

Figure 2.2: Illustration of the cylindrical mirror analyzer (CMA).

innermost and outermost held at ground potential. The intermediate cylinder has an applied negative potential, V_m, for deflecting Auger electrons through grid-covered openings in the side of the inner cylinder, forcing these electrons back through openings at the rear of the inner cylinder where they are collected by a channeltron electron multiplier. The deflection of the electrons by the intermediate cylinder is dependent on the kinetic energy of the electrons and the applied negative potential, V_m. Thus, the kinetic energy of the electrons collected can be controlled by the potential, V_m. Because the Auger peaks in the $N(E)$ vs. E spectrum are superimposed on a large, continuous background, the derivative, $dN(E)$ vs. E, spectrum provides a better way of detecting the peaks. This is accomplished electronically by a lock-in amplifier. The lock-in amplifier provides a small AC modulation (kHz) to the DC sweep voltage of V_m [23]. The AC signal detected at the channeltron has a superimposed DC component which is removed. The lock-in amplifier phase matches the AC signal and the derivative spectrum is directly detected.

2.1.2 Mean Free Path

The peak-to-peak height of the derivative lineshape for a given atomic transition is directly proportional to the concentration of atomic species in the near surface region of the sample. By accounting for the relative transition sensitivities [22], AES provides quantitative information on the chemical concentrations at the surface. Thus the most common use of AES in surface science is to monitor the cleanliness of the surface. The problem with quantitative analysis is the dependency of the escape depth of the Auger electron on the nature of the surrounding matrix. For an electron originating from within the solid, the electron escape depth corresponds to a distance below the surface, λ_e, where the intensity of the emitted electron is $1/e$ of the original intensity. Thus, the Auger electron intensity follows the law,

$$I = I_0 e^{-l/\lambda_e} \tag{2.2}$$

where l is defined as the distance below the surface for the excited atom that emits an Auger electron. The dominant factor that results in the attenuation of the Auger signal is energy loss to valence band excitations [24]. For this reason, the escape depth is determined primarily by the valence band structure of the solid. A plot of the variation of the electron escape depth as a function of electron kinetic energy is shown in Figure 2.3. From the figure, it is seen that the escape depth is roughly independent of the material, and this curve is called the universal curve.

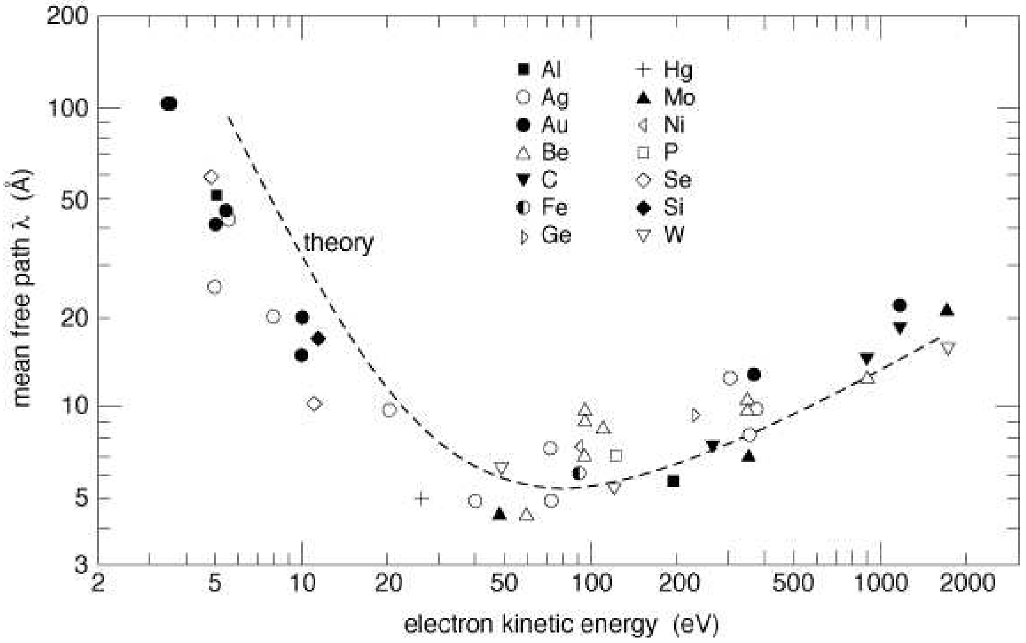

Figure 2.3: The universal curve demonstrating the variation of the electron mean free path with electron kinetic energy. Reproduced from reference [22].

Beginning at kilovolt energies, the escape depth decreases for decreasing electron energy to a minimum at ≈ 70 eV and then increases again. The energy minimum corresponds roughly to the energy maximum for the ionization cross-section of most gases [24]. A theoretical interpretation to the experimental data has been provided by Penn [25]. He concluded that the primary cause of the electron mean free path attenuation is due to inelastic scattering from valence band electrons via plasmon excitations. The minimum of the curve corresponds to the electron energy that most effectively couples to the plasma frequency of the material. At energies less than 70 eV, coupling to the plasma frequency becomes less efficient which causes a reduction in the inelastic scattering cross-section and increases the electron mean free path in the solid.

2.2 High Resolution Electron Energy Loss Spectroscopy.

High resolution electron energy loss spectroscopy (HREELS) is an extremely powerful technique capable of probing not only atomic and molecular vibrations at surfaces, but also exploring the underlying electronic structure of the interface. An incident electron of energy E_i may excite vibrational normal modes of adsorbed molecules with energy $h\nu_0$ before being backscattered into the vacuum with energy E_s. Because energy must be conserved, the collected backscattered electrons exit from the surface with an energy given by the following simple expression for each excited mode

$$E_s = E_i - h\nu_0 \tag{2.3}$$

having lost discrete amounts of energy to the surface-adsorbate complex. Analysis of the energy losses provides direct information regarding the vibrational frequencies of atoms and molecules at the surface. Energy gain features ($E_s = E_i + h\nu_0$) may also be observed if there is a sufficient population in vibrationally excited states.

In order to study the vibrational motion of adsorbed atoms and molecules by electron energy loss spectroscopy, one requires sufficient energy resolution in order to probe such motions since the natural line width of an adsorbed molecule is typically 0.5-1 meV [26]. Because HREELS uses electrons as the excitation “pump” as well as the “probe” that carries information regarding the surface to the analyzer, the electron beam must be highly monochromatic and the analyzer must have the capability to resolve energies of only a few millivolts. The formation of a monochromatic beam of electrons is accomplished by using electrostatic deflectors. The HREEL spectrometer utilizes tandem 127° cylindrical deflectors for monochromating the incident electron beam and a second pair for analyzing the elastically and inelastically scattered electrons that exit from the surface.

2.2.1 The 127° Cylindrical Deflector

To understand how focusing of low energy electrons is achieved, the trajectory of a charged particle in the presence of a uniform cylindrical electric field must be considered. An electron of mass m, velocity v, and charge q in a deflecting field, $\boldsymbol{E_r}$, travels in a circle along a central path $\boldsymbol{r}$ within the deflecting device if the centrifugal force and the deflecting force balance. This occurs when

$$\frac{mv^2}{\boldsymbol{r}} = q\boldsymbol{E_r} \tag{2.4}$$

where $\boldsymbol{r}$ is the radius of the central path and $\boldsymbol{E_r}$ is the radial electric field produced by two cylindrically parallel plates, with an inner plate of radius r_1, an outer plate of radius r_2, and the so-called main path denoted r_0. Figure 2.4 provides a pictorial representation.

The potential difference between the two plates is just

$$\Delta V = V(r_1) - V(r_2) \tag{2.5}$$

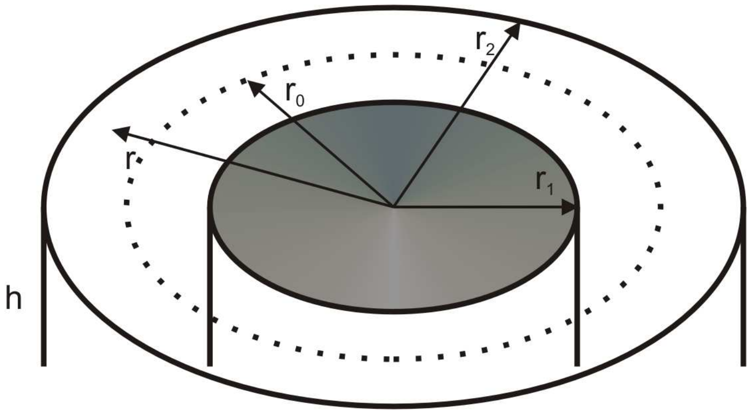

Figure 2.4: Illustration of cylindrically parallel plate conductors.

where

$$V(r_2) = -\frac{q}{2\pi h}\ln r_2 + constant \tag{2.6}$$

and

$$V(r_1) = -\frac{q}{2\pi h}\ln r_1 + constant \tag{2.7}$$

are potentials of the outer and inner plates by the relation

$$V(\boldsymbol{r}) = -\frac{q}{2\pi h}\int \frac{dr}{\boldsymbol{r}} \tag{2.8}$$

with h defined as the height of the cylinder. Thus, the potential difference, ΔV, is given by

$$\Delta V = -\frac{q}{2\pi h}\ln\frac{r_2}{r_1} \tag{2.9}$$

and since the potential at any point between r_1 and r_2 is just

$$V(\boldsymbol{r}) = -\frac{q}{2\pi h}\ln \boldsymbol{r} + constant, \tag{2.10}$$

it then follows that at $V(r_0) = 0$,

$$V(\boldsymbol{r}) = \frac{\Delta V}{\ln(r_2/r_1)} \ln \frac{\boldsymbol{r}}{r_0}, \tag{2.11}$$

where r_0 is the radius of the path where $V(r_0) = 0$. Now consider an electron traveling along the path r_0 with kinetic energy E_0. The radial electric field produced inside the cylinder is given by the expression

$$\boldsymbol{E_r} = -\frac{\delta V(\boldsymbol{r})}{\delta r} = \frac{1}{r} \frac{\Delta V}{\ln(r_2/r_1)}. \tag{2.12}$$

Combining equations 2.4 and 2.12, the kinetic energy of the electron, E_0, is given by

$$E_0 = \frac{1}{2} \frac{q \Delta V}{\ln(r_2/r_1)}. \tag{2.13}$$

Therefore it is seen that a linear relationship exists between the difference potential ΔV of the cylindrical deflecting device and the energy E_0 of the main path.

Several devices exist for the purpose of electron energy analysis such as the parallel plate deflector, the 180° spherical deflector, and the 127° cylindrical deflector. Our instrument is based on the 127° cylindrical deflector which is depicted in Figure 2.5.

In order to demonstrate the optimal transmission of current through such such a device, it is necessary to describe the trajectories of the electrons between the deflecting plates. The equation of the electron trajectory is [27]

$$y = y_1 \cos\left(\sqrt{2}\frac{x}{r}\right) + r\frac{\delta E}{2E_0}\left(1 - \cos\left(\sqrt{2}\frac{x}{r}\right)\right) + \frac{r\alpha}{\sqrt{2}} \sin\left(\sqrt{2}\frac{x}{r}\right) + \\ r\alpha^2 \left(\frac{2}{3}\cos\left(\sqrt{2}\frac{x}{r}\right) - \frac{7}{24}\cos\left(2\sqrt{2}\frac{x}{r}\right) - \frac{3}{8}\right) \tag{2.14}$$

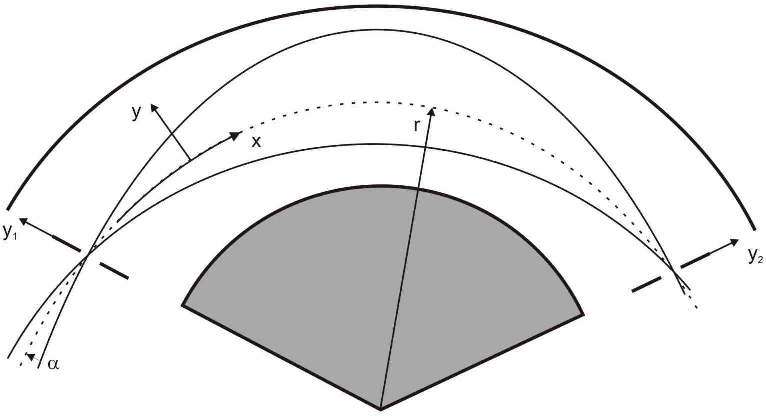

Figure 2.5: The 127° cylindrical deflector.

where y_1 is the radial deviation of the electron at a selected point upon in the device, α is the angle between the trajectory and the central path, r, at the same point. The difference between the electron energy and the pass energy E_0 is defined at δE. Letting x be defined as the distance from the selected point to the point on the central path, and letting y be defined as the radial deviation of the electron trajectory perpendicular to the main path, it is found that first-order focusing is obtained when the term linear in α vanishes. This requires that the length of the central path be

$$x_f = \frac{r\pi}{\sqrt{2}}, \tag{2.15}$$

which is the equivalent of having a deflection angle of $\frac{\pi}{\sqrt{2}} \cong 127^\circ$. For this angle, Equation 2.14 simplifies to the following when $x = x_f$,

$$y_2 = -y_1 + r\frac{\delta E}{E} - \frac{4}{3}r\alpha^2, \tag{2.16}$$

where y_2 is the deviation from the central path at a distance x_f downstream.

Therefore, an electron at y_1 is imaged at y_2 with a magnification of -1 when δE and α are both zero. The position of the image depends on the energy deviation δE which makes the system energy resolving.

A condition exists that results in a lower than theoretically predicted resolution. For example, electron focusing results in a spatial broadening of the beam due to repulsive Coulombic forces between the particles as the density of the beam increases. This is known as the space-charge effect. The transmitted current through the monochromator at a given resolution is the greatest restriction on the capability of the HREEL spectrometer since it ultimately determines the amount of detected signal. The full theoretical treatment [26] of electron trajectories under the influence of space-charge effects has been provided elsewhere.

2.2.2 Surface Selection Rule

The principle mechanism by which an incident low energy electron loses energy to the surface-adsorbate complex is through the long range interaction with the surface electric field and dynamic dipole moment of the adsorbate. The dipole moment, $\mu(\boldsymbol{x})$, is time dependent due to the nuclear motions of adsorbate and substrate atoms and may be expanded in terms of the displacement, $\boldsymbol{x}$, from the equilibrium separation as shown in Equation 2.17,

$$\mu(\boldsymbol{x}) = \mu_0 + \frac{d\mu}{dx}\boldsymbol{x} + \ldots \tag{2.17}$$

The transition moment between initial state n and final state n' is

$$\mu_{nn'} = \int \Psi^*_{n'} \mu(\boldsymbol{x}) \Psi_n d\tau. \tag{2.18}$$

Since μ_0 is a constant in the expansion of Equation 2.17, the first term in the integral of Equation 2.18 vanishes if $n{\neq}n'$ due to the orthogonality of the wavefunctions Ψ_n and Ψ'_n within the harmonic-oscillator approximation. Evaluation of the second term in the integration of Equation 2.18 does not vanish due to the orthogonality property of the Hermite polynomials if $n = n' + 1$. This result leads to the selection rule for vibrational transition within the harmonic oscillator approximation $\Delta n = \pm 1$. Furthermore, the factor $\left(\frac{d\mu}{dx}\right)_0$ implies that the dipole moment of the molecule must change during a vibration, i.e. it is dynamic, and thus is called the *dynamic dipole moment.*

Because the relative parallel momentum transfer from the initial state to the final state is small compared to the initial momentum of the incident particle, dipole scattering is peaked very near the specular (elastically scattered) direction with a deflection angle of $\approx h\nu/2E_i$ [26] away from the specularly reflected beam. Due to the dipolar nature of the interaction, the same selection rules for vibrational excitation in infrared spectroscopy applies to HREELS; the probability of excitation is given by the square of the transition dipole matrix element [22, 26, 28],

$$\left| \langle \Psi_f | \boldsymbol{\mu} \cdot \boldsymbol{E} | \Psi_i \rangle \right|^2 \tag{2.19}$$

where Ψ_f and Ψ_i are the time-dependent wavefunctions expressed as linear combinations of the probe electron wavefunction and the adsorbate vibrational wavefunction for the final and initial states, respectively, and $\boldsymbol{\mu}\cdot\boldsymbol{E}$ is the interaction potential between the incident electron and adsorbate complex. Therefore, the dipole selection rule can be stated as: *only those vibrations that transform as totally symmetric representations in a given surface point group representation are allowed transitions.* Since the parallel electric field vector of the probe electron lies in the plane of the surface, its projection is canceled out by the image potential it creates within the surface and it will therefore not couple to a surface vibration. Thus, for a molecule adsorbed on a surface, the only vibrational modes that can be observed will be those that have a dynamic dipole moment that projects a component along the surface normal.

2.2.3 Impact Scattering

In this section, the important features of impact scattering are discussed. From the previous discussion it was shown that a portion of the electrons in the primary beam undergo an inelastic process due to long range dipolar interactions with the adsorbate before being reflected from the surface at small angles away from the specularly reflected beam. However, the electrons that impact the surface without interacting with the dipole field encounter surface atoms that are not in their ideal equilibrium positions due to the time varying thermal motion of the atoms. This causes some electrons to emerge from the surface at large angles creating a diffuse thermal background. Consequently, these electrons may undergo multiple scattering events before emerging from the surface. The scattering is inelastic because the electron has lost (or gained) a vibrational quantum to (or from) the surface. A full theoretical treatment has not been developed that can describe in simple terms the origin of large angle inelastic scattering.

In light of the theoretical shortcomings, certain characteristics exist that distinguish between the impact scattering regime and the dipole scattering regime. Ibach [26] has shown that the energy dependence of the impact scattering cross-section has an oscillatory structure as well as an angular dependence, while the dipole scattering cross-section follows a monotonically rising function with increasing energy and is peaked near the specular direction, as discussed previously. The selection rule for impact scattering is not as specific as the dipole selection rule. The selection rule for impact scattering allows both parallel and perpendicular modes to be excited. Furthermore, it is a characteristic that multiple losses and overtone excitations are enhanced in the impact scattering regime.

A particular case of impact scattering occurs when electrons are inelastically scattered from molecules via a "resonance" process. Such a process involves the electron capture by an adsorbed molecule into an empty molecular orbital to form a temporary negative ion [29]. Characteristics of the negative ion resonance formation are short lifetimes on the order $10^{-13} - 10^{-16}$ sec, a distinct energy dependence in the scattering cross-section, generally observed as a sharp peak in the energy distribution over a width of several eV, an angular dependence to the scattered electrons that reflects the symmetry of the orbital involved in the resonance, and an enhanced probability for vibrational overtone excitation.

2.2.4 Instrumentation

Many different excitations of condensed media can be studied over a wide range of energies beginning at a few tens of meV to more than 1000 eV. Energy losses in the range of 1 meV up to approximately 500 meV are primarily due to librational and vibrational transitions from either surface atoms or adsorbates. Higher energy losses in the range of 1 eV - 10 eV are generally due interband transitions of the substrate and intramolecular electronic excitations of the adsorbate. For the range of losses between 10 eV and 100 eV, these excitations generally fall into the category of surface and bulk plasmons, wheres energy losses greater than 100 eV are principally due to core-level electronic excitations.

A Leybold Heraeus ELS22 high resolution electron energy loss (HREEL) spectrometer was used for both the vibrational and low-energy electronic excitation spectra. All spectra were acquired in the specular geometry (120° total scattering angle) with a primary electron energy of 7 eV (12 eV) and an energy resolution of 7-9 meV (25-30 meV) for the vibrational (electronic) excitation spectra unless otherwise indicated.

2.3 Surface Enhanced Raman Spectroscopy.

Surface enhanced spectroscopy provides one way to probe fundamental interactions of the nanometer length scale by exploiting the chemical nature of adsorbed molecules. In particular, surface enhanced Raman scattering (SERS) has been demonstrated for many molecules adsorbed on a number of metals including Cu, Ag, Au, Pt, and Rh, under a variety of experimental conditions [10,30,31]. Two theoretical mechanisms for enhancement have been generalized; one due to an electromagnetic (em) resonances of the metal substrate (intensity enhancement factor of $10^5 - 10^6$), and the other due to a local chemical (enhancement factor of 10-100) contribution [30]. SERS-active systems in which the em effect dominate include roughened electrode surfaces, metal particles and aggregates, and cold-deposited metal films. The em mechanism should be a non-selective Raman scattering amplifier by all molecules, yet certain molecule enhancements differ by a factor of 200. The chemical contribution, due to the formation of new, hybrid electronic states arising form chemisorption, can be isolated from the em effect for molecules adsorbed on "atomically smooth" single crystal substrates [10].

2.3.1 Electromagnetic Enhancement

The electromagnetic enhancement (EM) effect for a molecule adsorbed on a flat surface is best understood as a coupling of the EM field of the incident and scattered radiation to plasmon excitations of the metal [30,32]. In general, one should begin by considering the interaction of light with the surface illustrated in Figure 2.6.

For a flat, conducting plane, the components of the electric field at the

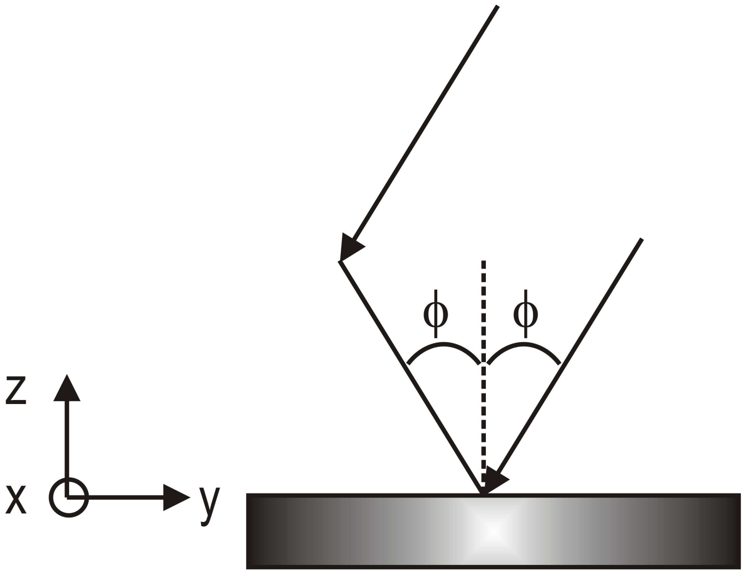

Figure 2.6: Definition of the coordinates of the incident radiation field. Reproduced from [32].

surface are

$$
\begin{aligned}
E_x &= E_{is}(1 + r_s) \\
E_y &= E_{ip}(r_p - 1)\cos\phi \\
E_z &= E_{ip}(1 + r_p)\sin\phi \qquad (2.20)
\end{aligned}
$$

where r_s and r_p are the Fresnel coefficients for reflection at the interface for s-polarized and p-polarized light, E_{is} and E_{ip} are the polarized electric field component magnitudes incident on the interface, and ϕ is the angle of incidence. The Fresnel coefficients describe the interface reflectivity and may be expressed in terms of the dielectric function ε of the metal,

$$\begin{aligned} r_s &= \frac{\cos\phi - \left(\varepsilon - \sin^2\phi\right)^{1/2}}{\cos\phi + \left(\varepsilon - \sin^2\phi\right)^{1/2}} \\ r_p &= \frac{\varepsilon\cos\phi - \left(\varepsilon - \sin^2\phi\right)^{1/2}}{\varepsilon\cos\phi + \left(\varepsilon - \sin^2\phi\right)^{1/2}} \end{aligned} \tag{2.21}$$

noting that the dielectric function $\varepsilon(\omega, \boldsymbol{k})$ depends on both frequency ω and wave vector $\boldsymbol{k}$.

Now consider light that has been scattered from the surface. The s-polarized and p-polarized components of the scattered field are given by

$$\begin{aligned} E'_p &= (1 + r'_s)p_x \\ E'_s &= p_y(1 - r'_p)\cos\phi' + p_z(1 + r'_p)\sin\phi' \end{aligned} \tag{2.22}$$

where r'_s and r'_p are the Fresnel coefficients pertaining to the light scattered at angle ϕ'. The polarized quantities p_x, p_y, and p_z given by

$$\begin{aligned} p_x &= \alpha_{xx}E_x + \alpha_{xy}E_y + \alpha_{xz}E_z \\ p_y &= \alpha_{yx}E_x + \alpha_{yy}E_y + \alpha_{yz}E_z \\ p_z &= \alpha_{zx}E_x + \alpha_{zy}E_y + \alpha_{zz}E_z \end{aligned} \tag{2.23}$$

where α_{nm} are the tensor elements of the polarizability for a particular vibrational mode. From the above equations, four intensity components are defined for a surface Raman experiment [32],

$$\begin{aligned}
I_{ss} &\propto C\Big|\alpha_{xx}(r_s+1)(r'_s+1)\Big|^2 \\
I_{sp} &\propto C\Big|\alpha_{xy}(r_p-1)(r'_s+1)\cos\phi+\alpha_{xz}(r_p+1)(r'_s+1)\sin\phi\Big|^2 \\
I_{ps} &\propto C\Big|-\alpha_{xy}(r_s+1)(r'_p-1)\cos\phi'+\alpha_{xz}(r_s+1)(r'_p+1)\sin\phi'\Big|^2 \\
I_{pp} &\propto C\Big|-(r'_p-1)\cos\phi'\left[\alpha_{yy}(r_p-1)\cos\phi+\alpha_{yz}(r_p+1)\sin\phi\right] \\
&\quad +(r'_p+1)\sin\phi'\left[\alpha_{yz}(r_p-1)\cos\phi+\alpha_{zz}(r_p+1)\sin\phi\right]\Big|^2
\end{aligned} \tag{2.24}$$

where C is defined as

$$C=(\nu_0-\nu_k)^4 \tag{2.25}$$

with ν_0 being the excitation frequency and ν_k the Raman frequency of a given vibrational mode. These equations refer to a molecule fixed with respect to the surface normal and form the basis for the Raman surface selection rules within the EM framework.

Ignoring, for the moment, the effect of the polarizability tensor, the Raman intensity is governed largely by two parameters - the scattering angles and the frequency-dependent dielectric function of the metal. It has been shown [30, 32, 33] that angles around 60° and 65° provide the most local enhancement of the radiation field thereby leading to a maximum in the Raman scattering process. The dependence of the dielectric function on the frequency of light may be described using the Drude model of a simple free-electron metal. Within this approximation, the frequency-dependent dielectric function may be expressed as

$$\varepsilon=1-\frac{\omega_p^2}{\omega^2-i\omega\gamma} \tag{2.26}$$

where γ is a damping factor associated with em energy loss in the metal and ω_p is the Drude plasmon frequency,

$$\omega_p^2 = \frac{4\pi N e^2}{m\varepsilon_0} \tag{2.27}$$

In Equation 2.27, N, e, and m are the number density, charge, and mass of the free electrons in the metal, respectively.

For most metals, $r_s \rightarrow -1$ and $r_p \rightarrow +1$ as $|\varepsilon|$ becomes very large at the red end of the visible spectrum. As a result, the tangential components of the surface field approach zero due to the cancellation of the incident and reflected fields, while the normal component is amplified by the reflected field. On the other hand, at short wavelengths $|\varepsilon| \rightarrow 0$ and $r_s \rightarrow -1$ and $r_p \rightarrow +1$. This occurs for metals like silver and to a lesser extent for copper. For these examples, the tangential field components are non-zero and become greater than the normal component at these shorter wavelengths. For Raman spectroscopy, visible light is generally used as the excitation source, thus the dielectric function is not very small and hence some of the tangential component of the surface electric field will contribute. For flat metal surfaces that are continuous over many wavelengths, plasmon resonances are generally not optically excited although the surface does modify the electromagnetic field to some extent. However, based on the em theory, the maximum *resonant* enhancement of the local field is no more than a factor of two leading to an enhancement factor of 16 in the scattered Raman intensity [30].

2.3.2 Chemical Enhancement

There is considerable experimental evidence to suggest that a second (chemical) enhancement mechanism exists independent of the em mechanism for SERS [17, 32, 34–44]. For systems where both mechanisms contribute, the effect is multiplicative [10, 30, 31]. Evidence for chemical enhancement can be found in potential-dependent electrochemical experiments. In those cases, by varying the electrode potential at a fixed laser frequency, broad resonances were observed. It has been generalized that the contribution to SERS by chemical enhancement proceeds via a charge transfer mechanism facilitated by one or more of several factors may that include: bonding interactions between adsorbed molecules and the substrate; orientation and coverage dependency of adsorbates; metal surface structures; and electrode potential. The original hypothesis suggested that new, hybrid electronic states are formed resulting from the chemisorption process that serve as virtual intermediate charge transfer states.

In Raman scattering, the charge transfer (CT) state can be in partial resonance with the incident laser frequency in the visible spectral region [45–47]. In general, four possibilities exist for the interaction of light with a molecule adsorbed on a metal surface: an electron excitation of the metal, an intramolecular electron excitation within the adsorbate, an electron excitation from a filled state of the metal to an empty state of the molecule, or an electron excitation from a filled state of the molecule to an empty metal state.

First, let us consider the molecule and the adsorption process. It is important to make a distinction between the intermediate SERS-CT excited state and charge transfer associated with the formation of a chemical bond. The former is a photon-induced electronic excitation involving a ground and an excited state. The latter results from the adsorption process and produces a ground state complex composed a linear combination of atomic and molecular orbitals of the adsorbate and substrate atoms invoked in bonding. In the case where chemisorption occurs, charge is either shared between the adsorbate and substrate in the form of a covalent bond or charge is tranferred from adsorbate to substrate or *visa versa* to form an ionic-like bond. In any event, the chemisorbate complex should be taken as a whole and include the local interaction between the metal atom(s) involved in bonding and the adsorbate. The extent to which the underlying bulk electronic structure is involved has yet to be fully determined, however, most experimental results indicate that the SERS-CT mechanism is quite local in nature and is described in general terms as a “first-layer” phenomenon [12, 21, 48].

The contribution to SERS due to charge transfer resulting from chemisoption should depend strongly on the adsorption site occupied by the adsorbate its and equilibrium geometry. Surface science experiments have shown that the heats of adsorption and bonding interactions arising from chemisorption differ from site to site. This clearly implies different electronic overlap between the adsorbate and substrate wave functions [49]. Due to differences in the local electronic structure and geometry for different adsorption sites, the adsorbate-surface interactions will influence the extent of charge transfer resulting from the adsorption process. Consequently, the variation of the α_{zz} polarizability tensor element is expected to be dependent on orientation and electronic overlap. This also implies that different SERS-CT states may be influenced by different adsorbate orientations which would result in different transition dipole moments. Consequently, the polarizability derivatives with respect to the same normal modes at different orientations would be different and would produce different SERS intensities.

Most recently, there has been experimental evidence to suggest that the SERS-CT state is similar to the radical anions of neutral adsorbates, e.g, pyridine adsorbed on electrode surfaces [40–42, 50]. The SERS spectrum of pyridine was obtained at negative electrode potentials and is one of the relatively few accepted examples demonstrating the CT mechanism. The SERS active bands were attributed to the equlibrium geometry changes associated with the two states involved: the neutral ground state and the radical anion of excited SERS-CT state. The SERS-CT mechanism involves a photon induced charge transfer from the silver electrode to pyridine.

Still, one is left to ponder the role of substrate effects since microscopic roughness features are ever present and would make an em contribution to the SERS intensity. Furthermore, less has been made of the fact that negative potentials must be applied in order to observe appreciable SERS intensity. Clearly, the negative potentials must affect the ground state equilibrium geometries by changing the relative amounts of charge in the bonding orbitals of the molecule. On flat surfaces and in UHV where experiments are carried out under zero bias this effect is not influential; however, the SERS-CT mechanism has been invoked for the chemisorption of the pyromellitic dianhydride (PMDA) on copper and silver surfaces.

2.3.3 Instrumentation

The experimental apparatus has been described in detail elsewhere. Surface Raman scattering experiments were conducted in a UHV chamber with a typical base pressure of 2 X 10^{-10} Torr. Raman spectra were acquired using 50-100 mW of 647.2 nm light produced by a Coherent-Innova 200 Ar^+ laser pumping Kiton Red in a Coherent Cr-599 dye laser. The copper crystal temperature was monitored and did not change upon illumination. All spectra were acquired in 600 sec scans with the luminescent background from the substrate subtracted.

Chapter 3

Surface Chemistry of Organic Anhydrides on Cu(111)

The adsorption and reactivity of aromatic molecules on metal surfaces are of considerable interest. The study and understanding of organic precursor structure, bonding, and orientation on surfaces is crucial for the optimal performance of thin film device structures on the nanometer length scale. Polyimide films are a class of polymers which can be formed into ultra-thin films that widely used as insulating materials in the microelectronics industry. The formation of polyimide films on copper surfaces proceed via the condensation and subsequent thermal reaction of a diamine and aromatic dianhydride. The most common of the dianhydrides used is 1,2,4,5-benzenetetracarboxylic dianhydride, or more commonly, pyromellitic dianhydride (PMDA).

The interaction of PMDA with metal surfaces has been the subject of numerous studies [10, 16–19, 51–61]. The earliest experiments performed at room temperature suggested that the PMDA-surface interaction proceeds by a ring-opening reaction of one of the anhydride units accompanied by the loss of CO to the gas phase. Infrared (IR) and high resolution electron energy loss spectroscopy (HREELS) provided evidence for the formation of a carboxylate

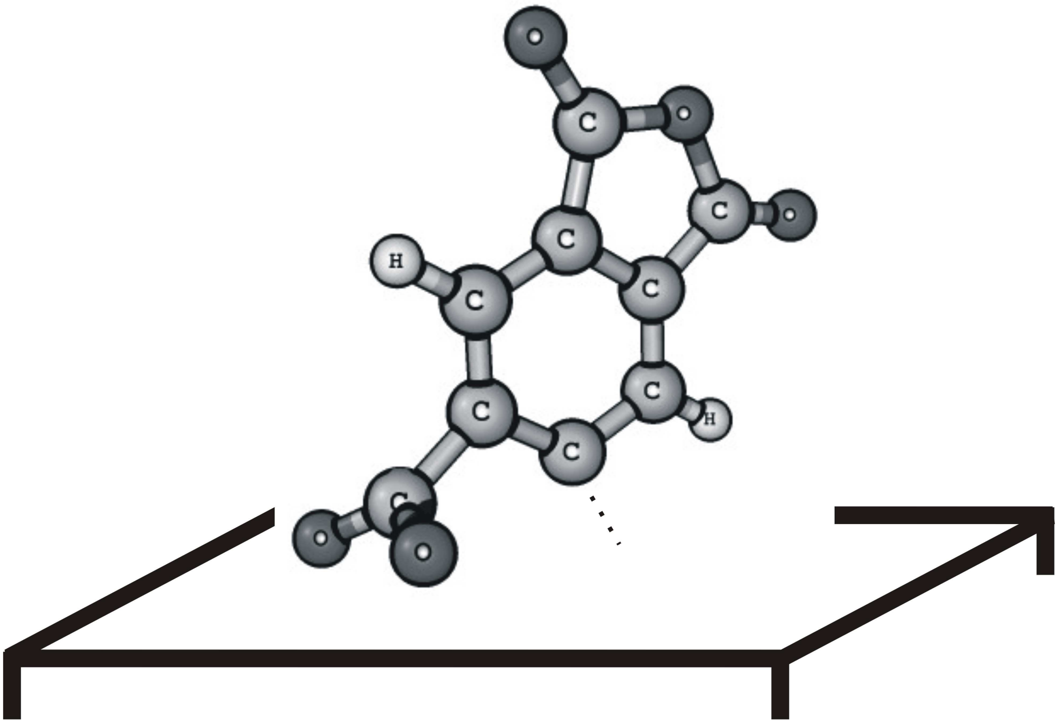

Figure 3.1: Model of the adsorption geometry of PMDA at room temperature.

link between the intact portion of the molecule and the surface [56, 60]. Surface Raman scattering experiments performed within our own research group on Si(100) [51], Ag(111) [52], and Cu(111) and Cu(100) [10, 16–19] confirmed these results and extended them to include adsorption at temperatures below 120K. The molecular orientation was believed to favor an upright geometry such that the long axis of the molecule pointed closer to the surface normal as illustrated in Figure 3.1

However, a recent set of experiments performed on Cu(110) at 95K concluded that, at least for initial PMDA coverages, the molecule favored a flat-lying geometry [58, 61]. These results are rather interesting in light of the previous observation of enhanced Raman scattering from PMDA adsorbed on the Cu(111) and Cu(100) surface [10, 16–19]. Thus it is not clear what is the relevant bonding orientation of PMDA at room temperature and at temperatures below 120K and what influence this may have on the previous results. From the previous Raman experiments, the interpretation of the adsorbate structure was based on the early IR and HREELS work performed at room temperature. Clearly, a difference in bonding orientation should play a role in the overall electronic structure and hence polarizability of PMDA adsorbed on a copper surface. Moreover, SERS has yet to be observed for PMDA adsorbed at room temperature, suggesting that bonding geometry may be important. For these reasons, the adsorption and reaction of PMDA as well as its ideal model compound, phthalic andhydride, on Cu(111) were examined at 110K and 295K.

3.1 Phthalic Anhydride, $C_8H_4O_3$.

In order to aid in the interpretation of the PMDA-surface interaction, I studied the adsorption at 110K of a related molecule, phthalic anhydride. Phthalic anhydride is a simpler version of PMDA and has a smaller number of vibrational normal modes. In principle, this should simplify the interpretation of the PMDA vibrational and electronic excitation spectra. Figure 3.2 presents the HREEL spectra of phthalic anhydride adsorption on clean Cu(111) at 110K for increasing exposures. The exact coverages are not known, but based on previous published accounts [58, 60], the film thickness has not reached the mulitilayer regime. For the lowest coverage shown, the principle loss feature is found at 690 cm^{-1}. Evidence for CO co-adsorption is from the weak loss feature near 2100 cm^{-1}. With increasing exposure, the 690 cm^{-1} band continues to increase in intensity and a weak band at 3050 cm^{-1} becomes apparent. An additional low frequency band near 400 cm^{-1} also becomes evident at higher coverages. The low intensity band near 1600 cm^{-1} and a broad band near 3400 cm^{-1} is evidence for H_2O co-adsorption.

The adsorption of phthalic anhydride on Cu(110) has been studied previously at 95-300K by IR and HREELS [58, 60]. Those experiments showed that phthalic anhydride adsorbed on the clean copper surface intact at low temperature with the molecular plane parallel to the substrate. The HREEL spectra presented in Figure 3.2 are consistent with the previous accounts [58, 60]. The main loss feature at 690 cm^{-1} is assigned to the out-of-plane γ(C-H) mode indicating that the molecule is adsorbed in a flat-lying, π-bonded ge-

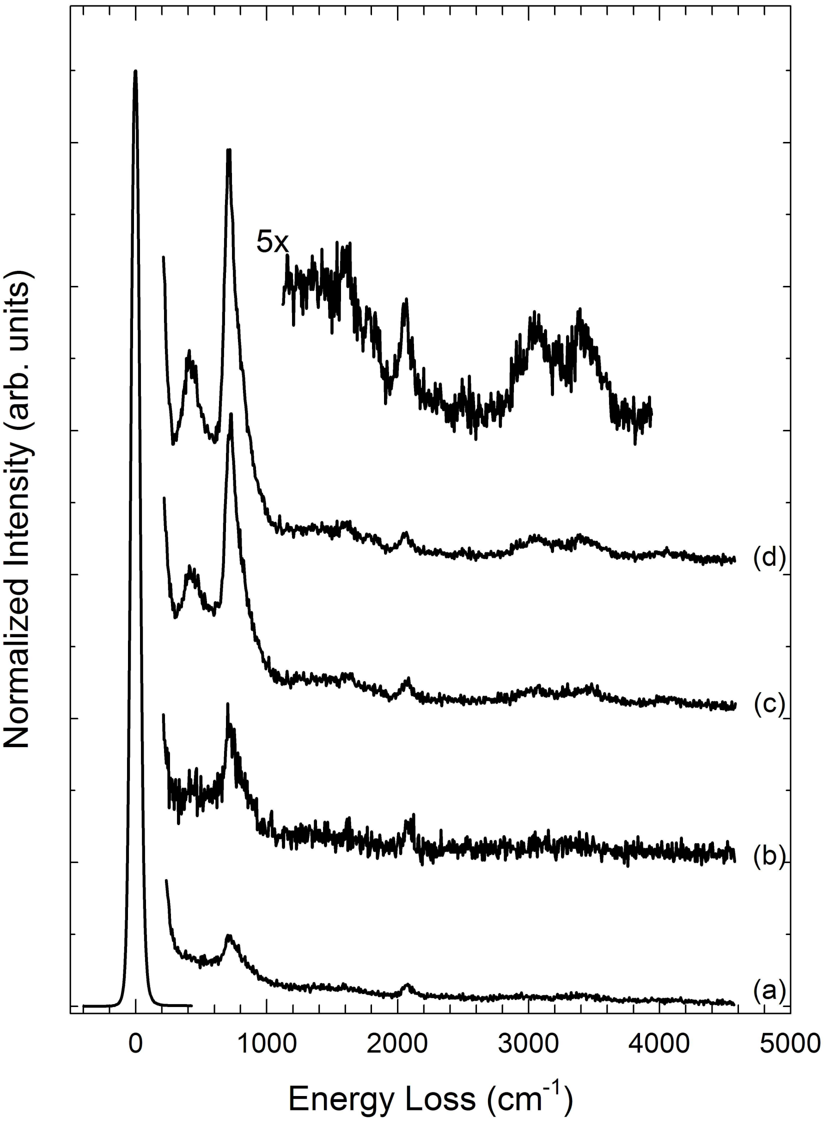

Figure 3.2: HREEL spectra of phthalic anhydride adsorption on clean Cu(111) at 110K, showing the monolayer formation with increasing coverages. Spectrum *d* is amplified by a factor of 5 as indicated and suggests that CO and H_2O are co-adsorbed during the dosing of phthalic anhydride.

ometry. The 400 cm^{-1} band is assigned to an out-of-plane deformation of the aromatic ring. The dynamic dipole of these two modes are perpendicular to the plane of the molecule since it projects along the surface normal. The anti-symmetric and symmetric carbonyl bands, which should be seen at 1762 cm^{-1} and 1852 cm^{-1}, respectively, are not active, also indicating a parallel adsorption geometry. The peaks due to co-adsorbed CO and H_2O are attributed to contamination from the gas phase. Although great care was taken during sample preparation, some residual CO and H_2O adsorption could not be avoided.

The electronic absorption spectrum for phthalic anhydride adsorbed on Cu(111) at 110K is shown in Figure 3.3. The intramolecular electronic excitations for phthalic anhydride appear at 4.1 eV, 4.9 eV and 6.0 eV for a typical monolayer spectrum. The intrinsic intramolecular excitations of phthalic anhydride, a colorless crystalline material, occur in the ulraviolet region [62]. These transitions are typical of aromatic compounds and are assigned to $\pi \rightarrow \pi^*$ electronic transitions.

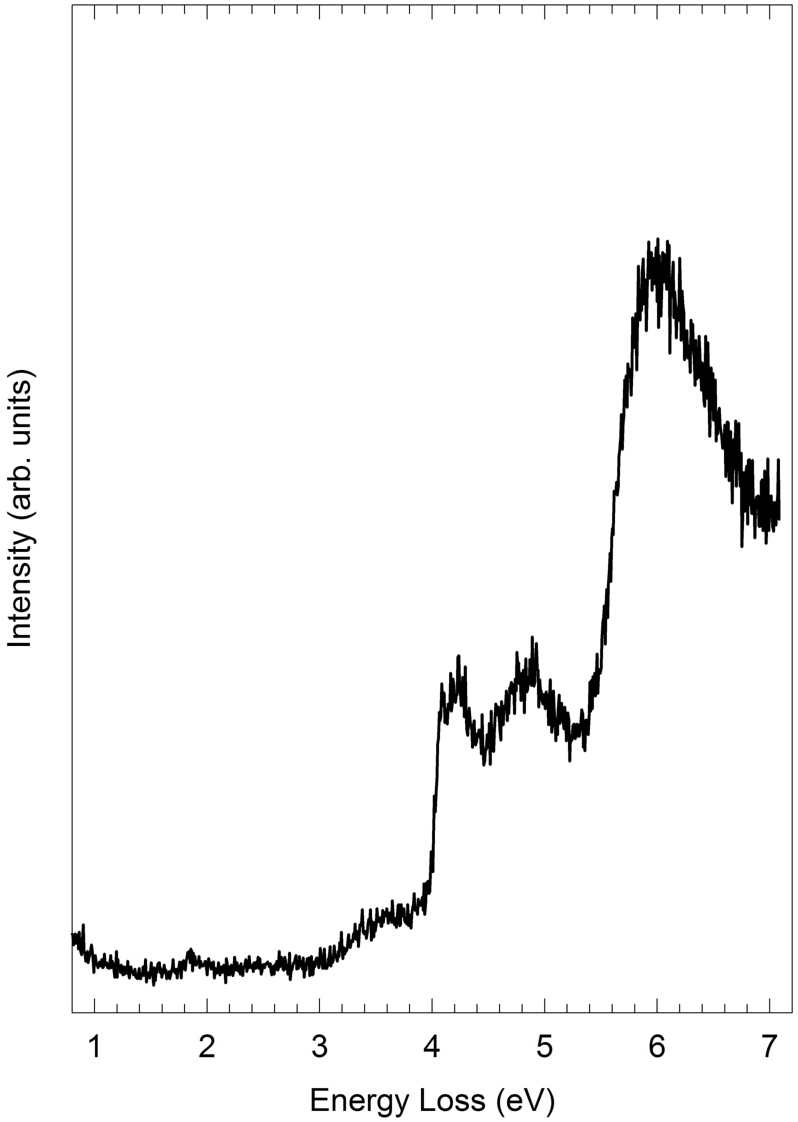

Figure 3.3: Electronic excitations of phthalic anhydride on clean Cu(111) at 110K by EELS.

3.2 Pyromellitic Dianhydride (PMDA), $C_{10}H_2O_6$.

Figure 3.4 shows the HREEL spectra of 2Å, 4Å, 6Å, 8Å, and 12Å thick films of PMDA condensed at 110K on a clean Cu(111) surface. The films correspond approximately to sub-monolayer (2Å-4Å), monolayer (6Å-8Å) and multilayer (12Å) coverages. At the onset of adsorption, four distinct vibrational losses appear at 710, 920, 1240, and 1740 cm^{-1} and increase in intensity as the film thickness is varied. The first two features are assigned based on IR and Raman spectroscopy of crystalline PMDA as an out-of-plane C=O deformation γ(C-O) and the anti-symmetric anhydride ring ν_{as}(COC) stretch of the parent molecule [63]. The peak at 1240 cm^{-1} appears in close proximity to the frequency of the symmetric anhydride ring ν_s(COC) stretch (1276 cm^{-1}) [63]. Additionally, a weak feature at 395 cm^{-1} in the 2Å spectrum becomes more resolved at higher coverages and is assigned as an out-of-plane ϕ(C-C) phenyl ring mode. A very weak band in the region of ν(C-H) (3080 cm^{-1}) can also be identified at completion of the monolayer. It should also be noted that the 2070 cm^{-1} peak is attributed to condensed CO due to background adsorption that occur during the initial exposure and does not increase in intensity with subsequent depositions.

Interestingly, I do not observe any appreciable dipole intensity in the 1750-1875 cm^{-1} region of the spectra that would be characteristic of ν(C=O) stretching modes of the anhydride ring. The broad, asymmetric peak at 1740 cm^{-1} observed in the 2Å film does not correlate with the intact parent molecule and indicates that PMDA undergoes some structural modification at very low

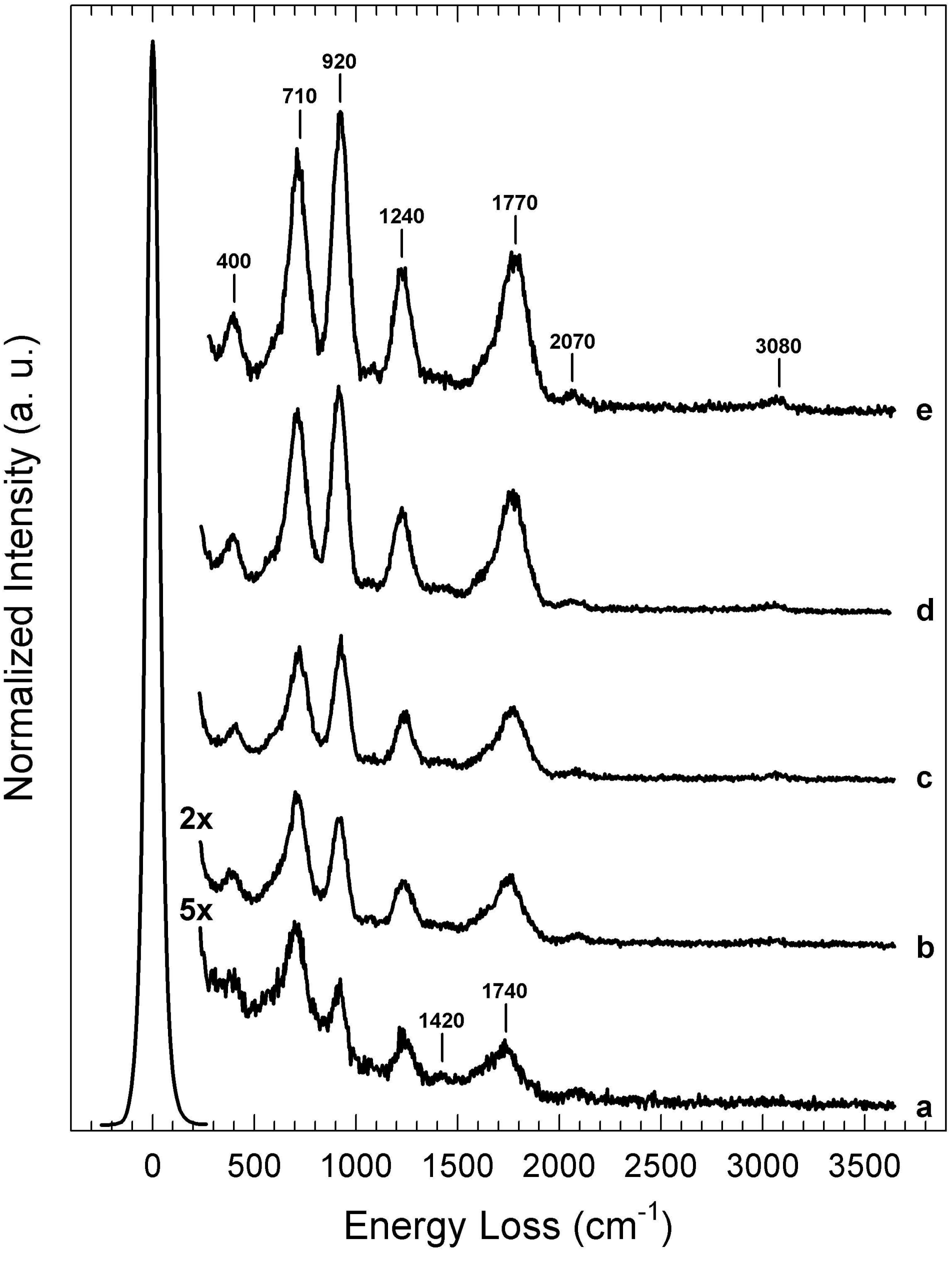

Figure 3.4: HREEL spectra of PMDA adsorption on clean Cu(111) at 110K. The corresponding coverages are (a) 2Å, (b) 4Å, (c) 6Å, (d) 8Å, and (e) 12Å.

coverages upon adsorption at 110K.

I have also investigated the adsorption of PMDA on clean Cu(111) at 295K and have found that the surface chemistry is quite different when compared to the low temperature results. Figure 3.5 shows the monolayer HREEL spectrum of PMDA compared with the same film adsorbed at 110K. Clearly, PMDA is much more reactive at room temperature as evidenced by the dramatic changes between the two spectra. First, new bands appear at 447 cm^{-1}, 600 cm^{-1}, 730 cm^{-1}, 1140 cm^{-1}, 1580 cm^{-1}, and 1820 cm^{-1}. Second, the relative intensities of the 910 cm^{-1} and 1257 cm^{-1} peaks have changed with respect to their low temperature counterparts at 920 cm^{-1} and 1240 cm^{-1}. Finally, the 3080 cm^{-1} peak has become strongly activated.

I have measured the thermal evolution of the PMDA vibrational spectrum from 110K to 400K, which is shown in Figure 3.6. There appears to be little difference in the PMDA geometry when the film is annealed to 300K or if it is adsorbed at 295K. Both result in similar adsorbate structures which will be discussed in the following section. As the PMDA film is annealed to 400K, there is a decrease in intensity in the 450 cm^{-1}, 722 cm^{-1}, 954 cm^{-1} and 1854 cm^{-1} bands suggesting that a loss of material occurs above 300K either through desorption or decomposition of the adsorbate layer.

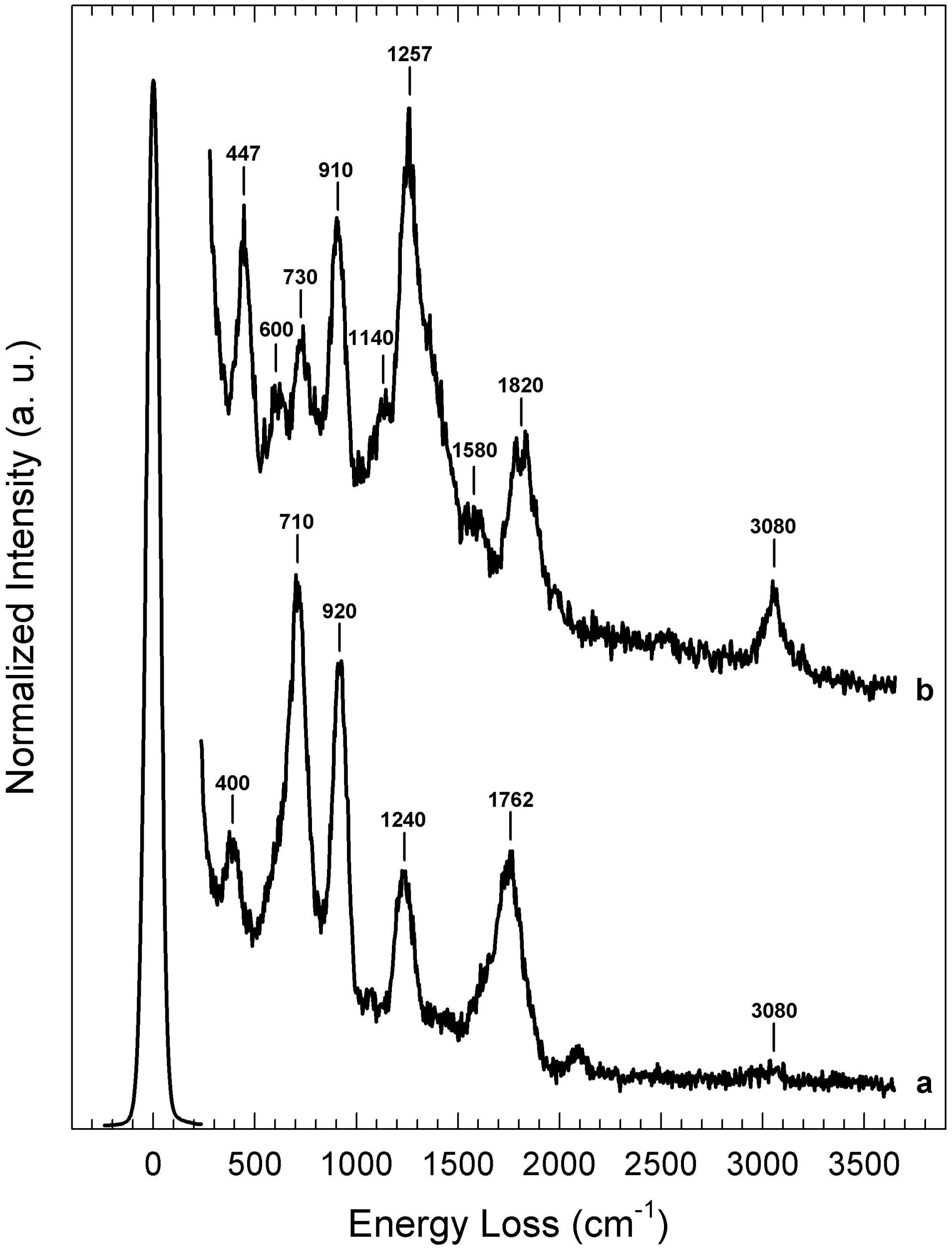

Figure 3.5: HREEL spectra comparing the adsorption of PMDA on clean Cu(111) at (a) 295K and (b) 110K.

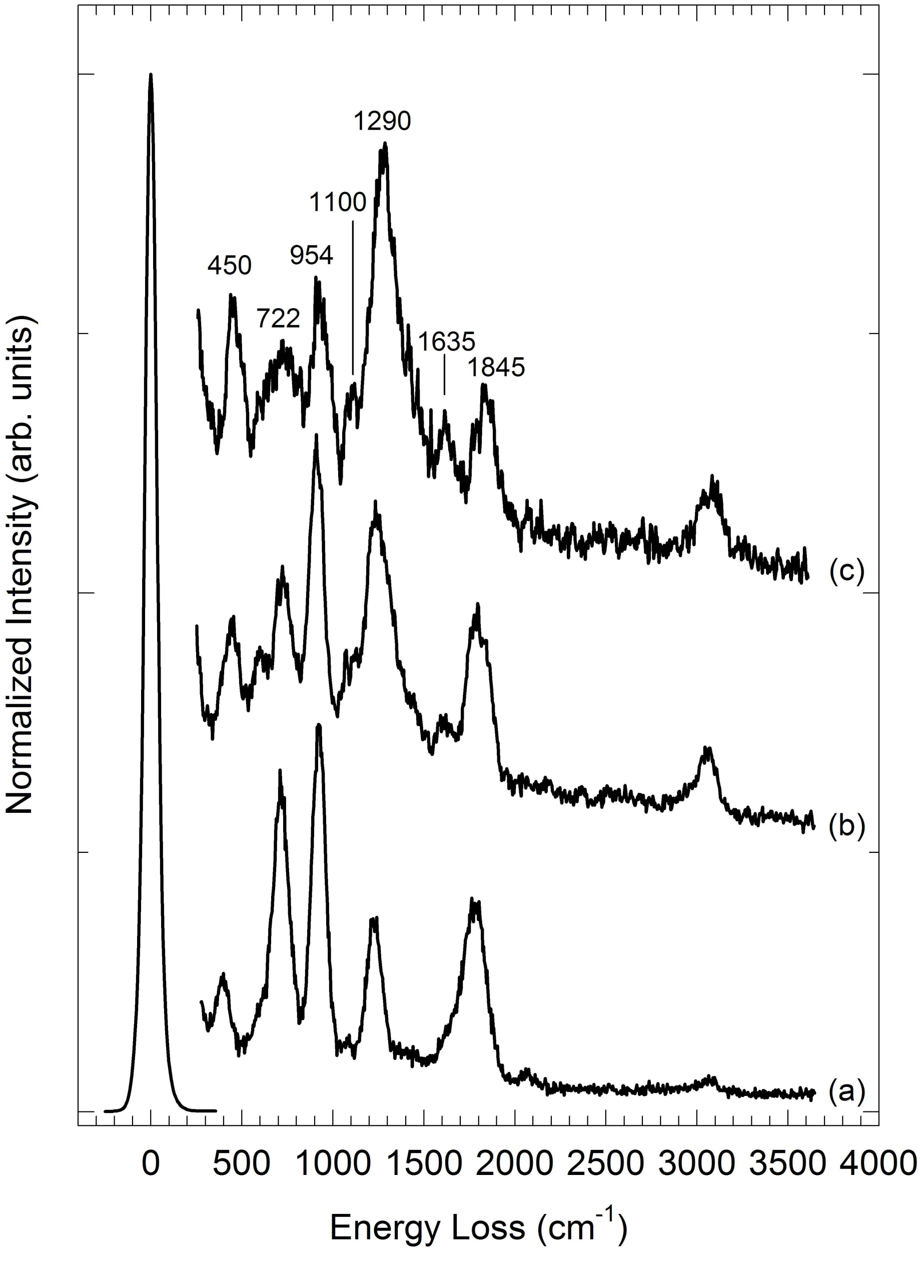

Figure 3.6: HREEL spectra showing the thermal evolution of (a) PMDA adsorbed on clean Cu(111) at 110K. The low temperature film is annealed to (b) 300K and (c) 400K, and then cooled back to 110K for the measurement of the HREEL spectrum.

3.3 Discussion of PMDA adsorption.

The chemisorption orientation of PMDA on a variety of substrates including Si [52], Ni [56, 57], Ag [51, 53] , Pt [55], and Cu [58–61] has been studied. The consensus is that PMDA dissociatively adsorbs to the substrate via an anhydride ring opening mechanism at one end of the molecule. At room temperature, PMDA binds to the substrate through the formation of a surface carboxylate group and the loss of CO to the gas phase

$$\mathrm{Cu_{(surface)} + C_{10}H_2O_6 \rightarrow (Cu^+C_9H_2O_5^-)_{ads} + CO_{(g)}}$$

with the resulting adsorbate complex resembling an inorganic charge-transfer complex. The other anhydride group remains intact and the molecular plane of the adsorbate is oriented such that the long C_2 axis of the molecule is directed toward the surface normal in an upright geometry. The plane containing the carboxylate group is considered to be perpendicular to the intact molecular plane (see Figure 3.1).

On the other hand, the study of PMDA on Cu(110) by the Richardson group [61] using RAIRS remains the only comprehensive spectroscopic study at low temperature (95 K) regarding PMDA adsorption, chemistry, and orientational changes. Those results also demonstrated a coverage dependent reorientation of the adsorbate geometry. At low coverage and 95K, PMDA molecules that are initially bound with their molecular planes closely parallel to the surface undergo the ring opening process resulting in adjacent carbonyl and carboxylate groups.

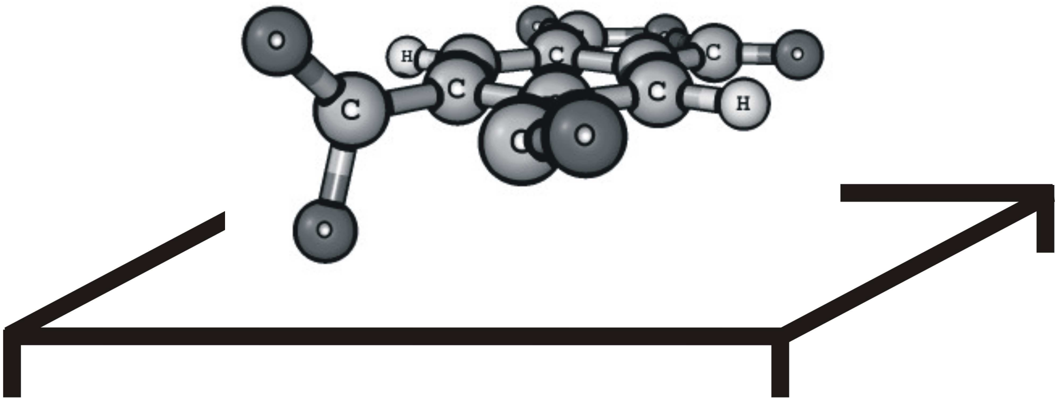

Figure 3.7: Low temperature model of PMDA adsorption on copper proposed by Haq and Richardson.

The steric repulsion between these two groups was argued to cause an out-of-plane twisting of the carboxylate group. The intact molecular plane remained (mostly) parallel to the surface. In order to accommodate the increasing coverages, additional adsorbing molecules then favor a more upright geometry. Similar behavior was found for phthalic anhydride. In both cases, at low coverage and at low temperature, the molecules preferred to adsorb in a flat-lying, π-bonded geometry as depicted in Figure 3.7. By assuming this orientation, considerable electronic overlap between the substrate and the π-system of the adsorbate can occur.

To account for the observed spectral changes in Figures 3.4 - 3.6, I analyzed the normal coordinates of the stretching and bending modes of the anhydride ring groups. The known X-ray crystal structure [64] for crystalline PMDA belongs to the space group C_{4h}^4 ($P4_2/n$); the unit cell contains four equivalent PMDA molecules positioned at sites with C_i symmetry. An isolated PMDA molecule has a quasi-planar molecular structure close to the D_{2h} symmetry point group as illustrated in Figure 3.8.

Infrared (Raman) active vibrations belonging to the b_{1u} (b_{3g}) and b_{2u} (a_g) representations transform as in-plane modes whereas vibrations of the b_{3u} (b_{1g} and b_{2g}) representations are out-of-plane modes. Infrared and Raman spectra have been measured previously [63] for PMDA in the crystalline phase and the frequencies have been assigned on the basis of D_{2h} symmetry. Under the D_{2h} symmetry group, ν_s(COC) (1276 cm^{-1}) and ν_s(C=O) (1854 cm^{-1}) have b_{2u} symmetry while ν_{as}(COC) (920 cm^{-1}) and ν_{as}(C=O) (1775 cm^{-1})

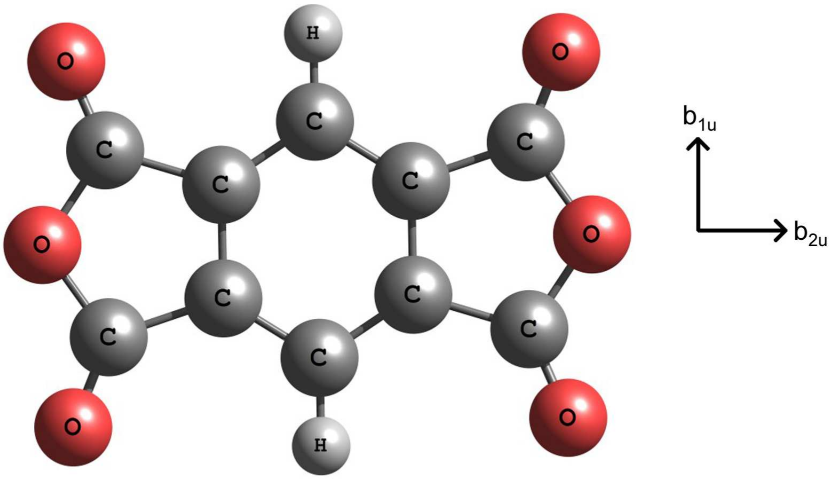

Figure 3.8: D_{2h} molecular symmetry of PMDA.

have b_{1u} symmetry. Accordingly, activation of the b_{2u} modes requires dynamic dipole moment changes along the long C_2 axis of the molecule while activation of the b_{1u} modes involve dynamic dipole moment changes along the short C_2 axis of the molecule.

The HREELS data I present are consistent with the low coverage model proposed by Richardson in reference [61] for the ranges of PMDA film thicknesses (2-12Å) studied. Vibrational modes observed in Figure 3.4 at 1640 cm^{-1} (unresolved) and 1740 cm^{-1} indicate that in the initial stages of adsorption, PMDA undergoes the anhydride ring-opening reaction forming a surface species with both a carbonyl (1740 cm^{-1}) and carboxylate (1640 cm^{-1}) moiety [61]. The carboxylate group vibrational frequencies depend on the bonding geometry of the molecule. Typically, for a symmetrically bound carboxylate group with equivalent or nearly equivalent C-O bond lengths, two normal modes are observed for the symmetric and anti-symmetric ν(OCO) stretches between 1400-1440 cm^{-1} and 1530-1580 cm^{-1}, respectively [65]. However, if the C-O bond lengths are not equivalent, the frequencies are expected to shift. Richardson [61] proposed a mono-dentate surface carboxylate (CO_2^-) bonding geometry where a C=O bond and a C-O bond exist with their respective frequencies located between 1640-1680 cm^{-1} and 1200-1300 cm^{-1}. By assigning the unresolved 1640 cm^{-1} peak to the C=O bond of the carboxylate and the 1740 cm^{-1} peak to the phenyl carbonyl moiety, I can then assign the 1240 cm^{-1} peak to the corresponding C-O bond in the carboxylate. The assignment of the 1240 cm^{-1} band is further supported by the inactivity of the ν_s(C=O) mode which should appear at 1854 cm^{-1} if ν_s(COC) were active. The symmetric anhydride ring mode ν_s(COC) (1276 cm^{-1}) appears to remain inactive.

A picture for the low coverage (2-12Å) adsorption geometry at 110K on Cu(111) develops in the same fashion as on the Cu(110) surface if I also consider that PMDA adsorbs with the molecular plane initially parallel to the surface [61]. The subsequent ring-opening reaction results in a mono-dentate surface carboxylate in which the plane of the group is twisted perpendicular to the molecular plane containing the second, unperturbed anhydride ring. The strong dipole activity for the out-of-plane b_{3u} γ(C=O) at 710 cm^{-1} combined with the absence of the anhydride ring carbonyl ν(C=O) stretches provide strong evidence for the parallel adsorption geometry due to the surface selection rule for the dipole scattering mechanism of EEL spectroscopy. As the film thickness increases, I observe small changes in the molecular orientation by noting that the intensity of γ(C=O) (710 cm^{-1}) relative to the ν_{as}(COC) (920 cm^{-1}) intensity is reduced. I observe that the 1740 cm^{-1} peak shifts to higher frequencies with increasing PMDA coverages. I also observe some weak dipole activation of the C-H stretching modes at 3080 cm^{-1}. During the initial film growth, I observe loss features corresponding to the γ(C=O) (710 cm^{-1}), ν_{as}(COC) (920 cm^{-1}), the carboxylate C-O bond (1240 cm^{-1}) stretch, the carboxylate C=O bond (unresolved) 1640 cm^{-1} stretch, and the phenyl carbonyl mode (1740 cm^{-1}). The absence of dipole activity of the ν_s(COC) (1276 cm^{-1}) and corresponding ν_s(C=O) (1854 cm^{-1}) modes indicates that the long C_2 axis of the molecular plane lies parallel to the plane of the surface. The presence of dipole activity of the ν_{as}(COC) (920 cm^{-1}) mode indicates that the short C_2 axis of the molecular plane is not parallel to surface plane, however, the lack of observable activity for the corresponding ν_{as}(C=O) (1775 cm^{-1}) also indicates that the short C_2 axis is not too far from parallel with the plane of the surface. The dipole activity of the surface carboxylate ν(OCO) modes indicates that the plane of the carboxylate is not parallel to the suface.

As I increase the film thickness, I observe that the intensity of γ(C=O) (710 cm^{-1}) decreases relative to ν_{as}(COC) (920 cm^{-1}) in concert with the smooth shift of the 1740 cm^{-1} band toward higher frequencies. This spectral behavior is assigned to a small reorientation of the short C_2 axis away from the the surface plane activating the ν_{as}(C=O) mode causing the 1740 cm^{-1} band to shift to 1770 cm^{-1}. A very weak loss feature associated with the C-H modes at 3080 cm^{-1} also becomes activated with this small orientational change.

A comparison of the low temperature film with the room temperature film reveals vastly different spectra indicating major structural or orientational differences between the two adsorbate phases. My results for the adsorption of PMDA at 295K (Figure 3.5) are also consistent with the previous experiments at room temperature [56–61] and are directly comparable with HREELS experiments on Cu(110) [60] which show that PMDA dissociatively chemisorbs to the substrate by the ring-opening reaction, producing a surface carboxylate and the loss of CO to the gas phase. The resulting room temperature species is bonded to the surface through a bridging carboxylate and the β-carbon on the phenyl ring. The remaining anhydride group remains unperturbed with the molecular plane now oriented mostly perpendicular to the surface. With the upright geometry, I observe that many of the in-plane normal modes are activated upon adsorption of PMDA at room temperature.

The formation of a new surface carboxylate species is characterized by the presence of a ν(Cu-O) stretch at 447 cm^{-1} and the δ(OCO) bending mode at 600 cm^{-1} [60]. The strong dipole activity unresolved near 1420 cm^{-1} is associated with the symmetric carboxylate mode ν_s(OCO) while the weak band near 1580 cm^{-1} is attributed to the antisymmetric carboxylate mode ν_{as}(OCO). With this bonding geometry, I see that the carboxylate stretching frequencies are now shifted to their expected values [65]. I attribute these spectral features to a conversion of the low temperature mono-dentate surface carboxylate to the bridging surface carboxylate at room temperature. The absence of the 1740 cm^{-1} band at 295K provides evidence for the loss of CO to the gas phase.

The remaining features are associated with the phenyl ring, the other intact anhydride ring, and the C-H modes. The two strong bands at 1257 cm^{-1} and 1820 cm^{-1} are attributed to the intact anhydride ring as the symmetric ring ν_s(COC) and carbonyl ν_s(C=O) stretching modes, respectively. The 730 cm^{-1} band is assigned to an in-plane deformation mode of the phenyl ring δ(CCC) while the weak feature at 1140 cm^{-1} is assigned to in-plane bending δ(C-H) of the phenyl hydrogens. The peak associated with the C-H stretching modes at 3080 cm^{-1} is strongly activated indicating a perpendicular alignment of the phenyl plane.

It is quite evident from Figure 3.5 that room temperature adsorption leads to an entirely different adsorbate geometry with respect to the low temperature phase. Indeed, similar behavior was found for adsorption on the more reactive Cu(110) surface [60, 61] where it was also found that low temperature adsorption led to anhydride ring-opening, however the coverage dependence at low temperature did not evolve in the same manner as the room temperature film. Richardson speculated that PMDA condensed on cold copper substrates is a metastable species while the room temperature species is the lowest energy conformation. I have independently verified this observation by noting that initially cold-deposited PMDA films annealed to 300K and subsequently cooled back to 110K do not revert back to the low temperature geometry. Table 1 summarizes the majority of the HREELS peak assignments for PMDA adsorption under various experimental conditions.

Table 3.1: HREELS vibrational frequencies (in cm^{-1}) for PMDA adsorbed on clean Cu(111) for the experimental conditions listed below. All spectral frequencies were obtained in the specular scattering geometry using a primary beam enrgy of 7 eV and instrumental resolution between 7-9 meV.

PMDA [63]	Assignment	2Å (110K)	12Å (110K)	~6Å (295K)
-	ν(Cu-O)			447
364	δ(C-O) b_{2u}			
392	ϕ(C-C) b_{3u}	395	400	
488	δ(CCC) b_{1u}			
581	δ(COC) b_{2u}			
-	δ(OCO)			600
710	γ(C=O) b_{3u}	710	710	730
767	δ(CCC) b_{1u}			
904	γ(C-H) b_{3u}			
924	ν(COC) b_{1u}	920	920	910
1075	δ(C-H) b_{2u}			1140
1238	ν(C-C) b_{2u}			
1276	ν(COC) b_{2u}			1257
1306	ν(C-C) b_{1u}			
1373	ν(C-C) b_{1u}			
1411	ν(C-C) b_{2u}			
-	ν_s(OCO)			1420
-	ν_{as}(OCO)			1580
1627	ν(C-C) a_g			
1775	ν(C=O) b_{1u}		1770	
1854	ν(C=O) b_{2u}			1820
3056	ν(C-H) b_{1u}			
3106	ν(C-H) a_g		3080	3080

3.4 Electronic structure of PMDA.

Although the electronic structure of PMDA adsorption on copper surfaces has already been determined [17], the adsorbate geometry was not directly compared to or correlated with the observed electronic structure. Figure 3.9 illustrates the evolution of the electronic absorption for increasing coverages of PMDA on clean Cu(111) at 110K. The EEL spectrum for the clean surface is in good agreement the calculated absorption spectrum computed from known optical parameters (see Appendix). As the coverage is increased to 12Å, a continuous decrease in the copper interband transition at 2.3 eV is observed in concert with an increase in intensity of the loss features at 4.1 eV, 4.9 eV and 5.9 eV associated with the intramolecular excitations of PMDA. Of notable interest, however, is the complete absence of a narrow and intense transition at 1.9 eV observed in previously published accounts that has been associated with a charge transfer (CT) resonance between PMDA and the substrate [17–19]. This CT resonance has also been shown to be responsible for enhanced Raman scattering for PMDA adsorbed on Cu(111) and Cu(100) at low temperature. Clearly, there is some difference in my results and those previously published [17–19]. After a number of repeated measurements, I was unable to reproduce the previous CT resonance and began to re-examine the data of the earlier results [17–19]. Since there were no previous HREELS studies of the vibrational excitations of PMDA adsorbed on clean Cu(111) it was impossile to compare the current set of vibrational losses to the earlier results. However, low resolution vibrational excitations are obtained when measuring the electronic excitations and I was able to discover two rather striking loss features that dominated the vibrational regime near 1630 cm^{-1} and 3400 cm^{-1} indicating that H_2O was possibly co-adsorbed with the PMDA adsorbate layers.

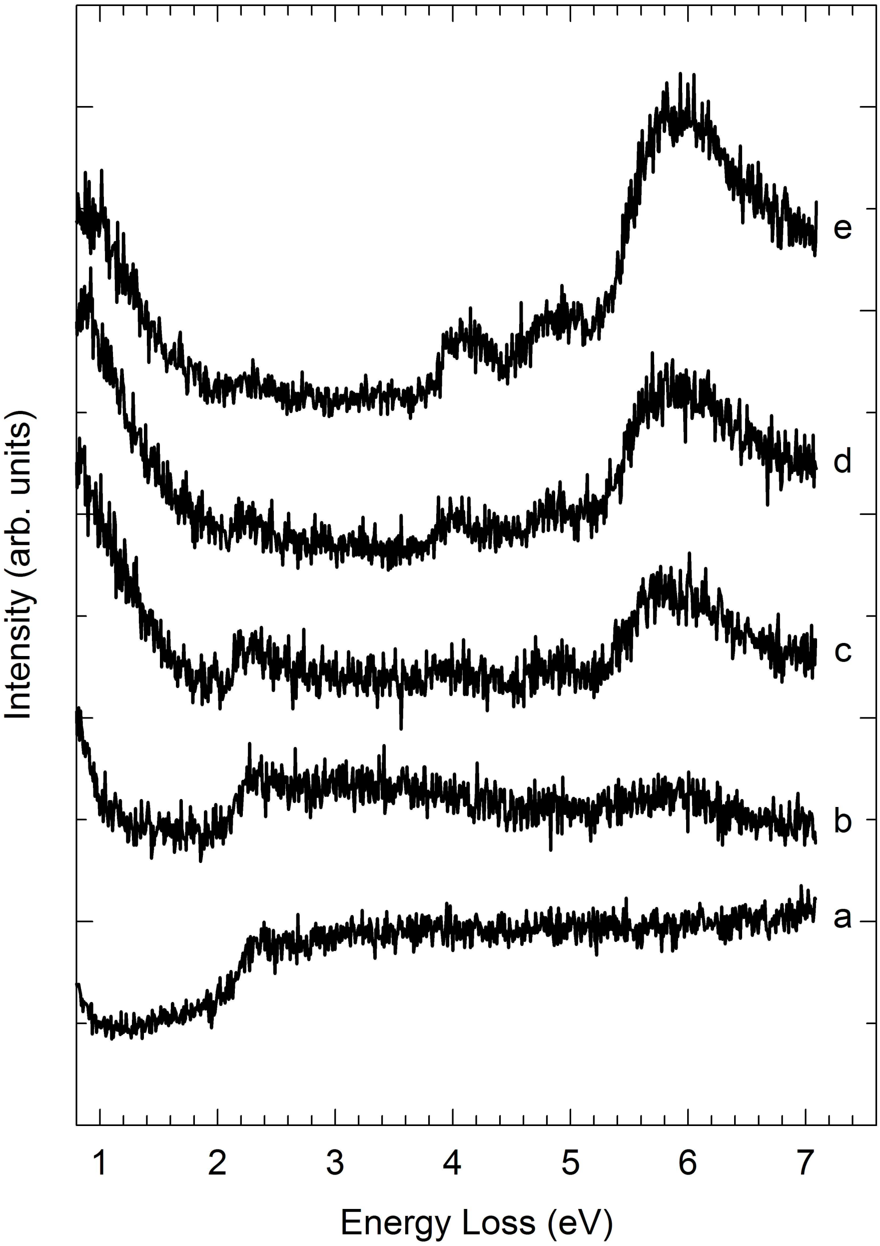

Figure 3.9: Electronic EEL spectra of the adsorption of PMDA on clean Cu(111) at 110K. The coverages shown are (a) clean Cu(111), (b) 2Å, (c) 6Å, (d) 8Å and (e) 12Å.

3.5 Conclusions.

High resolution electron energy loss spectroscopy has been used to characterize the chemical and electronic structure of two anhydride compounds: phthalic anhydride and pyromellitic dianhydride. Both phthalic anhydride and PMDA adsorb in a flat-lying, π-bonded orientation. PMDA adsorption at 110K proceeds by the now well documented ring-opening reaction of one of the anhydride units forming a carboxylate group and carbonyl moiety. PMDA interacts with the surface through the carboxylate linkage and aromatic π system of the intact ligand. The thermal evolution of PMDA produces a surface species that favors an upright orientation that is consistent with previous experimental results. The molecule is bonded to the subtrate throught a bidentate carboxylate and the β-carbon on the central ring, having lost CO to the gas phase. Adsorption at room temperature also produces a similar species. The evolution of the electronic excitation spectra of PMDA adsorption on clean Cu(111) at 110K by my own accounts indicate that the previously observed 1.9 eV charge transfer excitation may result from H_2O co-adsorbed with PMDA. Although this is somewhat speculative, I have hypothesized this to be the case. In Chapter 5, I investigate the influence of H_2O co-adsorption with PMDA on Cu(111) at 110K in order to elucidate the nature of charge-transfer excitations of PMDA in the presence of an electron donating solvent. In the following chapter, I explore the use of density functional theory to determine the electronic structure of PMDA and two other molecules, maleic anhydride and phthalic anhydride, in order to help develop a chemical intuition regarding the structure and reactivity of organic/metal interfaces.

Chapter 4

Density Functional Theory

The contents of this chapter will provide a basis for a qualitative and in some cases quantitative understanding of the behaviour of organic anhydride interactions with metals. In general, I seek to use current quantum chemical methods, namly density functional theory (DFT), to determine the optimized structures, harmonic vibrational frequencies, adiabatic electron affinities, and vertical electronic excitation energies for maleic anhydride, phthalic anhydride, and pyromellitic dianhydride and their respective anions. Specifically, I wish to understand the properties of gas phase molecular anions and how those species may be involved in surface mediated optical and electronic processes. Interestingly, negative ions have been speculated to be involved in the SERS-CT processes I have also taken the approach by Gomes and others using finite sized transition metal clusters to model the adsorbate-surface interactions of H_2O and PMDA adsorbed on Cu(111). I will determine adsorbate structures, binding energies, and vibrational frequencies in an effort to gain insight into the the nature of more complex surface- adsorbate interactions involving more than one surface species.

The literature is filled with examples where DFT hs been used with varing degrees of success to predict accurate molecular structures and electronic properties of neutral and anionic hydrocarbons, medium-sized aromatics, and various halogenated species. Also, there are several studies that examine the adsorbate structure of small (CO, NO, NH_3, etc.) molecules on transition metal surfaces using metal cluster models that incorporate between 1 - 50+ atoms.

This chapter is organized in the following manner. The optimized geometries, harmonic vibrational frequencies, adiabatic electron affinities, and vertical excitation energies for the three organic anhydrides (maleic anhydride, phthalic anhydride, and pyromellitic dianhydride) will be determined in a systematic way using several of the popular density functional or hydrid Hartree-Fock density functional methods and several basis sets including the medium sized DZP++ [66–69] of Lee and Schaefer and the flexible aug-cc-pVDZ and aug-cc-pVTZ basis sets of Dunning [70, 71]. Charge populations and bond orbitals will be computed to gain insight into the localization of charge upon anion formation. The rest of the chapter pertains to the adsorption of water and PMDA on the Cu(111) surface. I have determined the optimized structures and harmonic vibrational frequencies of H_2O adsorbed on a ten atom copper cluster (Cu_{10}) and PMDA adsorbed on a twenty two atom copper cluster (Cu_{22}). The goal of this chapter is to demonstrate that DFT may be used to complement modern surface spectroscopic methods in a qualitative and in some respects quantitative fashion in the interpretation of adsorbate interactions on metal surface.

4.1 Theory.

Before discussing the details of the results presented in this chapter, I will outline some of the necessary theoretical machinery from which the density functional methods are derived. This should in no way serve as a comprehensive treatise on the subject. Excellent reviews of density functional theory by those considered to be experts on the subject are available in the literature [72–74].

The proofs by Hohenberg and Kohn [75] form the basis for *density functional theory* (DFT), demonstrating that the ground state electronic energy of a system of interacting particles can be uniquely determined from the electron density of the system. The elegance of their theorems lie in the fact that they reduce the complexity of the wave-function based approach for an N-electron system with $3N$ coordinates for each electron. From elementary quantum mechanics, the electron density $\rho(\boldsymbol{r})$ (i.e., probability density) is just the square of the wave-function integrated over $N-1$ electron coordinates. Thus, it is observed that the electron density depends only on 3 coordinates *independent* of the number of electrons. The critical assertion proven by the Hohenberg-Kohn theorems is that the electron density, if it can determined exactly, uniquely determines the Hamiltonian operator and thus all molecular properties of the system. It has been shown that the total ground state energy is a *functional* of the ground state electron density [75]. Likewise, the individual components of the total energy must also be functionals of the ground state density such that

$$E_0[\rho] = T[\rho_0] + E_{ee}[\rho_0] + E_{ne}[\rho_0]. \tag{4.1}$$

In practice [74], the energy expression of Equation 4.1 is separated into what are considered system dependent and universally valid terms. The potential energy due to nuclei-electron attraction, $E_{ne}[\rho_0]$, expressed as

$$E_{ne}[\rho_0] = \int \rho_o(\boldsymbol{r}) V_{ne} d\boldsymbol{r} \tag{4.2}$$

depends on the actual system. The latter two terms of Equation 4.1 are considered to be universal because their forms are indendent of the total number of electrons, N, and the position and charge of the nuclei. Hence, Equation 4.1 may be recast in the form

$$E_0[\rho_0] = \int \rho_o(\boldsymbol{r}) V_{ne} d\boldsymbol{r} + F_{HK}[\rho_0] \tag{4.3}$$

where the system independent parts are defined by the Hohenberg-Kohn functional, $F_{HK}[\rho_0]$.

The functional $F_{HK}[\rho]$ contains the kinetic energy functional, $T[\rho]$, and the electron-electron interaction functional, $E_{ee}[\rho]$, for any arbitrary density $\rho(\boldsymbol{r})$. We can re-write the $E_{ee}[\rho]$ functional in terms of the classical Coulomb part, $J[\rho]$, and a non-classical part that contains the self-interaction correction and the exchange and Coulomb correlation terms such that

$$E_{ee}[\rho] = J[\rho] + E_{ncl}[\rho] = \frac{1}{2} \int \int \frac{\rho(\boldsymbol{r_1})\rho(\boldsymbol{r_2})}{r_{12}} d\boldsymbol{r_1} d\boldsymbol{r_2} + E_{ncl}[\rho]. \tag{4.4}$$

As in the wave-function based approach, we seek to minimize the energy to determine the true ground state of the system. In the Hohenberg-Kohn approach, the $F_{HK}[\rho]$ functional will yield the ground state energy if and only if the true ground state electron density is known. Thus, the ground state energy is derived in a variational way

$$E_0 = \min_{\rho \to N} \left(F[\rho] + \int \rho(\boldsymbol{r}) V_{ne} d\boldsymbol{r} \right) \tag{4.5}$$

where the 'universal mystery functional', $F[\rho]$, contains the kinetic energy, the classical Coulomb interaction, and the nonclassical term that contains the self-interaction correction, exchange, and electron correlation effects,

$$F[\rho] = T[\rho] + J[\rho] + E_{ncl}[\rho]. \tag{4.6}$$

Only $J[\rho]$ is known, but the problem of determing the kinetic energy and non-classical terms was cleverly solved later by Kohn and Sham who supposed that the true kinetic energy of the real system could be determined approximately by using a *non-interacting* reference system with the same electron density as the real, interacting system [76]. Since the non-interacting kinetic energy T_{KS} is not equal to the real kinetic energy T even if the same density is used, Kohn and Sham introduced a correction to $F[\rho]$ given as

$$F[\rho] = T_{KS}[\rho] + J[\rho] + E_{XC}[\rho] \tag{4.7}$$

where the new term E_{XC}, the *exchange-correlation* energy is defined as

$$\begin{aligned} E_{XC}[\rho] &\equiv (T[\rho] - T_{KS}[\rho]) + (E_{ee}[\rho] - J[\rho]) \\ &= T_C[\rho] + E_{ncl}[\rho] \end{aligned} \tag{4.8}$$

with T_C being a residual term of the true kinetic energy and is added to the non-classical part of the energy. Clearly, it is evident that the E_{XC} functional contains all unknown quantities which we are unable to determine exactly. Thus, we arrive at the fundamental expression for the Kohn-Sham equation which stipulates that the exact ground state energy of any N-electron system is given by

$$E_0[\rho] = T_{KS}[\rho] + J[\rho] + E_{ne}[\rho] + E_{XC}[\rho], \tag{4.9}$$

where $T_{KS}[\rho]$ is the *non-interacting* kinetic energy expressed as

$$T_{KS}[\rho] = -\frac{1}{2}\sum_{i}^{N} \langle \phi_i | \nabla^2 | \phi_i \rangle \tag{4.10}$$

and the orbitals, ϕ_i, are defined as the Kohn-Sham orbitals.

Thus in Kohn-Sham DFT [76], the “real” fully-interacting system of electrons is imagined as a system of *non-interacting* electrons under the influence of a common, one-body potential V_{KS} producing the same electron density as the “real” system. The local potential is given by

$$V_{KS} = V_{ne} + V_{ee} + V_{XC} \tag{4.11}$$

where V_{XC} represents the derivative of E_{XC} with respect to ρ

$$V_{XC} = \frac{\delta E_{XC}}{\delta \rho}. \tag{4.12}$$

The set of independent Kohn-Sham reference orbitals must then satisfy the independent-particle Schrödinger equation,

$$\left[-\frac{1}{2}\nabla^2 + V_{KS} \right] \phi_i = e_i \phi_i \tag{4.13}$$

where the local potential V_{KS} is defined such that the *non-interacting* density

$$\rho_{KS} = \sum_{i}^{N} |\phi_i|^2 \tag{4.14}$$

equals the density of the "real" interacting system. Therefore, the total electronic energy of the "real" fully-interacting system can be expressed as

$$E[\rho(\boldsymbol{r})] = T_{KS}[\rho] + \int \rho V_{ne} d\boldsymbol{r} + \frac{1}{2}\int\int \frac{\rho(\boldsymbol{r_1})\rho(\boldsymbol{r_2})}{r_{12}} d\boldsymbol{r_1} d\boldsymbol{r_2} + E_{XC}[\rho]. \tag{4.15}$$

The major goal of the molecular physics community over the past few decades has been to derive appropriate analytical expressions for the the XC functional such that the exact ground state density may be determined.

Since the exact form of the XC functional probably will never be known, approximate functionals have been developed based on the uniform electron gas model. In general, the exchange-correlation functional may be expressed as

$$E_{XC}[\rho] = \int f(\rho, \nabla\rho) d\boldsymbol{r} \tag{4.16}$$

with f a function of the density and gradient of the density at a point $\boldsymbol{r}$. In the local density approximation (LDA) the gradient of the density is not considered and the XC functional takes on the form [76]

$$E_{XC}^{LDA}[\rho] = \int \rho(\boldsymbol{r}) \varepsilon_{XC}(\rho(\boldsymbol{r})) d\boldsymbol{r} \tag{4.17}$$

where the exchange-correlation energy per particle is, $\varepsilon(\rho(\boldsymbol{r}))$ may be separated into exchange and correlation terms

$$\varepsilon_{XC}(\rho(\boldsymbol{r})) = \varepsilon_X(\rho(\boldsymbol{r})) + \varepsilon_C(\rho(\boldsymbol{r})). \tag{4.18}$$

The LDA and the spin-unrestricted LSDA approach are generally considered to be inferior in the sense that real molecules can hardly be assumed to behave as a uniform electron gas. An improvement on the LDA is to include the gradient of the density to account for inhomogeneity of the real electron density. Thus, the approach used in almost all cases today employs the generalized gradient approximation (GGA) where the XC functionals include gradients of the charge density. Once again the XC functional is split into separate exchange and correlation parts and gradient corrections for each component are generally sought after.

At this point, the problem of DFT becomes mathematical and we end up with the litany of *alphabet soup* XC fucntionals like B3LYP, BLYP, B1B95, BHLYP, etc. I will refer the interested reader to the review of Koch and Holthausen [74] for the analytic expressions for all of the popular functionals currently employed. In the following section, I will provide a systematic study of maleic anhydride, phthalic anhydride, and pyromellitic dianhyride to evaluate the performance of various XC functionals with a given basis set.

The reader may question the relevance of such a study with respect to adsorption on surfaces. I have found it very useful to evaluate the perfomance of DFT on the ideal gas phase model compounds for PMDA, i.e. maleic anhydride and phthalic anhydride, in order to gauge the level of success (or failure) one may expect when modeling PMDA adsorption on copper surfaces. As I have alluded to in the previous chapters, PMDA chemisorption on copper results in the transfer of charge from the substrate to the adsorbate upon reaction with the surface. As such, one might expect PMDA$_{ad}$ to be a partial negative ion residing on the surface. While the idealized gas phase D_{2h} PMDA molecule is quite different structurally than the chemisorbed carboxylate species, it may be instructive to understand the differences between the neutral and charged gas phase species.

4.2 Theoretical Methods.

The DFT studies were perfomed on maleic anhydride ($C_4H_2O_3$), phthalic anhydride ($C_8H_4O_3$), and pyromellitic dianhydride ($C_{10}H_2O_6$) and their respective anions. The anions were formed by adding an electron to the HOMO of the neutral. I report the optimized geometries, harmonic vibrational frequencies, and electron affinities using several of the popular DFT functionals including BP86, BLYP, BHLYP, B3LYP, and B3P86 which I now describe briefly. The BP86 functional uses Becke's 1988 exchange functional (B) [77], which includes correction for the gradient of the density, with Perdew's gradient corrected 1981 local correlation functional (P86) [78]. The LYP correlation functional of Lee, Yang, and Parr [79] includes both local and non-local terms and is by far the most popular of the correlation functionals. The LYP correlation functional combined with Becke's 1988 exchange functional delivers the BLYP XC functional. Hybrid functionals include a mixture of the Hartree-Fock exchange (the exchange energy of the Slater determinant which can be computed exactly) with KS exchange correlation. For example, BHLYP uses a modified version of the expression

$$E_{XC}^{HH} = 0.5E_X^{exact} + 0.5E_X^{LSDA} \tag{4.19}$$

with the LYP functional. And finally, the B3LYP hybrid functional uses Becke's three-parameter exchange [80] with the LYP correlation.

I have used a number of standard basis sets including the DZP++ of Lee and Schaefer [66–69] and Dunning's correlation consistent aug-cc-pVnZ (n=D and T) [70, 71]. The DZP++ standard basis of contracted double-ζ Gaussian functions is constructed by augmenting the Huzinaga-Dunning set of contracted double-ζ Gaussian functions with one set of p polarization functions for hydrogen and one set of five d polarization functions for carbon and oxygen. The basis-set is completed by adding one even-tempered s and p diffuse functions to the carbons and oxygens. The even-tempered exponents were determined according to the recipe of Lee and Schaefer [69].

All quantum chemical calculations were carried out using the Gaussian2003 suite of computational chemistry programs [81]. Spin-unrestricted Kohn-Sham orbitals were used for all calculations. Both the neutral and anion geometries were fully optimized by the analytic gradient method. The harmonic vibrational frequencies were determined analytically from the mass-weighted Hessian matrix.

4.3 Results for gas phase anhydrides.

The optimized geometries for the ground states of maleic anhydride, phthalic anhydride and pyromellitic dianhydride and their respective anions are illustrated in Figures 4.1 - 4.6. The optimized ground state C_{2v} structures for maleic anhydride and phthalic anhydride have a ^{1}A$_1$ ground electronic state. Tables 4.1 and 4.2 list the computed harmonic vibrational frequencies of maleic anhydride and its anion, while Tables 4.3 and 4.4 list the computed harmonic vibrational frequencies of phthalic anhydride and its anion. The D_{2h} optimized ground state for pyromellitic dianhydride has a ^{1}A$_g$ ground electronic state. Tables 4.5 and 4.6 list the computed harmonic vibrational frequencies of PMDA and its anion. The anions are realized by adding one additional electron to the HOMO of the neutral molecule. The C_{2v} optimized ground state structures for the anions of maleic anhydride and phthalic anhydride have a ^{2}A$_2$ ground electronic state. The D_{2h} optimized ground state structure for pyromellitic dianhydride anion has a ^{2}A$_u$ ground electronic state.

The adiabatic electron affinity (AEA) is obtained by subtracting the energy of the geometry optimized anion from the geometry optimized neutral. The total energies obtained with the DZP++ basis of the neutrals and anions at their respective optimized geometries are listed in Table 4.7 along with their adiabatic electron affinities. The harmonic zero point vibrational energy (ZPVE) corrected adiabatic electron affinities are also given in Table 4.7. In each case, the addition of one electron results in a lowering of the total energy of the anion yielding a positive AEA. This positive AEA indicates the formation

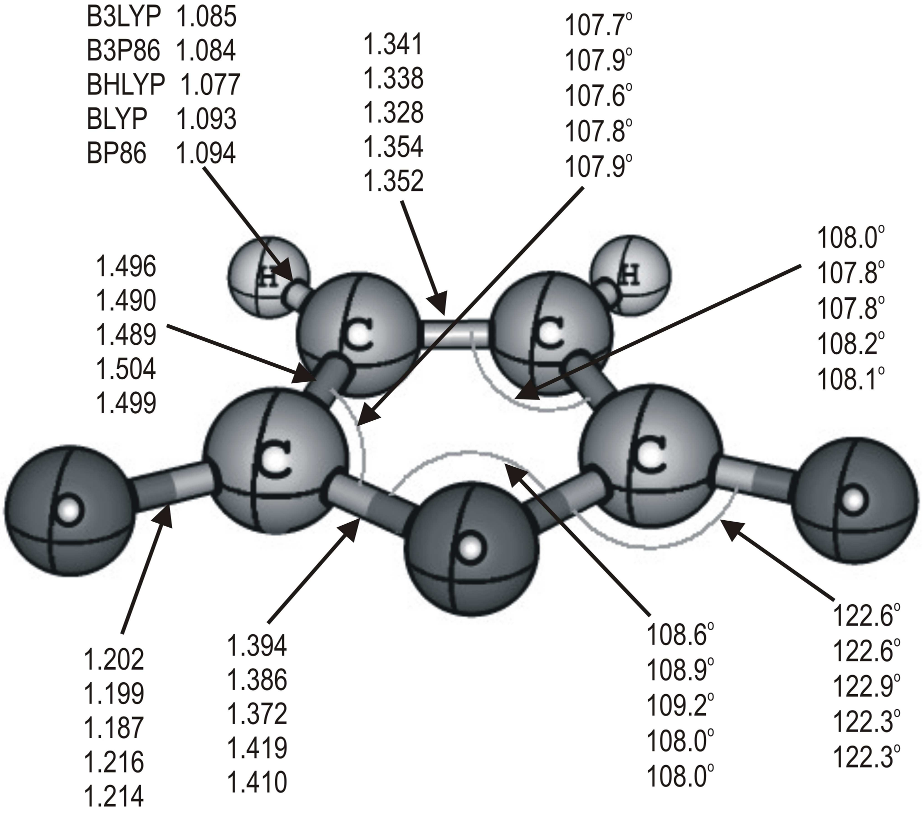

Figure 4.1: Optimized geometry of C_{2v} maleic anhydride in its $^1\text{A}_1$ ground electronic state. Bond lengths are given in Å.

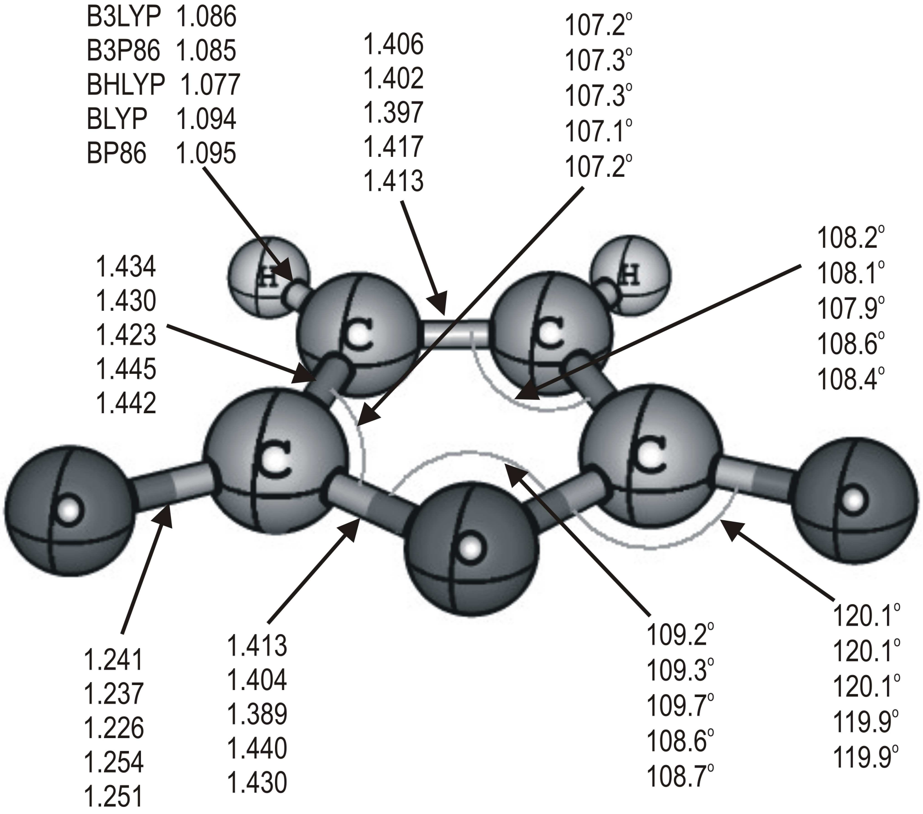

Figure 4.2: Optimized geometry of C_{2v} maleic anhydride anion in its $^2\mathrm{A}_2$ ground electronic state. Bond lengths are given in Å.

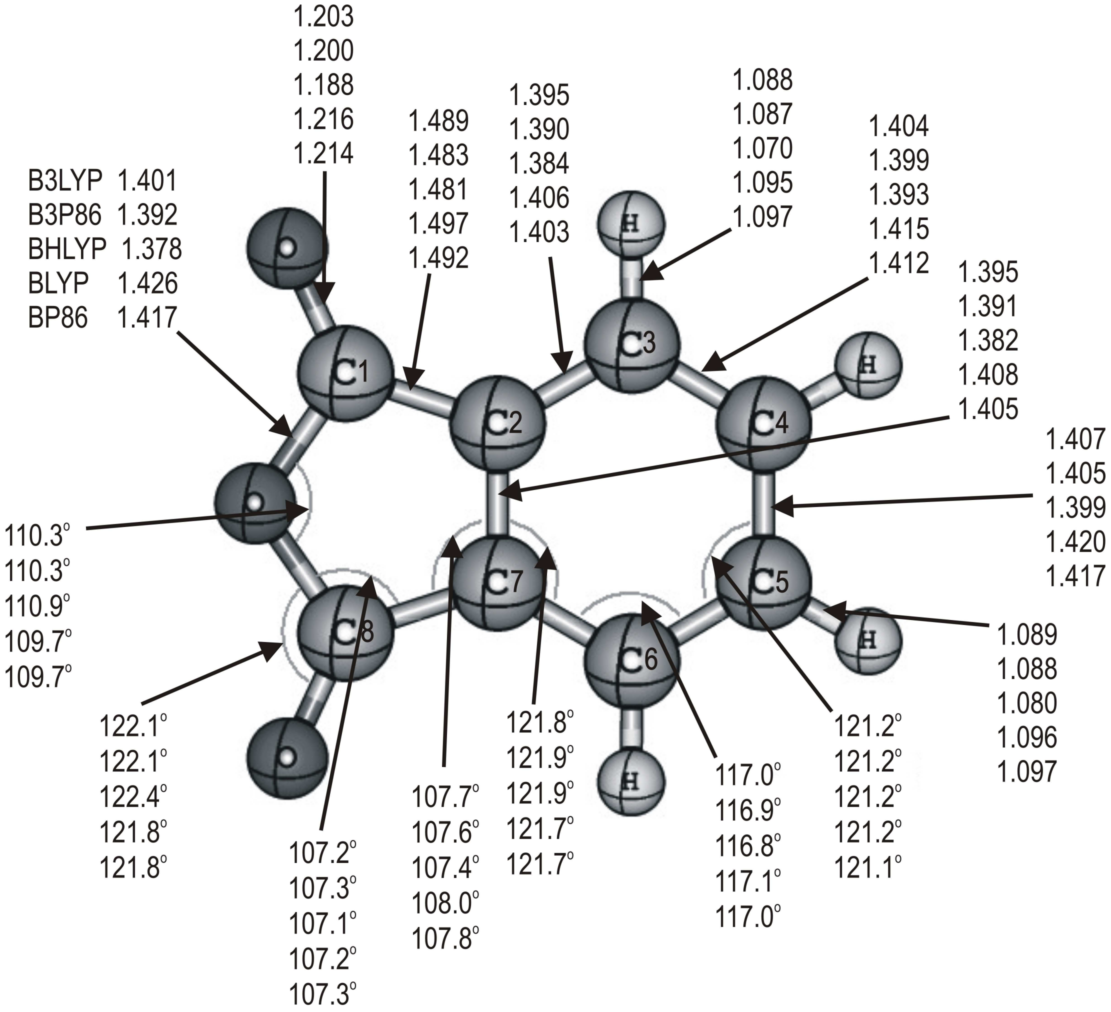

Figure 4.3: Optimized geometry of C_{2v} phthalic anhydride in its $^1\mathrm{A}_1$ ground electronic state. Bond lengths are given in Å.

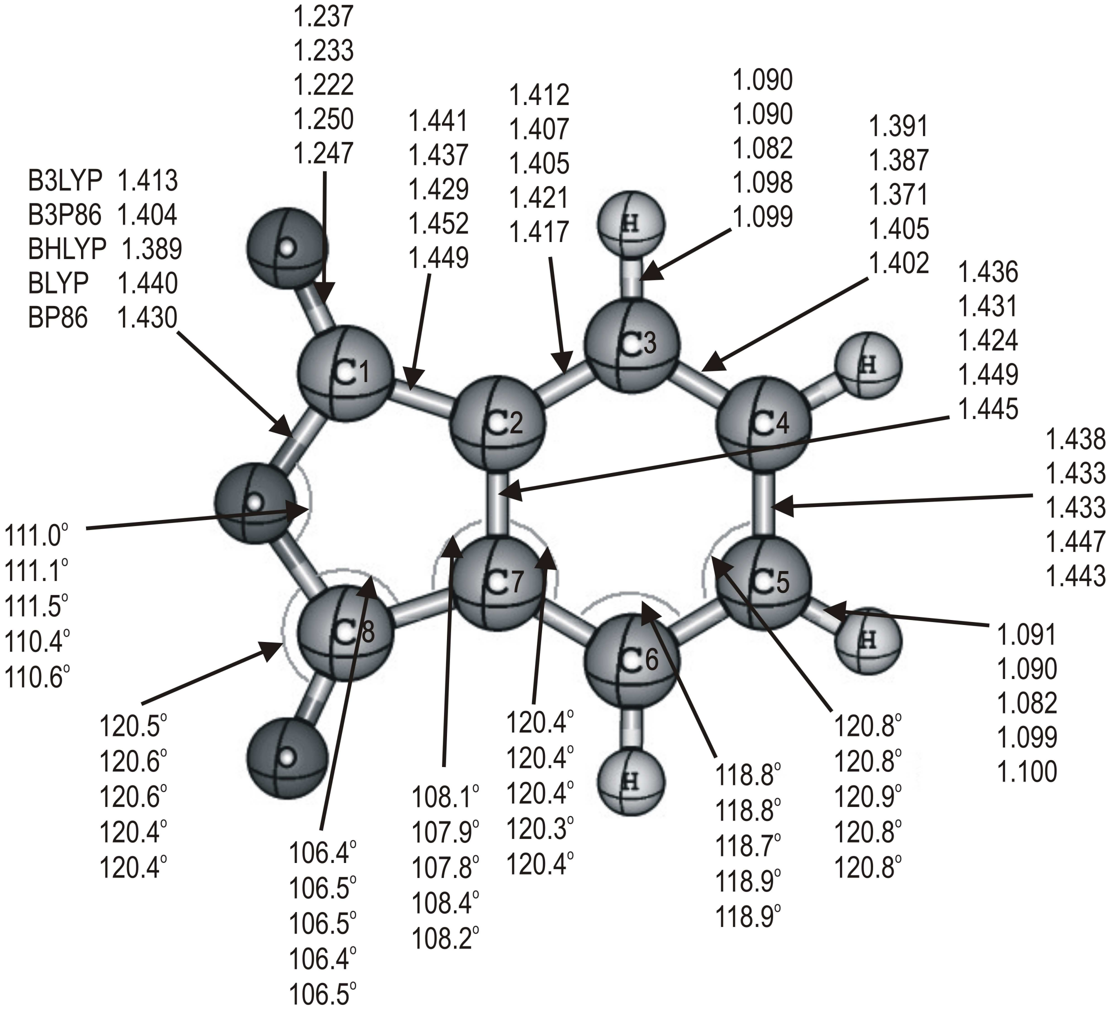

Figure 4.4: Optimized geometry of C_{2v} phthalic anhydride anion in its $^2\mathrm{A}_2$ ground electronic state. Bond lengths are given in Å.

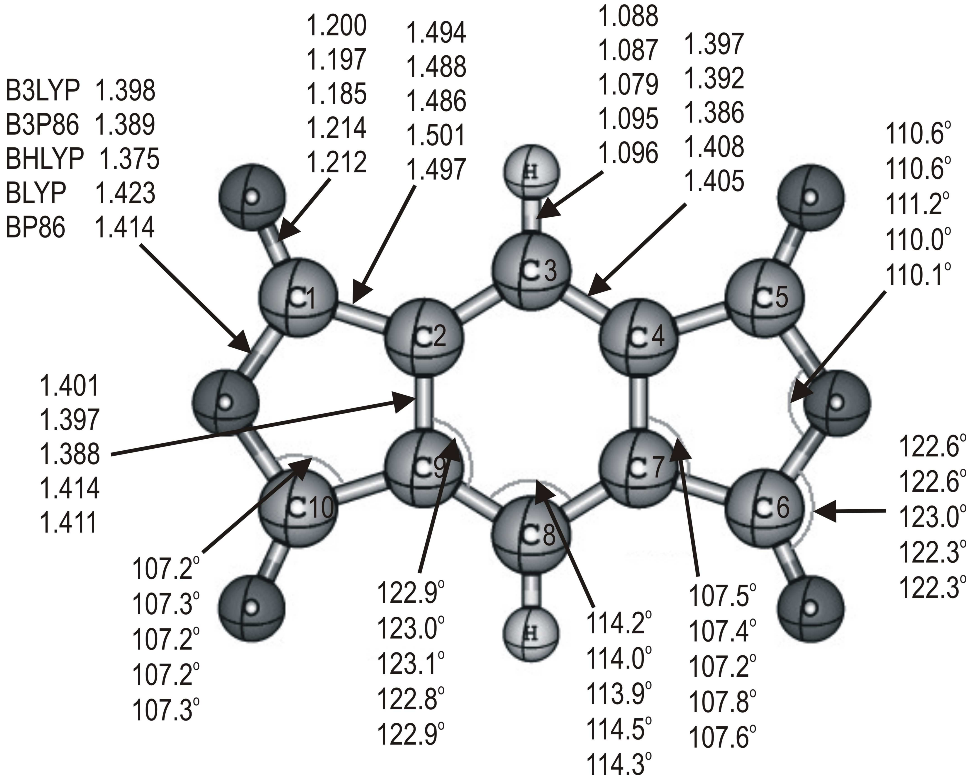

Figure 4.5: Optimized geometry of D_{2h} pyromellitic dianhydride in its ^1A_g ground electronic state. Bond lengths are given in Å.

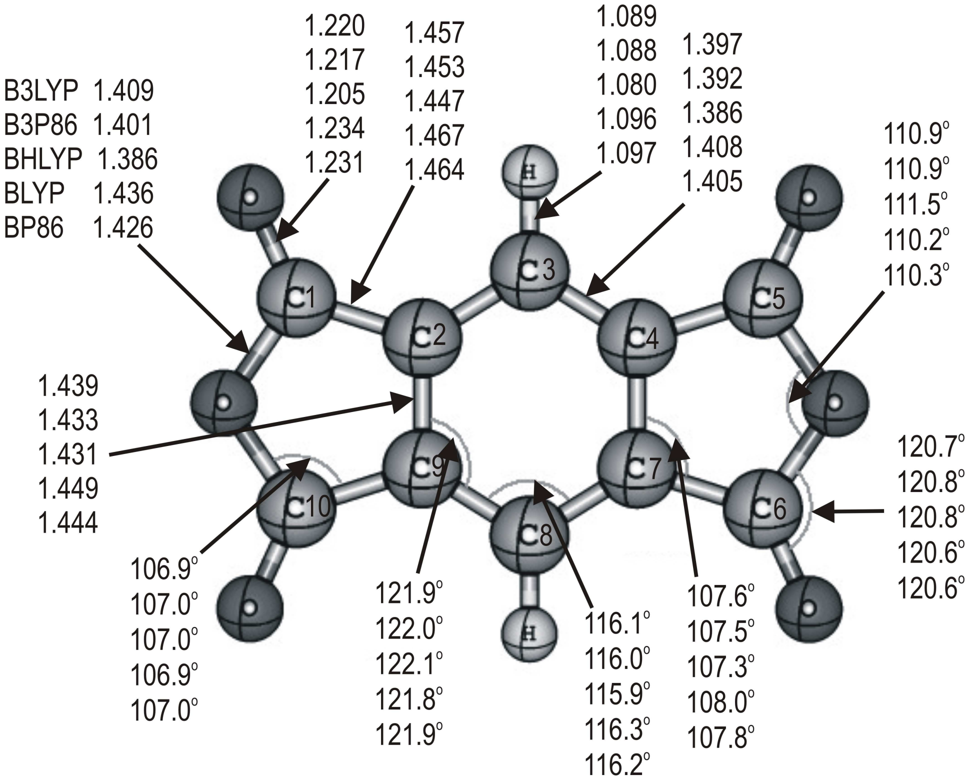

Figure 4.6: Optimized geometry of D_{2h} pyromellitic dianhydride anion in its $^2\mathrm{A}_u$ ground electronic state. Bond lengths are given in Å.

Table 4.1: IR active harmonic vibrational frequencies (cm^{-1}) and intensities (in parentheses km/mol) of C_{2v} maleic anhydride.

mode	B3LYP	B3P86	BHLYP	BLYP	BP86	expt[a]
a_1	3271(1)	3290(1)	3372(2)	3185(0.1)	3193(0.2)	3117
a_1	1905(59)	1930(59)	2023(77)	1803(48)	1827(47)	1852
a_1	1648(3)	1665(4)	1731(3)	1577(3)	1591(3)	1592
a_1	1269(150)	1293(165)	1354(192)	1195(129)	1219(136)	1235
a_1	1068(19)	1067(17)	1111(16)	1035(24)	1031(20)	1060
a_1	874(6)	889(6)	921(6)	830(7)	845(7)	864
a_1	633(1)	639(1)	666(0.5)	603(1)	608(1)	632
a_1	399(10)	403(11)	422(14)	378(7)	382(8)	403
b_1	841(75)	841(75)	883(88)	809(65)	806(66)	839
b_1	635(0.03)	638(0.004)	668(0.2)	607(0.01)	609(0.1)	642
b_1	164(3)	164(3)	168(4)	159(3)	159(3)	173
b_2	3250(1)	3269(1)	3351(2)	3164(0.04)	3172(0.1)	3117
b_2	1843(716)	1868(717)	1953(877)	1747(603)	1771(601)	1782
b_2	1322(2)	1325(1)	1383(0.4)	1276(2)	1274(2)	1305
b_2	1060(67)	1075(87)	1140(123)	1001(33)	1012(44)	1054
b_2	913(134)	935(120)	995(104)	823(127)	849(130)	889
b_2	701(38)	707(32)	740(26)	662(65)	671(50)	697
b_2	554(3)	558(2)	580(2)	530(6)	534(4)	557

[a] Experimental values taken from Rogstad [82].

Table 4.2: IR active harmonic vibrational frequencies (cm^{-1}) and intensities (in parentheses km/mol) of C_{2v} maleic anhydride anion.

mode	B3LYP	B3P86	BHLYP	BLYP	BP86
a_1	3238(14)	3259(12)	3344(6)	3147(24)	3157(22)
a_1	1750(263)	1779(260)	1844(331)	1667(221)	1694(220)
a_1	1444(36)	1461(33)	1504(48)	1390(29)	1405(27)
a_1	1266(58)	1291(64)	1354(80)	1192(41)	1217(48)
a_1	1031(21)	1032(20)	1071(23)	1000(20)	997(19)
a_1	919(6)	934(5)	975(3)	866(7)	882(7)
a_1	628(7)	634(7)	663(8)	596(6)	602(6)
a_1	384(3)	388(4)	407(5)	362(2)	367(2)
b_1	717(51)	723(48)	768(58)	674(49)	677(42)
b_1	629(44)	629(48)	654(55)	606(35)	604(43)
b_1	196(2)	198(2)	206(2)	187(1)	188(1)
b_2	3219(33)	3240(31)	3325(27)	3126(41)	3137(41)
b_2	1671(1087)	1701(1089)	1753(1343)	1596(923)	1624(923)
b_2	1325(5)	1330(5)	1384(0.2)	1278(11)	1278(10)
b_2	1075(8)	1082(9)	1122(1)	1034(12)	1037(14)
b_2	844(48)	875(50)	942(29)	751(27)	781(51)
b_2	730(41)	734(33)	766(25)	688(88)	699(58)
b_2	569(2)	573(1)	599(0.3)	542(5)	546(3)

Table 4.3: IR active harmonic vibrational frequencies (cm^{-1}) and intensities (in parentheses km/mol) of C_{2v} phthalic anhydride.

mode	B3LYP	B3P86	BHLYP	BLYP	BP86	expt^a
a_1	3222(6)	3240(6)	3324(5)	3137(9)	3145(8)	3090
a_1	3207(4)	3227(4)	3309(4)	3122(6)	3131(5)	3069
a_1	1900(225)	1926(223)	2014(256)	1802(203)	1827(201)	1852
a_1	1655(0.2)	1677(0.2)	1735(0.3)	1586(0.2)	1606(0.2)	1599
a_1	1495(0.04)	1503(0.7)	1561(0.3)	1442(0.05)	1445(0.1)	1517
a_1	1400(17)	1426(15)	1430(66)	1364(8)	1391(7)	1336
a_1	1278(271)	1300(285)	1343(285)	1217(216)	1238(233)	1258
a_1	1179(10)	1181(14)	1218(11)	1148(12)	1145(13)	1213
a_1	1123(48)	1137(37)	1183(34)	1066(61)	1080(50)	1107
a_1	1027(5)	1035(5)	1065(4)	993(7)	1000(6)	1006
a_1	743(0.3)	748(0.2)	775(0.1)	715(0.6)	719(0.5)	734
a_1	636(4)	641(3)	668(3)	606(4)	611(3)	643
a_1	535(3)	538(3)	560(5)	512(1)	515(1)	536
a_1	351(8)	354(9)	369(11)	336(6)	338(7)	355
b_1	997(1)	993(1)	1039(1)	964(1)	954(1)	922
b_1	815(21)	812(18)	848(13)	791(27)	782(25)	800
b_1	724(75)	725(78)	761(98)	692(57)	691(61)	714
b_1	423(0.5)	418(0.6)	437(0.6)	412(0.4)	405(0.6)	212
b_1	196(0.00)	194(0.03)	202(0.004)	191(0.01)	188(0.01)	188
b_1	163(4)	162(4)	168(5)	158(4)	157(4)	173
b_2	3218(2)	3237(1)	3320(0.5)	3133(4)	3141(3)	3059
b_2	3196(1)	3215(1)	3297(1)	3110(2)	3119(1)	3049
b_2	1844(693)	1869(694)	1951(815)	1751(603)	1776(602)	1762
b_2	1647(8)	1668(6)	1730(4)	1577(11)	1595(8)	1610
b_2	1490(11)	1498(12)	1555(15)	1437(8)	1442(9)	1471
b_2	1300(0.3)	1300(0.4)	1354(1)	1260(0.1)	1255(0.1)	1243
b_2	1185(2)	1192(3)	1235(8)	1146(1)	1150(1)	1175
b_2	1096(1)	1100(2)	1139(4)	1060(1)	1063(1)	1070
b_2	932(262)	964(260)	1046(277)	819(238)	855(240)	906
b_2	838(3)	842(2)	877(3)	806(3)	808(2)	839
b_2	677(3)	679(3)	707(3)	651(4)	651(3)	679
b_2	537(10)	540(9)	563(7)	512(17)	516(13)	409
b_2	247(1)	246(1)	256(1)	239(1)	238(1)	256

^{a}Experimental values taken from Hase [83].

Table 4.4: IR active harmonic vibrational frequencies (cm^{-1}) and intensities (in parentheses km/mol) of C_{2v} phthalic anhydride anion.

mode	B3LYP	B3P86	BHLYP	BLYP	BP86
a_1	3187(45)	206(44)	3291(37)	3099(56)	3107(57)
a_1	3165(17)	185(14)	3268(15)	3076(19)	3086(15)
a_1	1763(632)	792(627)	1853(792)	1681(533)	1710(530)
a_1	1566(109)	1587(109)	1635(156)	1505(81)	1523(81)
a_1	1476(6)	1493(12)	1536(13)	1425(3)	1440(8)
a_1	1400(56)	1418(44)	1448(105)	1356(38)	1370(28)
a_1	1288(3)	1309(6)	1366(4)	1224(1)	1243(3)
a_1	1152(2)	1152(5)	1197(11)	1118(1)	1114(1)
a_1	1091(47)	1108(47)	1157(41)	1028(42)	1046(45)
a_1	991(47)	1000(46)	1024(49)	960(49)	967(46)
a_1	739(1)	745(1)	770(4)	711(1)	716(1)
a_1	638(16)	643(15)	673(19)	606(15)	612(14)
a_1	531(8)	534(2)	556(1)	508(3)	511(6)
a_1	344(5)	346(5)	361(5)	327(4)	330(4)
b_1	959(1)	955(1)	1008(1)	921(2)	912(2)
b_1	751(42)	747(35)	784(22)	726(51)	716(47)
b_1	691(55)	695(61)	737(88)	651(36)	654(40)
b_1	428(6)	425(7)	443(8)	416(5)	411(6)
b_1	219(2)	220(2)	230(3)	209(1)	209(1)
b_1	172(4)	170(3)	174(3)	169(4)	166(3)
b_2	3179(56)	3198(54)	3284(46)	3090(71)	3098(71)
b_2	3150(9)	3171(8)	3253(12)	3062(8)	3072(7)
b_2	1682(1049)	1711(1072)	1765(1200)	1608(926)	1636(946)
b_2	1537(304)	1555(300)	1599(378)	1481(243)	1496(231)
b_2	1464(76)	1476(54)	1512(232)	1416(34)	1424(20)
b_2	1287(16)	1289(10)	1336(51)	1246(8)	1243(4)
b_2	1184(22)	1189(18)	1230(20)	1146(23)	1148(19)
b_2	1094(1)	1097(1)	1138(2)	1057(3)	1058(2)
b_2	839(4)	848(2)	893(2)	804(1)	806(1)
b_2	793(5)	823(3)	836(14)	709(28)	747(27)
b_2	670(3)	672(3)	701(7)	642(1)	643(1)
b_2	533(3)	536(3)	557(1)	507(8)	512(6)
b_2	243(2)	241(3)	250(1)	236(7)	234(4)

Table 4.5: IR active harmonic vibrational frequencies (cm^{-1}) and intensities (in parentheses km/mol) for D_{2h} pyromellitic dianhydride (PMDA).

mode	B3LYP	B3P86	BHLYP	BLYP	BP86	expt[a]
b_{1u}	3226(8)	3243(9)	3327(12)	3142(4)	3148(5)	3056
b_{1u}	1856(1248)	1881(1249)	1965(1486)	1761(1077)	1786(1074)	1775
b_{1u}	1483(10)	1501(12)	1555(18)	1420(6)	1436(8)	1373
b_{1u}	1170(2)	1177(4)	1222(9)	1127(0.4)	1131(1)	1306
b_{1u}	945(506)	977(504)	1060(545)	831(442)	867(454)	924
b_{1u}	761(27)	766(21)	802(20)	723(49)	728(32)	767
b_{1u}	566(6)	569(5)	591(4)	544(11)	547(8)	656
b_{1u}	162(8)	162(7)	169(8)	156(8)	156(7)	488
b_{2u}	1903(434)	1929(430)	2018(494)	1804(396)	1829(390)	1854
b_{2u}	1477(7)	1488(14)	1546(9)	1422(5)	1431(14)	1411
b_{2u}	1423(17)	1453(13)	1443(53)	1390(9)	1415(2)	1276
b_{2u}	1235(719)	1256(736)	1312(786)	1166(608)	1186(634)	1238
b_{2u}	1087(22)	1091(13)	1134(14)	1044(47)	1048(26)	1119
b_{2u}	737(0.5)	747(0.5)	770(2)	706(0.02)	715(0.03)	1075
b_{2u}	628(3)	635(2)	661(3)	597(4)	603(3)	581
b_{2u}	385(26)	388(27)	406(36)	365(18)	368(20)	364
b_{3u}	964(15)	959(14)	1005(13)	933(17)	922(16)	904
b_{3u}	726(68)	729(68)	766(90)	693(52)	693(52)	710
b_{3u}	426(1)	421(1)	440(1)	416(0.4)	408(1)	392
b_{3u}	168(4)	168(4)	173(5)	163(4)	162(4)	202
b_{3u}	101(14)	99(13)	103(15)	99(13)	96(12)	138

[a] Experimental values taken from Hase [63].

Table 4.6: IR active harmonic vibrational frequencies (cm^{-1}) and intensities (in parentheses km/mol) for D_{2h} pyromellitic dianhydride (PMDA) anion.

mode	B3LYP	B3P86	BHLYP	BLYP	BP86
b_{1u}	3206(3)	3224(2)	3309(2)	3120(6)	3127(5)
b_{1u}	1770(1645)	1798(1639)	1865(1926)	1685(1439)	1712(1428)
b_{1u}	1498(13)	1516(16)	1565(9)	1437(15)	1453(18)
b_{1u}	1185(15)	929(372)	1233(9)	1143(17)	1148(19)
b_{1u}	895(373)	770(25)	1006(376)	785(338)	823(359)
b_{1u}	766(33)	770(25)	806(24)	729(61)	734(35)
b_{1u}	581(10)	584(8)	607(8)	558(16)	560(12)
b_{1u}	169(6)	169(6)	176(7)	162(6)	162(6)
b_{2u}	1768(2593)	1797(2574)	1853(2914)	1692(2112)	1719(2090)
b_{2u}	1481(1104)	1505(1121)	1501(2082)	1443(528)	1466(539)
b_{2u}	1402(22)	1416(0.2)	1452 (203)	1356(15)	1366(0.002)
b_{2u}	1243(610)	1264(595)	1325(918)	1172(445)	1193(445)
b_{2u}	1056(25)	1063(27)	1095(160)	1017(0.1)	1022(1)
b_{2u}	760(0.1)	769(0.0001)	796(1)	727(0.2)	736(0.003)
b_{2u}	611(145)	618(140)	643(195)	582(109)	588(105)
b_{2u}	378(12)	382(14)	400(15)	358(9)	362(11)
b_{3u}	957(12)	952(12)	1002(8)	923(15)	912(15)
b_{3u}	728(54)	731(54)	776(77)	687(40)	688(39)
b_{3u}	427(5)	421(5)	436(8)	418(3)	410(4)
b_{3u}	189(5)	190(5)	197(6)	181(4)	181(5)
b_{3u}	103(12)	101(11)	103(11)	102(12)	99(11)

of a stable anion. It is also observed that in all cases the ZPVE corrected AEA yields a more positive value.

4.3.1 Maleic anhydride

The IR and Raman spectra for maleic anhydride were originally published by Mirone [84], oriented crystalline samples of deuterated and undeuterated samples were published later by Di Lauro [85]. Finally, the vapor phase IR spectrum was published by Rogstad [82]. Table 4.1 compares the theoretical IR active harmonic frequencies to the IR values from the vapor phase data of Rogstad [82]. Under C_{2v} symmetry, there are twenty-one fundamental vibrations in which eight of a_1, three of b_1, and seven of b_2 symmetry are IR and Raman active, while three of a_2 symmetry are only Raman active. The level of performance of the DFT functionals used with the DZP++ basis can be determined by calculating the mean absolute percent deviation from the experiment: B3LYP(2.1%), B3P86(2.8%), BHLYP(6.8%), BLYP(4.3%) and BP86(3.2%) while not considering the Raman active only a_2 modes in the error analysis. These results generally are considered to be very good considering that anharmonicity is not accounted for in the calculation. The B3LYP functional gives the best results while the BHLYP yields the worst.

Figures 4.1 and 4.2 give the optimized geometrical parameters for maleic anhydride and its respective anion. The anion geometry altered the bond length of the C=O bond by $\sim$ +0.04Å, the C-O anhydride bond by $\sim$ +0.02Å, the C-C bond by $\sim$ -0.06Å, and the C=C bond by $\sim$ +0.06Å. A population analysis using the natural charges and bond orbitals [86] indicates that the excess electron will tend towards localizing in the anti-bonding π^* orbitals of the C=O and C=C bonds.

The derivative of the energy with respect to an applied static electric field yields the electric dipole moment. The excess electron results in a decrease in the B3LYP calculated static electric dipole moment from 4.4D for the neutral to 2.6D for the anion and is accompanied by a slight compression of the molecule along the C_2 axis of about 0.06Å. The second derivative of the energy with respect to an applied electric field yields the static electric polarizability. The anion results in a 32% increase in the mean polarizability from 53.30 Bohr^3 to 70.46 Bohr^3.

The theoretical predictions of the electron affinity consistently overestimate the experimental values listed in Table 4.7. The experimental values range from 1.3 eV to 1.6 eV with a mean value about 1.4 eV [87, 88]. The DFT functional BHLYP result of 1.54 eV is closest to the experimental values. I believe that this over-estimation of the electron affinity is attributible to the incomplete cancellation of the electron self-interaction term and an incorrect asymptotic potential intrinstic to all current DFT functionals [74, 89]. Recall from Hartree-Fock theory that the self-interaction problem arises when $i = j$ in the Coulomb operator and describes the unphysical situation of an electron interacting with itself. However, in HF theory the exchange operator takes care of this particular problem at $i = j$ by exactly cancelling the Coulomb term. In DFT, the total energy is varied via the Kohn-Sham partioning of Equation

4.9 and necessarily reqires the exact $E_{XC}[\rho]$ to cancel the self-interaction term contained in $J[\rho]$. Since the exact XC functional is unknown, the use of the current *approximate* functionals necessarily introduces what is known as the self-interaction error [74]

$$SIE = J[\rho] + E_{XC}[\rho]. \tag{4.20}$$

This error can be significant, especially in the case of odd-electron systems such as anions [90]. However, it is widely speculated that the self-interaction error can be effectively "spread out" over larger molecular anions such that more reasonble calculations of the electron affinity can be made [89]. On the other hand, the problem becomes much more severe for localized charge as is the case with atomic anions [90] and bonds with localized electron densities [91]. Clearly, the localization of the excess electron population on the carbonyl and C=C bonds of maleic anhydride must contribute to the error between the theoretical and experimental values.

4.3.2 Phthalic anhydride

The IR and Raman spectra of phthalic anhydride were reported originally by Hase [83] for poly-crystalline samples. Crystalline phthalic anhydride belongs to the C_{2v}^{9} space group and the C_1 site group with four molecules per unit cell [92]. However, C_{2v} molecular symmetry was assumed for the normal coordinate analysis of the free molecule as a first approximation. Under C_{2v} symmetry, there are thirty-nine fundamental vibrations in which fourteen of a_1, six of b_1, and thirteen of a_2 symmetry are IR and Raman active, while six of a_2

symmetry are only Raman active. Table 4.3 compares the theoretical IR harmonic frequencies to the experimental values of Hase [83]. I find that the mean absolute percent deviation is, on average, larger for phthalic anhydride when compared to the maleic anhydride results: B3LYP(6.6%), B3P86(7.1%), BHLYP(10.5%), BLYP(6.7%) and BP86(6.3%) with the six Raman only a_2 modes not considered in the error analysis. This increase in error is attributable directly to the gross over estimation of the experimental b_1 212 cm^{-1} and b_2 409 cm^{-1} modes. Removal of these two theoretical harmonic frequencies results in a more reasonble agreement with the experimental values: B3LYP(2.9%), B3P86(3.5%), BHLYP(6.6%), BLYP(3.4%), and BP86(3.1%). Once more, the B3LYP gives the best result while the BHLYP gives the worst result.

Figures 4.3 and 4.4 give the optimized geometrical parameters for phthalic anhydride and its anion. The anion geometry altered the C=O bonds by $\sim$ +0.03Å and the C-O anhydride bonds by $\sim$ +0.01Å. The C1-C2 bonds and C3-C4 bonds are shortened by $\sim$ -0.05Å and -0.01Å, respectively, while the C2-C3 bonds, C4-C5 bond, and C2-C7 bond are lengthened by $\sim$ +0.02Å, +0.03Å, and +0.04Å, respectively. The natural bond order analysis [86] reveals that the excess charge populates the C=O π^* orbitals and the π^* orbitals of the phenyl ring. The LUMO of phthalic anhydride is a mixture of about 48% of the C=O π^* orbitals and 42% of the phenyl ring π^* orbitals indicating that the excess electron is more delocalized over the phenyl portion of the molecule.

The energy derivative with respect to an applied static electric field gives an electric dipole moment of 6.2D for the neutral species and 5.9D for the anion. The energy second derviatives compute an increase in the static mean polarizability for the anion by about 27% from 97.7 Bohr^3 to 124.4 Bohr^3

The theoretical predictions for the adiabatic electron affinity (Table 4.7) give mixed results as in the case for maleic anhydride. The experimental values range from 1.2 eV to 1.3 eV. The BHLYP functional yields the closest result yet under-estimates the experimental value by about -0.1 eV. The BLYP(+0.1 eV) and B3LYP(+0.2 eV) functionals produce reasonbly adequate results. Better agreement seems to be due to greater delocalization of the excess charge over the π^* system of the phenyl ring.

4.3.3 Pyromellitic dianhydride

The IR and Raman spectra for poly-crystalline pyromellitic dianhydride have been published by Hase. Crystalline PMDA belongs to the space group C_{4h}^4 ($P4_2/n$) and has a quasi-planar structure close to D_{2h} symmetry [64]. Normal coordinate analysis of the experimental spectra were based on the idealized D_{2h} molecular symmetry [63]. Under D_{2h} symmetry, there are forty-eight fundamental vibrations of which nine of a_g, three of b_{1g}, four of b_{2g}, and eight of b_{3g} symmetry are only Raman active, and eight of b_{1u}, eight of b_{2u}, and five of b_{3u} symmetry are only IR active, while three of a_u symmetry are inactive for both IR and Raman. Table 4.5 compares the theoretical IR harmonic frequencies to the experimental values of Hase [63]. I find that the mean absolute percent deviation from the experimental values is somewhat larger than for the previous two molecules (maleic anhydride and phthalic anhydride): B3LYP(11.5%), B3P86(12.0%), BHLYP(14.2%), BLYP(11.6%), and BP86(11.4%). In a separate calculation, I have used the large cc-pVQZ basis set in combination with the B3LYP functional to test for basis-set error due to the finite size of the smaller DZP++ basis set and found negligible improvement with the larger basis set. Clearly, the lack of agreement may in part be due to anharmonicity effects but most likely are due largely to the assumption of idealized D_{2h} molecular symmetry used in the DFT calculations. Distortions in the molecular geometry of solid-phase PMDA due to crystal field effects likely contribute to the disagreement between theory and experiment. Thus, it would be more useful to calculate the optimized structure of the crystalline material in order to directly compare theoretical harmonic frequencies with the known experimental values. That reasonbly good agreement is achieved assuming a C_{2v} molecular symmetry for phthalic anhydride seems to indicate that my approximation for the idealized molecular geometry of phthalic anhydride is more valid than the D_{2h} symmetry assumption for PMDA.

Figures 4.5 and 4.6 give the optimized geometrical parameters for PMDA and PMDA anion. The anion geometry altered the C=O bonds by $\sim$ +0.02Å and the C-O anhydride bonds by $\sim$ +0.01Å. The C1-C2 and C9-C10 bonds were shortened by $\sim$ -0.04Å and the C2-C9 and C4-C7 bonds were lengthened by $\sim$ +0.04Å. The C2-C3, C3-C4, C7-C8, and C9-C9 bonds all demonstrated negligible changes. Natural bond order analysis [86] reveals that the excess charge populates the C=O π^* orbitals and the C=C π^* orbitals of the two C-C bonds that fuse the anhydride rings to the phenyl ring. The excess electron appears *less* delocalized over the π-system of the phenyl ring than was calculated for phthalic anhydride. This may be conceptualized as a localization of charge on the two anhydride groups rather than a delocalization over the the entire molecule. Since PMDA possesses an inversion center by virtue of the D_{2h} molecular symmetry, there is zero net dipole moment. However, the formation of the anion results in a 33% increase in the mean static polarizability from 130.7 Bohr^3 to 173.3 Bohr^3.

The theoretical predications for the adiabatic electron affinity (Table 4.7) are poor when compared to the experimental values although the BH-LYP(+0.6 eV) functional once more gives the most reasonable result. The B3P86 over-estimates the electron affinity by about 1.4 eV and the BP86 over-estimates the electron affinity by nearly 1 eV. The B3LYP and BLYP functionals provide nearly the same level of performance but are off by about +0.8 eV. Such poor results are due to the presence of the second anhydride ring, and the tendency for increased charge localization on these moieties. Evidently, this leads to a large contribution to the self-interaction error that none of the XC functionals used are able to compensate.

I have explored the influence of basis-set size on the prediction of the adiabatic electron affinities summarized in Table 4.8. I have also included calculations utilizing Handy's OPTX modification of Becke's exchange functional [93] combined with the ever popular LYP correlation functional as well as

Becke's 1995 gradient-corrected correlation functional [94] which produce the OLYP and OB95 DFT XC functionals. The choice of the OPTX (O) exchange functional is due to its reported improved performance of the Becke 1988 exchange functional in terms of better energetic and structural predictions. The Becke 1995 (B95) gradient-corrected correlation functional has been chosen because it correctly cancels the Coulomb self-repulsion error for one-electron systems [94]. This should reduce the electron self-repulsion error that seems to plague the theoretical predictions for adiabatic electron affinities. The results tabulated in Table 4.8 demonstrate a modest improvement in the aggreement between theoretical and experimental values as larger basis-sets are used for a given functional. In every case, the adiabatic electron affinities are lowered and seem to converge with the aug-cc-pVTZ basis. For maleic anhydride, the combination of OB95/aug-cc-pVTZ produces the best agreement with experiment. Very little difference is observed between the OLYP and OB95, although the OB95 XC functional produces consistently lower results for all three molecules. The BHLYP XC functional consistently under-estimates the electron affinity for phthalic anhydride. Schaefer observed a similar performance with BHLYP in his comprehensive study of "medium ring" compounds which included maleic anhydride [?]. Finally, PMDA still remains problematic although a systematic lowering of the electron affinity is observed. Both the BHLYP and OB95 are comparable when using the large aug-cc-pVTZ basis set. Clearly the additional anhydride ring causes significant problems for DFT in that the excess electron is more localized at the ends of the molecule rather than “spreading out” over the phenyl π-system. It is likely that PMDA qualifies as one of those “difficult” molecules frequently encountered in many other systematic studies.

Table 4.7: Ground state energies (Hartrees) and adiabatic electron affinities (eV) of organic anhydrides and their anions using the DZP++ basis-set and the DFT functionals B3LYP, B3P86, BHLYP, BLYP, and BP86. The harmonic zero point vibrational energy (ZPVE) corrected adiabatic electron affinities are listed in parentheses.

molecule	B3LYP	B3P86	BHLYP	BLYP	BP86	expt
$C_4H_2O_3$	-379.369967	-380.254861	-379.169246	-379.295814	-379.382039	
$C_4H_2O_3^-$	-379.433819	-380.338749	-379.225810	-379.355300	-379.448497	
AEA	1.74(1.80)	2.28(2.34)	1.54(1.61)	1.62(1.68)	1.81(1.87)	[a]1.44(9), [a]1.44, [a]1.40, [a]1.42(5), [b]1.6, [b]1.33
$C_8H_4O_3$	-533.047710	-534.402956	-532.758911	-532.906397	-533.057678	
$C_8H_4O_3^-$	-533.099628	-534.475105	-532.800850	-532.955880	-533.114491	
AEA	1.41(1.50)	1.96(2.05)	1.14(1.24)	1.35(1.43)	1.55(1.63)	[a]1.25(5), [a]1.245, [a]1.25(5), [b]1.3, [b]1.18
$C_{10}H_2O_6$	-833.806913	-835.760473	-833.371933	-833.643030	-833.837355	
$C_{10}H_2O_6^-$	-833.912391	-835.886532	-833.467503	-833.746561	-833.948294	
AEA	2.87(2.93)	3.43(3.49)	2.60(2.68)	2.82(2.87)	3.02(3.07)	[b]2.04, [b]1.94

[a]References within [87], [b] Reference [88]

Table 4.8: Adiabatic electron affinities (eV) of the organic anhydrides studied using the DFT functionals BHLYP, B3LYP, BLYP, OLYP, and OB95. The variation in the adiabatic electron affinities with basis set selection for each functional is demonstrated.

molecule/method	BHLYP	B3LYP	BLYP	OLYP	OB95
maleic anhydride					
DZP++	1.54	1.74	1.62	1.53	1.50
aug-cc-pVDZ	1.48	1.69	1.58	1.48	1.45
aug-cc-pVTZ	1.43	1.65	1.54	1.45	1.42
phthalic anhydride					
DZP++	1.14	1.41	1.35	1.26	1.25
aug-cc-pVDZ	1.11	1.38	1.32	1.22	1.21
aug-cc-pVTZ	1.07	1.33	1.28	1.20	1.19
pyromellitic dianhydride					
DZP++	2.60	2.87	2.82	2.72	2.72
aug-cc-pVDZ	2.53	2.80	2.77	2.66	2.65
aug-cc-pVTZ	2.48	2.77	2.73	2.63	2.62

4.4 Electronic structure of the anhydrides and their anions.

Recently, time-dependent density functional response theory (TDDFT) has been developed in order to predict discrete electronic transition energies and oscillator strengths. A full theoretical treatment has been provided by Casida [95, 96]and will be introduced here briefly. The reader is referred to a formal review of the method by Gross and Kohn [97].

The time-dependent Kohn-Sham equation is given by

$$\left[-\frac{1}{2}\nabla^2 + V_{eff}(\boldsymbol{r},t)\right]\psi(\boldsymbol{r},t) = i\frac{\partial}{\partial t}\psi(\boldsymbol{r},t) \tag{4.21}$$

assuming there exists an effective potential V_{eff} for an indendent particle system whose orbitals $\psi(\boldsymbol{r},t)$ give the real density $\rho(\boldsymbol{r},t)$ of the interacting system. The potential is expressed as

$$V_{eff} = V(t) + V_{ee}(\boldsymbol{r},t) + V_{XC}(\boldsymbol{r},t) \tag{4.22}$$

where an applied field (peturbation) $V(t)$ is slowly turned on. The XC potential is expressed as the functional derivative of the exchange-correlation action $A_{XC}[\rho]$ with respect to the time-dependent electron density and is approximated as the functional derivative of the time-independent E_{XC} with respect to the charge density at time t,

$$V_{XC}[\rho(\boldsymbol{r},t)] = \frac{\partial A_{XC}[\rho]}{\partial\rho(\boldsymbol{r},t)} \approx \frac{\partial E_{XC}[\rho]}{\partial\rho_t(\boldsymbol{r})} = V_{XC}[\rho_t(\boldsymbol{r})]. \tag{4.23}$$

and is known as the *adiabatic approximation* because the zero-frequency limit of A_{XC} is used for handling frequency-dependent perturbations. The excitation energies are computed in terms of the ground state electron density and hence ground state properties of the system determine the excited states of the system. The application of the external perturbation results in a linear response of the electron density. The response of the electric dipole moment to a time varying electric field is defined by the *dynamic* polarizability, $\alpha(\omega)$, which may be computed from the response of the electronic density by time-dependent density functional response theory. The electronic excitation spectrum may then be calculated by finding poles in the dynamic polarizability through the usual sum-over-states relationship

$$\alpha(\omega) \propto \sum_i \frac{f_i}{\omega_i^2 - \omega^2}, \tag{4.24}$$

where the excitation enegies are given by ω_i with oscillator strength f_i.

The electronic absorption spectra for phthalic anhydride and PMDA and their respective anions have been measured previously and the absorption maxima are listed in Tables 4.9 - 4.12 along with the theoretically predicted values. I find that in all cases the aggreement with experiment is quite satisfactory and generally within 0.2 eV of the measured values. The dominant electronic transitions are associated with $\pi \rightarrow \pi^*$ excitations of the carbonyl and phenyl π-systems. The experimental absorption onset generally is observed around 4 eV (310 nm) for both neutral molecules which is typical for aromatic molecules. On the other hand, the first excited state transition energy is dramatically red-shifted upon the formation of the anion. For phthalic anhydride anion, the first experimentally observed electronic transition is observed at 1.23 eV with very low intensity, while an intense and narrow transition at

1.86 eV is observed for the experiments PMDA anion. The DFT calculations qualitatively reproduce this trend with the predicated first excited state transition energy for phthalic anhydride anion at 1.21 eV (f=0.0061), while the predicted first excited state for PMDA anion occurs at 1.99 eV (f=0.1491).

Table 4.9: Vertical excitation energies (eV) for C_{2v} phthalic anhydride in its $^1A_1$ ground electronic state using the TD-B3LYP/aug-cc-pVDZ method. Oscillator strengths are listed in parentheses.

molecule	State	Energy	expt[a]
$C_8H_4O_3$	$^1B_1$	4.01(0.0001)	4.13
	$^1A_1$	4.58(0.0409)	4.31
	$^1B_2$	4.79(0.0449)	4.75
	$^1B_1$	5.78(0.0001)	
	$^1B_2$	5.93(0.0295)	
	$^1A_1$	5.96(0.5245)	
	$^1B_2$	6.04(0.2784)	
	$^1A_1$	6.66(0.0099)	
	$^1B_1$	6.93(0.0104)	
	$^1B_2$	7.07(0.0063)	
	$^1B_1$	7.07(0.0002)	
	$^1B_1$	7.26(0.0001)	
	$^1B_2$	7.39(0.0022)	
	$^1B_1$	7.53(0.0223)	
	$^1B_1$	7.55(0.0007)	
	$^1A_1$	7.56(0.1503)	
	$^1A_1$	7.63(0.1527)	

Experimental from NIST [98].

Table 4.10: Vertical excitation energies (eV) for C_{2v} phthalic anhydride anion in its $^2A_2$ ground electronic state using the TD-B3LYP/aug-cc-pVDZ method. Oscillator strengths are listed in parentheses.

molecule	State	Energy	expt[a]
$C_8H_4O_3^-$	$^2B_2$	1.21(0.0061)	1.23
	$^2B_1$	1.86(0.0026)	
	$^2B_2$	3.12(0.0045)	2.90
	$^2A_1$	3.15(0.0914)	3.02
	$^2B_1$	3.65(0.0001)	
	$^2B_2$	3.71(0.0261)	3.70
	$^2A_1$	3.87(0.0071)	
	$^2B_2$	3.99(0.0066)	
	$^2B_1$	4.21(0.0036)	
	$^2B_2$	4.27(0.0249)	4.03
	$^2B_2$	4.30(0.0217)	
	$^2A_1$	4.33(0.0339)	
	$^2A_1$	4.39(0.0273)	
	$^2B_1$	4.54(0.0002)	

[a] Experimental from Shida [99].

Table 4.11: Vertical excitation energies (eV) for D_{2h} pyromellitic dianhydride in its ^1A_g ground electronic state using the TD-B3LYP/aug-cc-pVDZ method. Oscillator strengths are listed in parentheses.

molecule	State	Energy	expt[a]
$C_{10}H_2O_6$	$^1B_{3u}$	3.63(0.0001)	3.99
	$^1B_{2u}$	4.32(0.0568)	4.13
	$^1B_{1u}$	4.61(0.0505)	
	$^1B_{3u}$	5.23(0.0004)	
	$^1B_{1u}$	5.38(0.1363)	
	$^1B_{2u}$	5.66(0.7568)	
	$^1B_{1u}$	5.74(0.1015)	
	$^1B_{2u}$	6.14(0.1469)	

Experimental from Ferstandig [100].

Table 4.12: Vertical excitation energies (eV) for D_{2h} pyromellitic dianhydride anion in its ^2A_u ground electronic state using the TD-B3LYP/aug-cc-pVDZ method. Oscillator strengths are listed in parentheses.

molecule	State	Energy	expt[a]
$C_{10}H_2O_6^-$	$^2B_{2u}$	1.99(0.1491)	1.86
	$^2B_{1u}$	3.41(0.0420)	3.31
	$^2B_{1u}$	3.98(0.0140)	
	$^2B_{2u}$	3.99(0.0473)	
	$^2B_{2u}$	4.14(0.0597)	
	$^2B_{3u}$	4.24(0.0002)	
	$^2B_{1u}$	4.39(0.0109)	
	$^2B_{1u}$	4.72(0.0080)	

[a] Experimental from Shida [99].

4.5 Cluster models for adsorption.

Cluster models have been used in the past to model chemical interactions of adsorbates with metals [101–106], metal oxides [107–111], and semiconductor surfaces [112–116]. Of those accounts, several have computed accurate descriptions of adsorbate geometries, vibrational frequencies, and heats of adsorption. This is of particular importance to the catalysis industry where knowledge of energetics and structure are tantamount for the successful design of new materials. Early computational studies involving transition metal atoms were quite difficult until the advent of pseudopotentials and plane-wave basis-sets. Moreover, advances in high-speed computing has made the computation of transition metal complexes more manageable.

In the following section, I have used cluster models of a copper surface to simulate the adsorption of H_2O and PMDA on Cu(111). The motivation for this work was provided in the previous chapter in which I speculated that the co-adsorption of H_2O with PMDA could be responsible for the previously observed 1.9 eV charge transfer excitation in EELS. I also speculate that the observed effect is due to a polarization of the substrate charge density by adsorbed H_2O which results in an increased electronic overlap between the surface and PMDA The surface-adsorbate complex is conceptualized as a hydrated (or solvated) transition metal salt of the form

$$\mathrm{Cu_{surface}} + (\mathrm{H_2O})_\mathrm{n} + \mathrm{C_{10}H_2O_6} \rightarrow (\mathrm{Cu^+C_{10}H_2O_6^-}) \cdot (\mathrm{H_2O})_\mathrm{n}.$$

It is well known that polar solvents like water modify the surface potential of metals by increasing the energy of the Fermi level with respect to the vacuum level. For alkali metal adsorption, this is easily understood as an ionization of the adsorbate, donating an electron to the surface. For molecules like water where the surface-adsorbate interaction is primarily through σ-donation, the increase in the Fermi energy is generally atributted to the formation of a surface dipole layer [49]. Nevertheless, the net result is a lower potential barrier between the surface and adsorbate which helps facilitate charge transfer across the interface. As was demonstrated in the previous sections, the formation of stable anions of the anhydrides is highly favorable, especially for PMDA, due to the large electron affinities associated with each molecule. For such molecules adsorbing at "surface sites" with excess negative charge, the probability for stable anion formation is likely to be quite large and one would expect to observe electronic and vibrational structure characteristic to the anion.

The ultimate goal of this study was to model the total interation for the H_2O-PMDA/Cu(111) co-adsorbate complex including adsorption energies and vibrational frequencies. However, due to the computational size of such a "real" chemical system, I began by demonstrating that the general phenomenon described above may begin to be realized by first modeling the individual components of the total complex. The calculation of the whole co-adsorbated system shoul be the subject of future work.

Of particular interest is the influence of H_2O adsorption on the HOMO of the copper cluster relative to the affinity levels of PMDA. Clearly the energetic positions of the latter relative to the former will be important in the charge transfer process during the chemisorption of PMDA on Cu(111). Additionally, there is experimental evidence to suggest that PMDA adsorbs at low temepratural in a flat-lying, π-bonded orientation contrary to some previous accounts (see previous chapter). In studying the Cu_{22}-PMDA cluster model my goal to find the optimized structures for both the flat-lying and upright geometries to correlate with the previous experimental observations.

The copper cluster models of Cu_1, Cu_{10} (seven atoms in the first layer and three atoms in the second layer), and Cu_{22} (fourteen atoms in the first layer and eight atoms in the second layer) are illustrated in Figure 4.7. The Cu(111) surfaces are constructed using the bulk lattice parameter of 3.615Å [117]. The first two models have been employed for the study of H_2O adsorption while the last is used for PMDA adsorption. With the exception of the single Cu atom cluster, the geometry of the cluster was held fixed while the adsorbates were fully optimized above the surface. This approximation is justified due to the observation of very little elastic modication of the metal surface by the adsorption of molecules in the low coverage limit [118].

As in the study of the gas phase anhydrides in the previous section, the interaction of H_2O and PMDA on the Cu(111) surface is studied by the density functional methods outlined above. Specifically, I utilize the hybrid HF/DFT B3LYP exchange-correlation functional as implemented in the Gaussian 2003 [81] suite of quantum chemical programs. For the copper atoms, the relativistic effective core potentials derived by Hay and Wadt [119] have been used to describe the $1s-2p$ core while the electrons residing in the $3s$, $3p$, $3d$, $4s$, and

$4p$ shells have been treated explicitly using a standard double-ζ basis set. It is customary to refer to this basis as LANL2DZ. The Pople style split valence basis set 6-31G(d) is used to describe the electron density of C, O, and H, while a diffuse *sp*-function is added to the 6-31G(D) yielding 6-31+G(d) for the H_2O adsorption studies [120, 121].

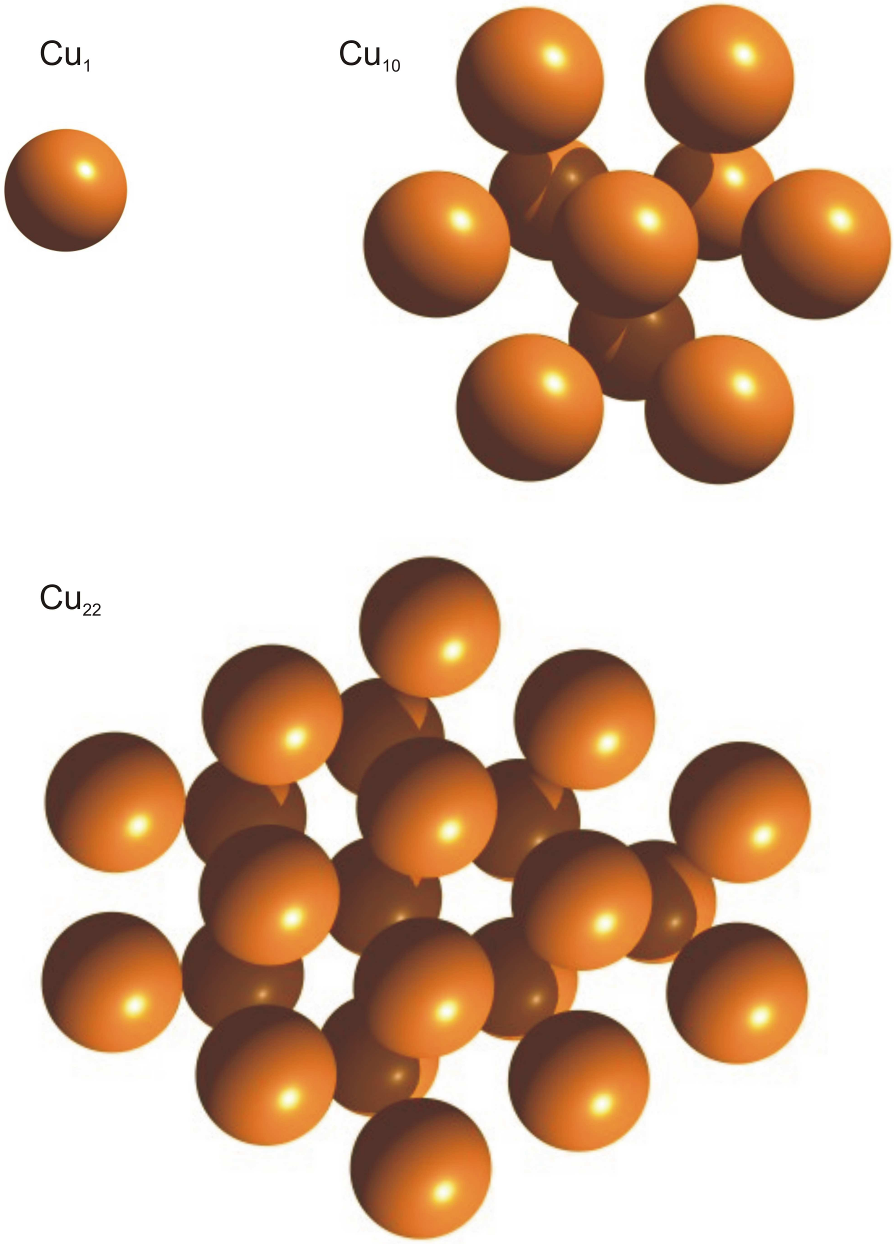

Figure 4.7: Top views of the Cu$_1$, Cu$_{10}$(7,3), and Cu$_{22}$(14,8) clusters used to model the adsorption of H_2O and PMDA on the Cu(111) surface.

4.5.1 Cu-H_2O

Water adsorption on transition metal surfaces has been the subject of numerous theoretical [103–106, 122] and experimental [123–125] works. Thiel and Madey have reported the experimental adsorption energy to be in the range of -40 to -65 kJ/mol, and more recent temperature programmed desorption experiments on the Cu(111) surface report the adsorption energy the between 50-59 kJ/mol. In general, most experimental and theoretical studies find that water adsorbs molecularly to most surfaces through the oxygen atom, while a tendency of forming hydrogen-bonded networks on the surface has been determined by experiement. Most theoretical studies have found that the most favorable orientation for a single H_2O molecule occur in the "H-up" orientation with the molecular plane angled between 55° - 67° away from the surface normal [103–106, 122].

The optimized C_{2v} and C_s geometries for Cu-H_2O are shown in Figures 4.8 and 4.9. The calculation of the harmonic vibrational frequencies yielded a single yet significant imaginary value ($254i$ cm^{-1}) representing a transition state for the C_{2v} cluster. This frequency corresponds to an out-of-plane rocking motion of H_2O reducing the symmetry representation to C_s. Indeed, a lower energy minimum is found at the latter symmetry. The tilt angle (angle between the H_2O plane and surface normal) for the optimized C_s structure was found to be 47.0° which is somewhat smaller than previous theoretical accounts [106, 122, 126]. The Cu-H_2O interaction energy was calculated to be -23.52 kJ/mol for the C_s structure and is in agreement with the previous theoretical accounts albeit significantly lower than experimental values. The results are listed in Table 4.13 along with other theoretical results previously reported for the tilted geometry.

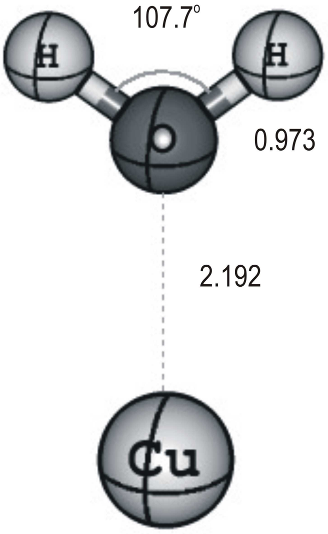

Figure 4.8: Optimized geometry of the C_{2v} Cu-H_2O cluster. Bond lengths are given in Å.

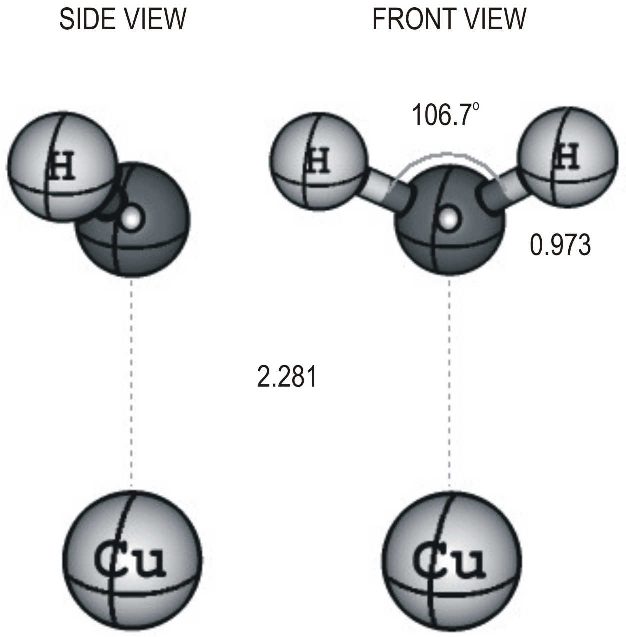

Figure 4.9: Optimized geometry of the C_s Cu-H_2O cluster. Bond lengths are given in Å.

Table 4.13: Interaction energies(kJ/mol) and Cu-O distances(Å) for Cu-H_2O from this work and from literature.

symmetry(tilt)	method	Energy	R_{Cu-O}	ref
C_s (55.4°)	MP2	-25.93	2.27	[106]
C_s (55.4°)	CCSD(T)	-23.40	2.24	[106]
C_s (62°)	DFT (GC-LDA)	-16.9	2.3	[122]
C_s (67°)	SCF-LCAO-Xα	-36.7	2.0	[126]
C_s (47.0°)	B3LYP	-23.52	2.198	This work

4.5.2 Cu_{10}-H_2O

The influence of metal cluster size on the adsorption energy and molecular orientation has been determined using a variety of theoretical methods. For cluster sizes up to twelve atoms, the computed results generally show that H_2O prefers to bind at on-top sites in a tilted geometry similar to the single Cu cluster model. The estimated experimental binding energy for water adsorption Cu(111) has been reported to be about -50 kJ/mol [124]. The C_s optimized structure resulted in a Cu-O bond length of 2.520Å, an O-H bond length of 0.974Å, and H-O-H angle of 105.0°. The H_2O tilt angle was computed to be 79.6° away from the surface normal. The adsorption binding energy, computed as the difference between the total energy of the Cu_{10}-H_2O and the sum of the total energies of the bare Cu cluster and gas phase H_2O, was predicted to be -11.2 kJ/mol and is nearly 40 kJ/mol lower than experimental values. In an MP2 study of water adsorption, the optimal binding energy was calculated to be -41.0 kJ/mol with an optimal tilt angle of 77 degrees [106]. While orientation does not seem to be an issue, clearly the estimation of the binding energy with the current B3LYP method does not aggre with experiment. In the MP2 study, the counterpoise (CP) method was used for correcting basis-set superposition error (BSSE) which has been shown to be significant in the H_2O-copper interaction [106]. Since I have not included this correction in my calculations, this is the likely cause of the observed differences in comparing the two methods. Counterpoise corrected MP2 binding energies with the Cu_{10} model have been computed to be about -12 kJ/mol which is close to my uncorrected value of -11.2 kJ/mol using the B3LYP method. Neither method agrees with experiment and seems to indicate that the current cluster models used for H_2O adsorption should not be used for an accurate calculation of adsorbate-substrate binding energies.

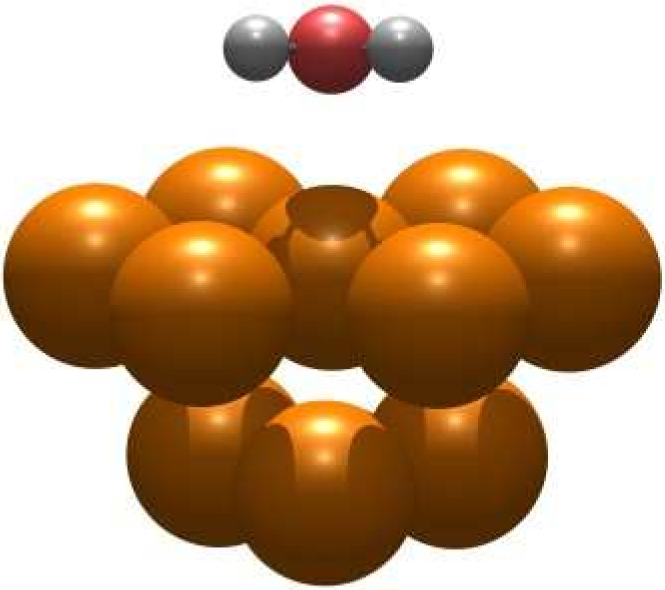

Figure 4.10: Optimized geometry of the C_s Cu_{10}-H_2O cluster.

4.5.3 Cu_{22}-PMDA

Previous theoretical treatments of adsorbate-surface interactions using cluster models have beem limited to small molecules including H_2O, CO, O_2, C_2H_2, and H_2CO. This limitation is due to simple bonding geometries and the ability to use small clusters. As the size of the adsorbate is increased, one naturally must use larger cluster models for the surface in order to minimize the influence of the atoms at the edges of the cluster. In order to model PMDA adsorption I have started with the highest possible symmetry and smallest possible cluster in order to reduce the computational effort as much as possible without introducing too many ill effects from edge interactions. Initially, this was accomplished by starting with an idealized, upright adsorption model for chemisorbed PMDA on Cu_{22} assuming C_s symmetry. This model is meant to approximate the upright, room temperature structure previously determined by HREELS (this work and others [56, 57]) without considering the π bonding interactions of the phenyl ring.

The C_s optimized structure resulted in more than one imaginary frequency indicating that a stationary state had not yet been obtained. The symmetry was subsequently relaxed to C_1 symmetry by breaking the plane of symmetry through the surface carboxylate group. The C_1 optimized structure was found to be a stationary point with all real harmonic frequencies and is depicted in Figure 4.11. Previous experimental results have postulated that room temperature adsorption of PMDA on Cu(111) results in a species bonded to the surface through the unsatisfied valence on the β-carbon of the phenyl ring and a surface caboxylate group with inequivalent C-O bonds [56, 57, 60]. The theoretical results demonstrate that one oxygen on the carboxylate is about 0.08Å closer to the surface than the other. The long C_2 axis on the intact portion of the molecule is directed away from the surface normal by about 49° wheras experimental results have estimated that angle to be closer to 60°. Additionally, the short C_2 axis is found to be tilted away from the surface normal by about 5.5°. To the best of my knowledge, this is the first theoretical treatment of PMDA adsorption and the results appear to be qualitatively consistent with the previous room temperature models deduced from experimental data. The harmonic vibrational frequencies of the adsorbate have been determined and are plotted as a "spectrum" in Figure 4.12 with the room temperature HREELS data from the previous chapter. Unfortunately, the low temperature, π-bonded adsorbate structure has yet to be determined. As I have already determined by experiment, the parallel adsorption geometry appears to be the dominant species at low temperature.

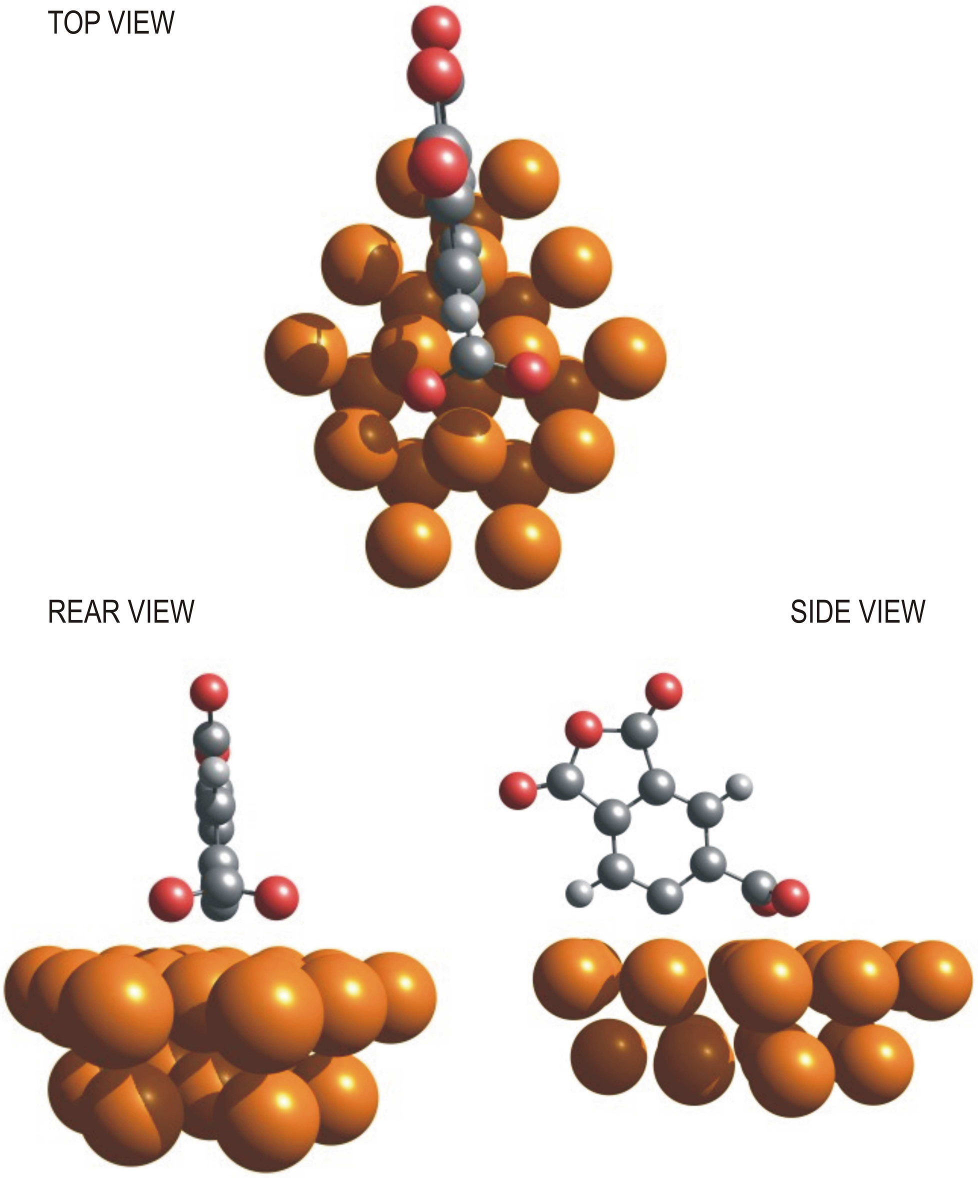

Figure 4.11: Optimized geometry of the C_1 Cu$_{22}$-PMDA cluster.

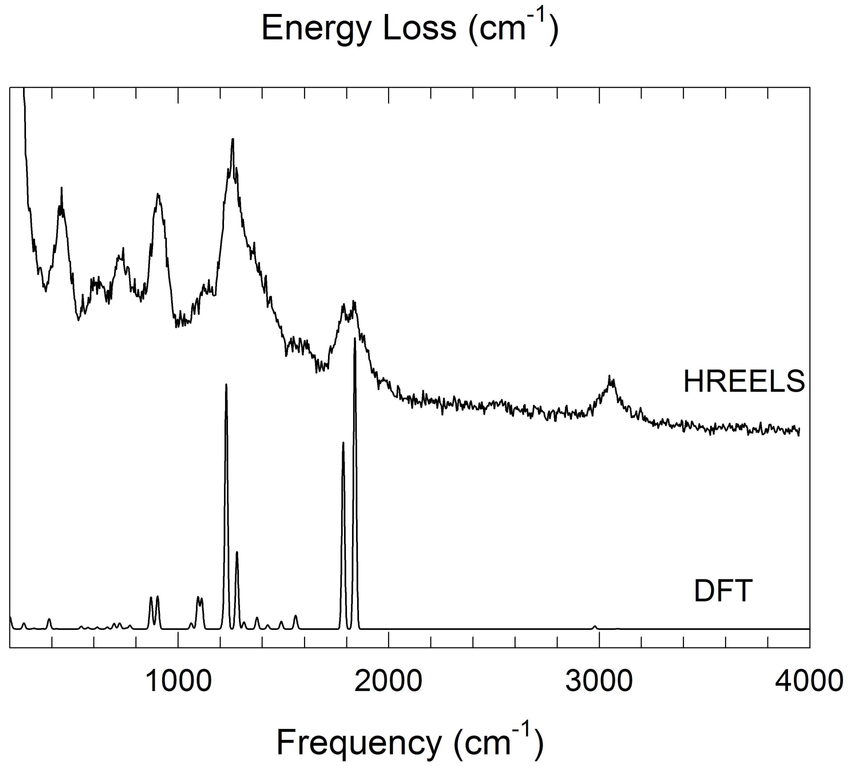

Figure 4.12: IR spectrum of PMDA adsorption on Cu(111) computed using B3LYP/LANL2DZ/6-31g(d). The HREEL spectrum for PMDA adsorption on Cu(111) at room temperature is also provided.

4.6 Conclusions.

Density functional theory has been used to determine the optimized geometries, harmonic vibrational frequencies and adiabatic electron affinities of maleic anhydride, phthalic anhydride, and pyromellitic dianhydride and their respective anions. The vertical electronic excitation energies for phthalic anhydride and pyromellitic dianhydride have been computed using time-dependent density functional theory. I have found there to be very good agreement in the predicted structures. The computed harmonic vibrational frequencies for maleic anhydride and phthalic anhydride are within about 4% of the experimental values. The consideration of anharmonic effects will likely improve the agreement between the theoretical and experimental values. The computed harmonic frequencies for PMDA were not as good, deviating from the experimental values by about 13%. This disagreement can be attributed to geometrical differrences between the idealized D_{2h} symmetry assumed in the calculation and the actual space group symmetry C_{4h}^4 of the crystalline material. Better predictions of the harmonic frequencies can be obtained by determining the optimized stucture of the crystalline lattice. The computed adiabitic electron affinities (AEA) for the three molecules predict the formation of stable anions upon electron attachment. Very accurate AEAs have been computed for maleic anhydride and phthalic anhydride by using the OLYP or OB95 XC functional and aug-cc-pVTZ triple-ζ quality basis set augmented with diffuse functions. The best estimation for the AEA of PMDA was in error by about +0.5 eV using the BHLYP/aug-cc-pVTZ. The over-estimation of the AEA for

PMDA is attributed to the over-binding or localization of charge on the anhydride groups that results in larger contributions to the self-interaction error persistent in DFT functionals. The vertical excitation energies for phthalic anhydride and PMDA and their respective anions have been calculated to be within about 0.2 eV of their observed experimental values. Both anions are characterized by a change in the position of the first excited state transition energy expected to fall in the visible region of the spectrum.

While the results for the gas phase molecules may be termed as “quantitative”, the results for the cluster models for the adsorption of water and PMDA on Cu(111) are “qualitative” at best. Water is predicated to adsorb in a tilted orientation ranging from 55 - 80 degrees. Estimation of the binding energies by all theoretical accounts range between -10 kJ/mol to about -40 kJ/mol. The best experimental estimates place the binding energy near -40 kJ/mol. The optimized geometry for the adsorption of PMDA on Cu(111) has been determined for the first time. An up-right geometry, which corresponds to the room temperature adsorbate structure, predicts the long C_2 axis of the intact portion of the molecule to be tilted away from the surface normal by about 49 degrees compared to the experimentally estimated value of about 60 degrees. The short C_2 axis is tilted away from the surface normal by about 5.5 degrees and the surface carboxylate group is bonded inequivalently to the surface.

Chapter 5

Co-adsorbate interactions on Cu(111)

5.1 Co-adsorption of H_2O with PMDA at 110K.

HREEL spectra of 0.01L of H_2O adsorbed on Cu(111) at 110 K and a 7Å thick film of PMDA co-adsorbed on a H_2O pre-covered surface are depicted in Figure 5.1. On clean Cu(111), water adsorption at 110K leads to the observation of the bulk librational modes peaked at 700 cm^{-1}, H-O-H scissor modes at 1630 cm^{-1}, and the O-H stretching modes between 3200-3700 cm^{-1}. At coverages $<$ 1 monolayer (ML) and growth temperatures below 140K [124], water forms amorphous 2D-clusters on the surface for ambient H_2O exposures in the range of 0.2-2.4L (1ML $\approx$ 4L). The expanded region shown in the inset of Figure 5.1 shows the O-H stretching region in an expanded view. The solid lines are drawn over the raw data (circles) only to provide a guide to aid in interpretation. The broad peak centered at 3400 cm^{-1} is identified as the "associated" (hydrogen bonded) O-H stretching mode while the sharp peak at 3650 cm^{-1} is identified as the "free" (non hydrogen bonded) O-H stretching mode at the edge of the clusters.

Spectrum *b* of Figure 5.1 illustrates the influence of Cu(111) surface pre-dosed with 0.01L H_2O on the vibrational structure of the 7Å thick PMDA film. The co-adsorbate layer is characterized by the out-of-plane ϕ(C-C) mode (395 cm^{-1}), γ(C=O) (718 cm^{-1}), ν_{as}(COC) (914 cm^{-1}), the carboxylate C-O bond stretch (1240 cm^{-1}), and the broad peak at 1740 cm^{-1} associated with the C=O moiety on the β-carbon. As observed on the "dry" surface, the absence of appreciable dipole activity between 1750-1875 cm^{-1} for the ν(C=O) stretching modes suggest a predominantly parallel adsorption geometry. The C-H and O-H stretching vibrations are expanded in the inset of Figure 5.1. The "free" O-H mode (3650 cm^{-1}) can no longer be resolved in the co-adsorbate spectrum. An additional peak of medium weak intensity is observed at 1440 cm^{-1} that was not present in the pure PMDA spectrum. Small shifts are observed in the peak positions of γ(C=O) (718, +8 cm^{-1}) and ν_{as}(COC) (914, -6 cm^{-1}) which are attributable to changes in the local electronic environment of the chemisorbate. This subtle observation suggests that water adsorption either directly or indirectly (substrate mediated) alters the charge population on the remaining intact anhydride group.

The influence of trace amounts ($< 1\%$ ML) of co-adsorbed H_2O on the structural orientation of ultra-thin PMDA films may be regarded as *subtle* at best. Even for a pristine single crystal substrate, it is generally assumed that the concentration of naturally occurring atomic defect sites is on the order of 1-5% of the surface. Thus, I characterize the ultra-low concentration of surface waters as "molecular" defect sites. Spectral assignment of the HREELS data is complicated due to significant overlap of the vibrational bands and limited resolution of the instrument. For water exposures greater than 0.5L,

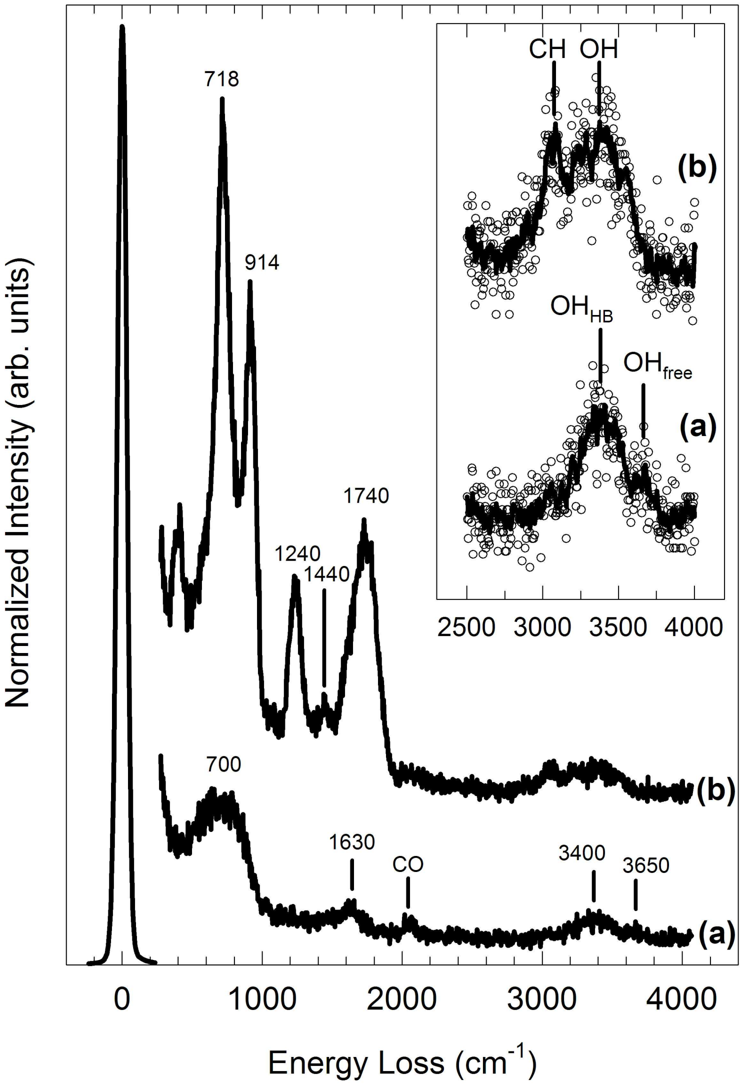

Figure 5.1: HREEL spectra of the (a) Cu(111) surface pre-covered with ∼ 0.01L H_2O and (b) a 7Å thick PMDA film co-adsorbed on (a). An expanded view of the C-H an O-H loss region is provided in the inset.

the measured loss spectra are completely dominated by the H_2O bands and no vibrational modes associated with PMDA can be observed.

It is apparent from Figure 5.1 that some preferential adsorption occurs at the edges of the surface water clusters as evidenced by the apparent quenching or red-shifting of the "free" O-H mode. I can imagine at least two possibilities for the observed loss of intensity for that O-H feature during the complexation of H_2O with PMDA on Cu(111): one in which PMDA hydrogen-bonds with edge O-H groups through the carboxylate, or one in which PMDA extracts a proton to form a surface carboxylic acid (R-COOH).

I shall begin by ruling out the possibility that a surface carboxylic acid (R-COOH) is formed due to a low temperature reaction between PMDA and H_2O. Carboxylic acids are generally characterized by O-H , C=O, and C-O stretching modes and C-OH bending modes. The infrared vibrational frequencies of these bands are also sensitive to environmental effects such as bonding orientation, dimer formation with another carboxylic acid, hydrogen bonding with other groups, and the electron donating or accepting ability of the R-group. For the gas phase monomer [65], the O-H stretching mode is observed as a sharp peak of medium intensity at 3570-3585 cm^{-1}. There is a strong C=O stretching mode at 1760-1780 cm^{-1} and a medium intensity C-O mode at 1115-1180 cm^{-1}. The C-OH in-plane bending mode is typically found at 1335-1385 cm^{-1} with medium weak intensity.

I cannot distinguish the O-H stretching mode of the -COOH group from the "free" O-H modes of the pure H_2O clusters. Similarly, I cannot distinguish the C=O stretch of a -COOH (1760-1780 cm^{-1}) group from the 1740 cm^{-1} band of PMDA. This is not surprising considering that the concentration of H_2O is on the order of 1% of a mono-layer. Even if every surface H_2O reacts with a PMDA molecule to form the acid, the remaining 99% of the "unreacted" PMDA molecules will contribute significant intensity to the loss spectrum. On the other hand, I note that there is no dipole activity in Figure 5.1 characteristic of the carboxylic acid C-O (1115-1180 cm^{-1}) stretching and C-OH (1335-1385 cm^{-1}) bending modes.

Furthermore, I have yet to identify the 1440 cm^{-1} peak in Figure 5.1. No vibrational modes exist in that region for the monomeric -COOH group, although a band at 1395-1440 cm^{-1} is characteristic of the C-OH bending mode in hydrogen-bonded carboxylic acid dimers. For carboxylic acid dimers, the O-H stretching band is observed at 3000 cm^{-1}, thus would be superimposed on any C-H modes in that region. The C-H modes are clearly separated from the O-H band shown in the inset of Figure 5.1 and no apparent broadening or increase in relative intensity is observed. Moreover, the best band for identifying -COOH dimers would be a broad, medium intensity band at 875-960 cm^{-1} a characteristic of $\mathrm{OH}\cdots\mathrm{H}$ out-of-plane bending modes. However, since I am unable to identify the existence of the -COOH dimer spectral features or loss features associated with the -COOH monomer, I have concluded that the surface reaction between PMDA and H_2O does not readily occur at 110K.

A more reasonable model where PMDA interacts with co-adsorbed H_2O by forming a hydrogen bonded surface complex with the carboxylate group is postulated. In this case, the interpretation of the co-adsorbate HREEL spectrum in Figure 5.1 becomes rather trivial. A small fraction of adsorbing PMDA bonds at the edges of the H_2O defect sites. Following the ring-opening reaction, the carboxylate group hydrogen-bonds to the “free” O-H groups which results in the observation of the 1440 cm^{-1} loss feature in Figure 5.1 which I attribute to the ν_s(OCO) stretching mode. The accompanying anti-symmetric ν_{as}(OCO) stretching mode at 1530-1580 cm^{-1} is unresolved in the broad 1740 cm^{-1} band. Evidently, the carboxylate-H_2O interaction results in more equivalent C-O bond lengths and red-shifts the “free” O-H frequency into the broad “associated” O-H band at 3400 cm^{-1}. The shift in the peak positions of the out-of-plane γ(C=O) mode (718 cm^{-1}) and anti-symmetric anhydride ring ν_{as}(COC) mode (914 cm^{-1}) are suggestive of an electronic perturbation induced by the complexation with H_2O. From the DFT calculation of harmonic frequencies for PMDA and the PMDA anion (see Tables 4.5 and 4.6), qualitative agreement is demonstrated by observing that the b_{3u} γ(C=O) mode increases in frequency (+2 cm^{-1}) while the b_{1u} anti-symmetric ν_{as}(COC) mode decreases in frequency (-50 cm^{-1}) upon the formation of the anion.

In general, PMDA adsorption on clean surfaces proceeds by the following simple reaction scheme

$$\mathrm{M} + \mathrm{C_{10}H_2O_6} \rightarrow \mathrm{M^+C_{10}H_2O_6^-}$$

where the metal M = Ag, Cu, Ni. Water adsorption on metals results in a lowering of the surface potential by raising the Fermi energy of the substrate and results in an increase of negative charge at the metal/vacuum interface [125]. As such, some of the metal electron density spills further into the vacuum and can interact with other adsorbed molecules in the vicinity of this local perturbation. I have already demonstrated that anhydrides in general are good electron acceptors, and PMDA in particular may be considered to be a very good electron acceptor with an experimental electron affinity around 2 eV [88]. Thus, in the presence of excess negative charge that may result from the polarization of the the substrate electron density at atomic or molecular defect sites, the probability of electron attachment to PMDA is likely to be greater than zero. The low temperature bonding geometry prefers the flat-lying, π-bonded orientation which places the π^* orbitals of the anhydride carbonyl groups in close proximity to the surface. It was shown from the DFT calculations in the preceding chapter that excess charge will localize in the C=O π^*-orbitals, hence this bonding orientation will be favorable for the formation of a stable surface anion at the H_2O "defect" sites. Therefore, I attribute the subtle changes in the HREEL spectrum of PMDA condensed in the presence of co-adsorbed H_2O to an increase in electron transfer from the substrate atoms involved in the PMDA chemisorption bond to the PMDA "surface ligand". Since the net amount of charge that is transferred during chemisorption is not known at this time, I prefer to represent the reaction scheme using partial charges such that

$$\mathrm{Cu_{surface}} + (\mathrm{H_2O})_\mathrm{n} + \mathrm{C_{10}H_2O_6} \rightarrow (\mathrm{Cu}^{\delta+}\mathrm{C_{10}H_2O_6^{\delta-}}) \cdot (\mathrm{H_2O})_\mathrm{n}$$

where the adsorption of PMDA on Cu(111) pre-covered with sub-monolayer coverages of H_2O is characterized as a mixture of hydrogen-bonded H_2O-PMDA and non-hydrogen bonded chemisorbed PMDA. Due to the extremely low H_2O concentration, the predominant surface species may be attributed to PMDA chemisorbed on the "non-doped" portions of the surface, and thus makes the largest contribution to the loss spectrum.

5.2 On the nature of SERS-CT of PMDA/Cu(111).

Up to this point, I have not made any reference to the previous work regarding the surface enhanced Raman scattering (SERS) and charge transfer excitations for mono-layer thick films of PMDA adsorbed on Cu(111) and Cu(100) [17–19]. Those surface Raman experiments demonstrated a resonant type behavior inferred by the observation of an enhanced scattering cross-section when exciting the adsorbate-substrate complex at 647nm. Electronic absorption experiments performed by EELS revealed an intense, narrow transition at 1.9 eV, nearly matching the laser excitation wavelength of the SERS data. The 1.9 eV excitation was assigned to a charge transfer resonance and correlated with photon-induced dynamical charge transfer (DCT) between PMDA and the copper substrate [17]. This was the first published account of the observation of SERS-CT excitations on an "atomically smooth" metal surface although the idea has been and continues to be invoked for SERS of molecules adsorbed on roughened electrodes and cold-deposited Cu films [127]. The enhancement observed for the PMDA/Cu systems was ultimately attributed to the so-called “first-layer” chemical enhancement mechanism of SERS [48].

As I have pointed out in the previous chapters, I have suspected that the previously observed CT excitations observed by EELS were due to the presence of co-adsorbed water. The electronic excitation spectra for clean Cu(111), PMDA adsorbed on clean Cu(111) at 110K, and PMDA adsorbed in the presence of co-adsorbed H_2O on Cu(111) at 110K are shown in Figure 5.2.

The HREEL spectra shown in Figure 5.2 demonstrate a most remarkable effect. In the absence of H_2O, I observe the typical PMDA electronic excitations at 4.1, 4.8, and 5.9 eV. The presence of pre-condensed H_2O exactly reproduces the 1.9 eV charge transfer resonance spectrum observed in the experiments by Ivanecky et al. I have also studied the evolution of the PMDA electronic excitations as a function of water exposure which is shown in Figure 5.3.

It is not until I have doped the surface with very low concentrations of H_2O that the charge transfer resonance is observed as evidenced in Figures 5.2 and 5.3. As little as 0.001L has to be exposed to the substrate prior to condensing PMDA in order to observe the 1.85 eV resonance. It should also be noted that the pre-covered H_2O surface alone does not cause the spectral changes the I observe. Clearly, this effect is due to the intimate relationship between H_2O, PMDA, and the surface.

These new results clearly imply that H_2O is necessary for the observa-

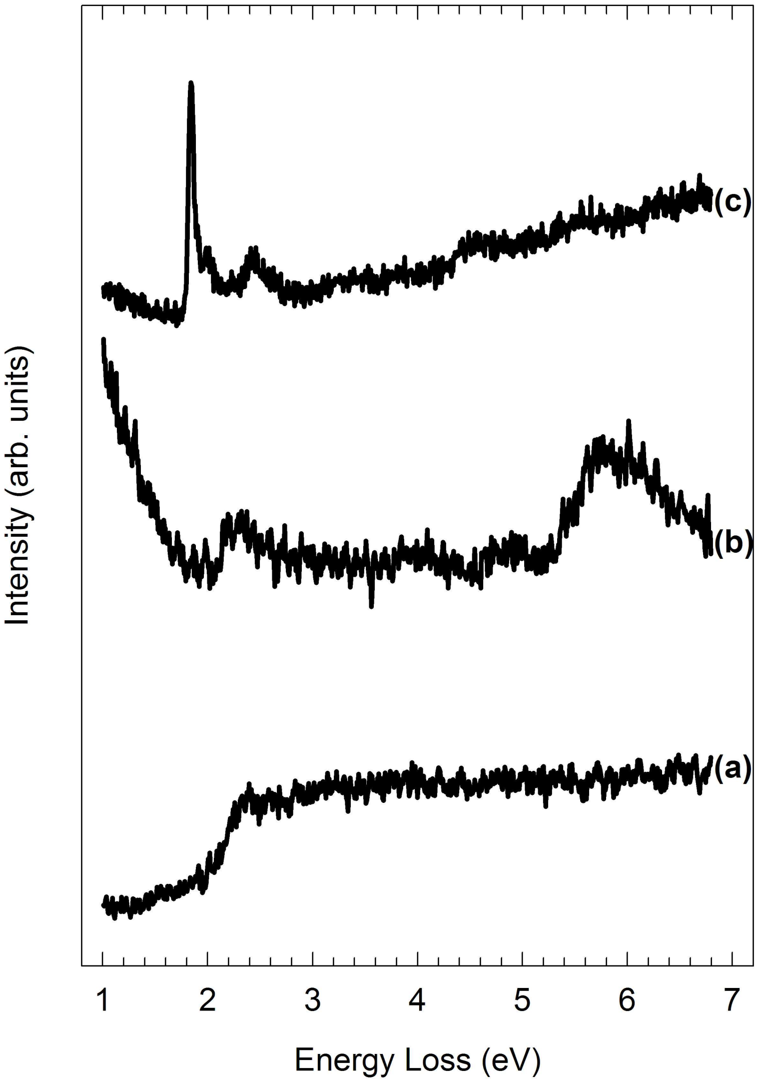

Figure 5.2: HREEL spectra of the (a) clean Cu(111) at 110K, (b) PMDA adsorption on clean Cu(111) at 110K, and (c) a 7Å thick PMDA film co-adsorbed with H_2O on Cu(111) at 110K.

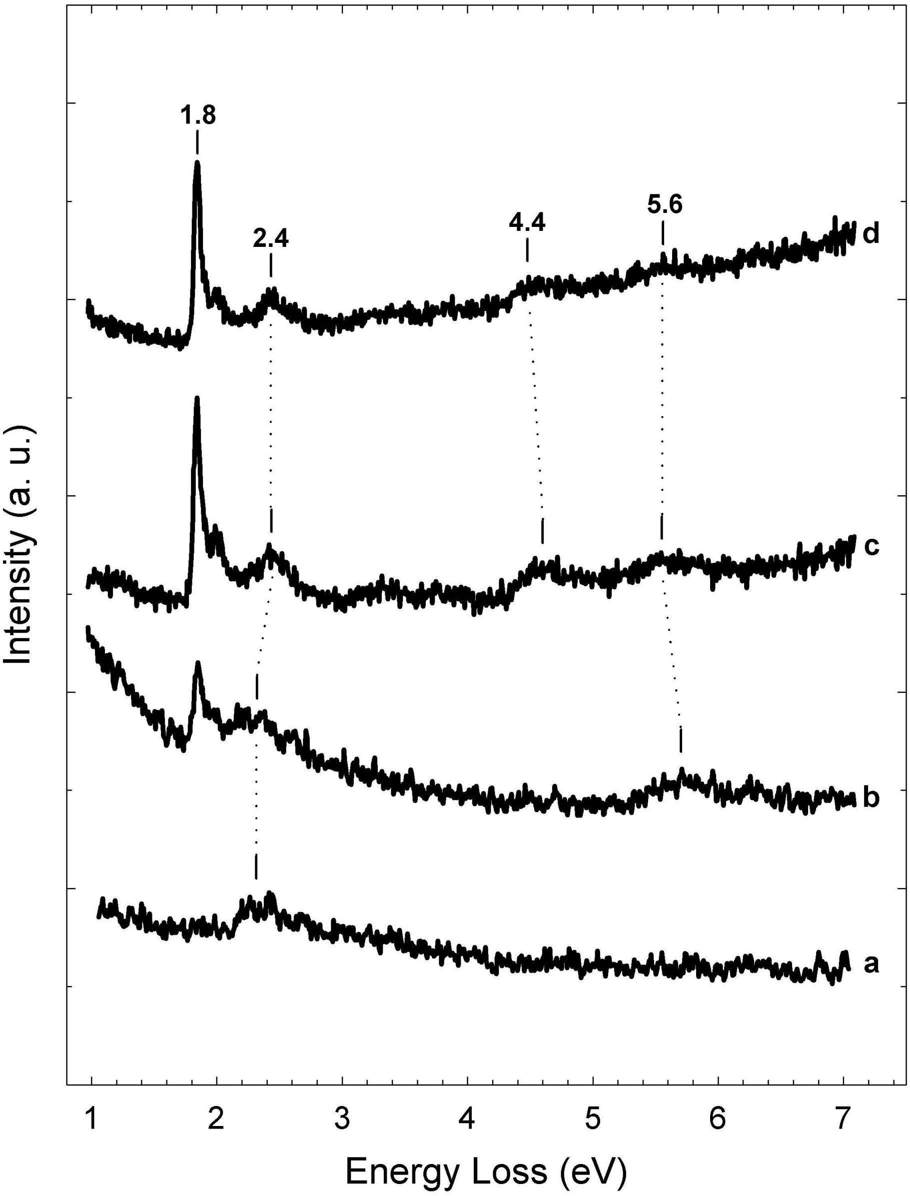

Figure 5.3: Electronic excitation spectral evolution demonstrating the "activation" of the surface PMDA anion. A 4Å thick PMDA film condensed at 110K with (a) 0.001L H_2O, (b) 0.01L H_2O, (c) 0.05L H_2O, and (d) 0.09L H_2O on a clean Cu(111) surface.

tion of SERS from PMDA adsorbed on copper surfaces. Indeed, this is evident in the surface Raman spectra recorded for PMDA adsorbed with increasing coverages of H_2O as shown in Figure 5.4. Again, I am able to exactly reproduce the SERS work of Ivanecky [17] and later Kambhampati [18, 19] if I "dope" the surface with very low concentrations of H_2O. The adsorption of H_2O apparently activates the Raman scattering of PMDA adsorbed on Cu(111) at 110K. The Raman vibrational modes for PMDA/Cu(111) have already been assigned on the basis that the surface was not doped with H_2O. Table 5.1 summarizes the Raman vibrational peak assignments.

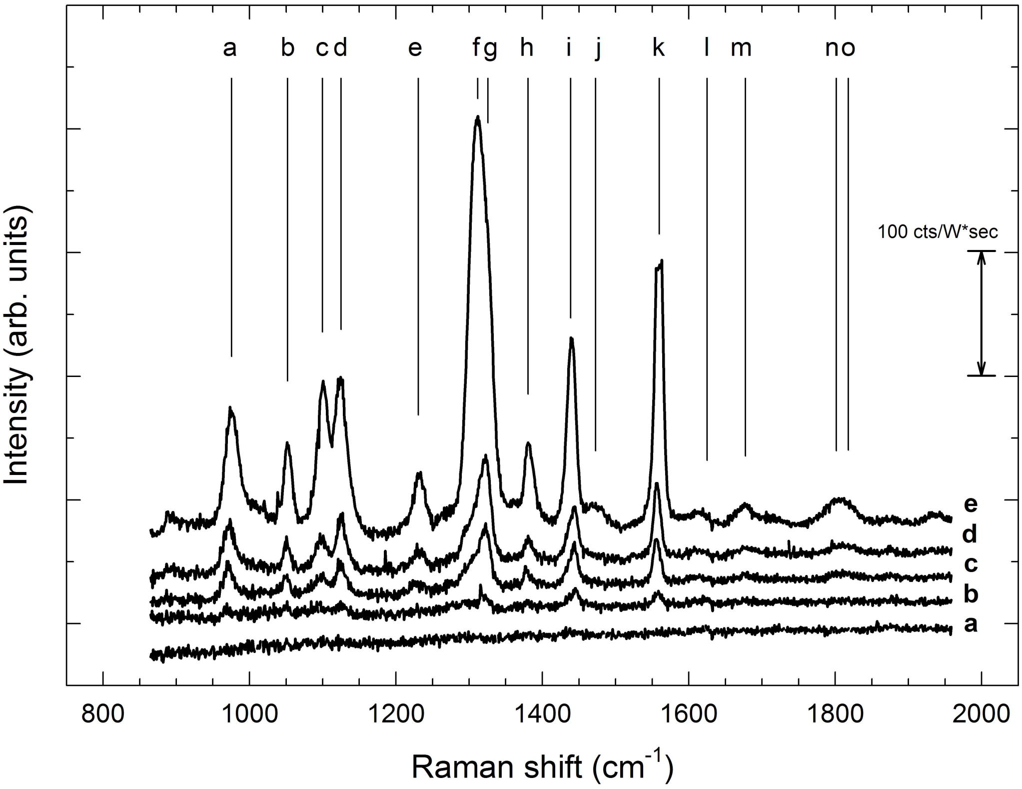

Figure 5.4: Surface enhanced Raman spectra of PMDA adsorption on Cu(111) co-adsorbed with (a) 0.00L H_2O, (b) 0.05L H_2O, (c) 0.10L H_2O, (d) 0.15L H_2O, and (e) $\sim$ 2-4L H_2O. The laser excitation wavelength was 647.2nm (50-100 mW) and all spectra were acquired in 600 sec scans with the luminescent background subtracted.

Table 5.1: Surface Raman vibrational mode assignments for PMDA co-adsorbed with H_2O on Cu(111) at 110K.

Peak	Freq. (0.15L H_2O)	Freq. (2-4L H_2O)	Assignment	PMDA [63]
a	973	977	ν(C-O)	937, R, b_{3g}
b	1051	1052	δ(C-H)	1075, IR, b_{2u}
c	1099	1100	ν(C-C)	1119, IR, b_{2u}
d	1125	1124	ν(C-C)	1132, R, a_g
e	1231	1232	-	-
f	1305	1307	ν(C-O)	1305, R, a_g
g	1323	1324	ν(C-C)	1329, R, b_{3g}
h	1381	1381	ν(C-C)	1373, IR, b_{1u}
i	1442	1439	ν_s(OCO)	$\cdots$
j	-	1470	-	-
k	1557	1559	ν_{as}(OCO)	$\cdots$
l	1609	1608	ν(C-C)	1627, R, a_g
m	1680	1677	-	-
n	1806	1798	ν_{as}(C=O)	1775, IR, b_{1u}
o	1824	1818	ν_{as}(C=O)	1790, R, b_{3g}

I have also attempted to measure the Raman spectrum of PMDA adsorbed on Cu(111) at room temperature "on resonance" and have yet to obtain a detectable signal. However, this result is not unexpected since H_2O does not adsorb on Cu(111) at room temperature. Moreover, I have established that the room temperature PMDA adsorption geometry favors an upright orientation. In experiments where PMDA was initially adsorbed at room temperature and subsequently cooled to 110K and exposed to H_2O, SERS is not observed. This implies that the initial orientation of PMDA is crucial for the SERS-CT mechanism. The flat-lying, π-bonded geometry that is observed at low temperature allows for efficient electronic coupling of the substrate and chemisorbed PMDA. It is also an indication that the H_2O-PMDA interaction is a "substrate-mediated" process. Additional evidence for the substrate-mediated charge transfer process is provided in Figure 5.5. The upper panel of Figure 5.5 demonstrates the *molecular* adsorption of PMDA in a thick ice surface grown on Cu(111) at 110K. The metal substrate-PMDA interaction is removed, while the PMDA-H_2O interactions remain present. Remarkably, PMDA does not undergo the now well-documented anhydride ring opening reaction noted by the conspicuous absence of the surface carboxylate modes in the upper panel that are present in the lower panel at 1442 cm^{-1} and 1557 cm^{-1}. Comparing the total Raman scattering intensities, it is quite evident that the PMDA-copper interaction is necessary for the observation of SERS and the direct interaction between the "solvent" water molecules and PMDA is less important than the direct interaction of PMDA with the substrate.

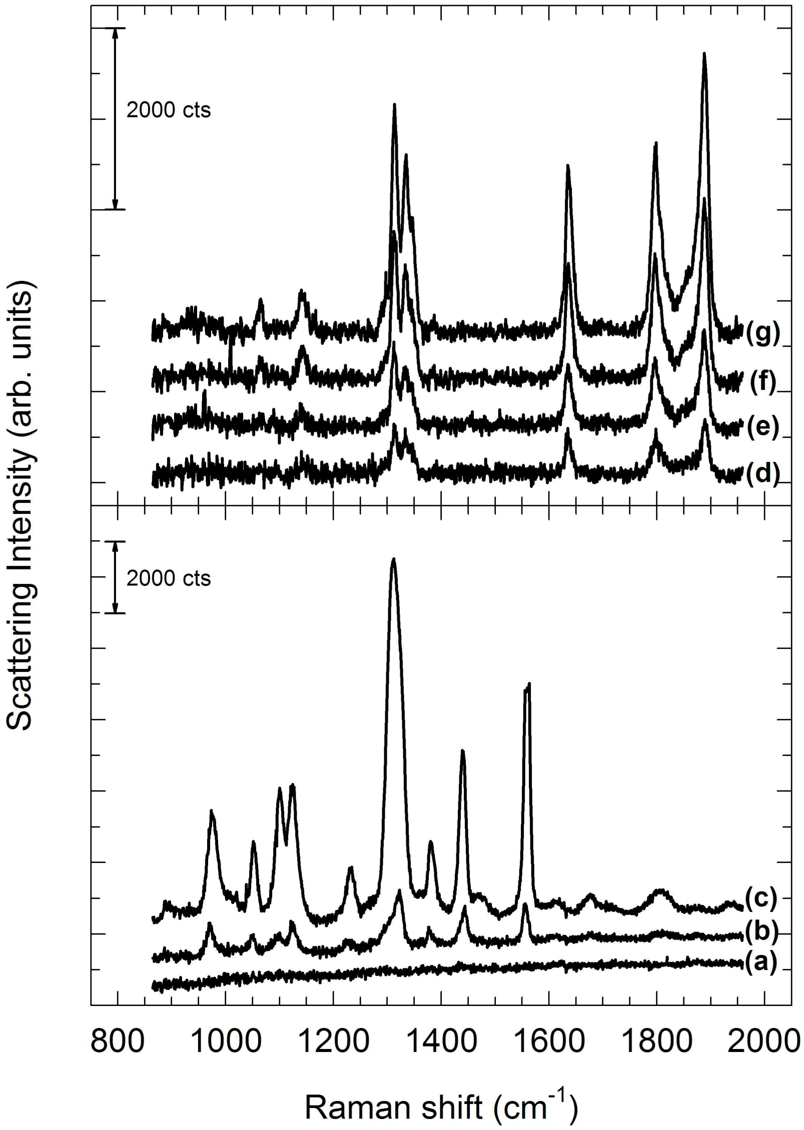

Figure 5.5: Lower Panel: Surface Raman spectra of PMDA co-adsorbed at 110K with (a) 0.00L H_2O, (b) 0.10L H_2O, and (c) 2-4L H_2O. Upper panel: Surface Raman spectra of increasing exposures of PMDA condensed on a 30L H_2O/Cu(111) surface. The coverages correspond to approximately (a) submonolayer, (b-c) monolayer, and (d) multilayer PMDA films. PMDA condenses on the ice surface molecularly.

I have shown that the observed HREEL spectra of the co-adsorbate system were largely due to the undoped regions of the PMDA films. On the other hand, we observe the opposite effect in the surface Raman experiments! The data presented in Figure 5.4 clearly demonstrate that, under resonant scattering conditions, surface Raman spectroscopy is indeed quite sensitive to the local chemical and electronic structure of defect site chemistry on single crystal surfaces.

5.3 Discussion.

I now turn our discussion to the underlying chemical physics of the SERS phenomenon for the H_2O-PMDA/Cu(111) system. Somehow, we must be able to provide a reasonable explanation for the role that H_2O plays in this complicated many-body problem. Central to our understanding is the so-called charge transfer resonance at 1.85 eV in the energy loss data. Does the presence of such extremely low concentrations of H_2O produce the necessary "atomic scale roughness" proposed by Otto [21] to prevent the dephasing of optical currents at the surface so that dynamical charge transfer between the copper and PMDA may take place? Perhaps this is true, since, the resonant charge transfer excitation at 1.85 eV is not observed for PMDA on clean, 'atomically smooth' Cu(111). However, if I condense PMDA on a sputter-damaged surface, I do not observe the 1.85 eV resonance. I have also considered that H_2O adsorption might induce elastic deformations of the substrate atoms thereby roughening the surface, however, we have yet to find any experimental evidence in the literature to support such a claim. Furthermore, I can hardly imagine that sub-monolayer H_2O coverages even come close to the RMS roughness produced by the cold-deposited copper films studied by the Otto group although I will agree that the "surface" is indeed "smooth" without adsorbed water. However, it is not the physical roughness that is important but rather the induced electronic roughness by virtue of a electronic polarization of the substrate charge density. Therefore, it is unlikely that a physical surface roughness contributes to the observed SERS of the PMDA co-adsorbed with H_2O on Cu(111) at 110K.

Now consider the effect of H_2O adsorption on the copper surface electronic structure. It has already been established that sub-monolayer coverages have a low activation energy for desorption on the order of 50-59 kJ/mol [124]. Small binding energies correspond to physisorbed systems and the adsorbate-substrate interactions are generally due to Van der Waals attractive forces. Little or no orbital mixing is involved between the adsorbate and surface, hence little or no charge is transferred at the time of adsorption. Since H_2O is a polar molecule, it affects the local surface potential by raising the Fermi energy through the formation of a surface dipole layer and is characterized by a decrease in the work function of the surface [49].

In the case of a chemisorbed molecule where a direct bond (either ionic or covalent) is formed, the energy levels of the molecule are shifted and broadened. Additionally the potential barrier between the surface and adsorbate is greatly reduced. If the affinity level of the adsorbate lies below E_{fermi}, then generally it is believed that charge flows from the metal to the adsorbate. On the other hand, if the affinity level lies above E_{fermi}, then charge is transferred to the metal from the adsorbate. Of course, this schematic approach does very little in terms of understanding the true nature of the charge transfer excitations on Cu(111) from a state-to-state point of view. Therefore, it is necessary to try to understand what molecular orbitals are involved in the coupled H_2O/PMDA/Cu(111) complex.

An energy level diagram is provided in Figure 5.6 that illustrates the relative orbital alignments of the copper cluster models and gas phase PMDA This simple diagram is very informative. As usual, electrons occupy states up to the Fermi level of the metal. A reasonable measure of the cluster quality is to compare the energy of the HOMO level of the cluster to the work function of the real surface. For Cu(111), the experimental work function is 4.94 eV [117] comparing favorably with the DFT predicted value of 4.13 eV. The adsorption of H_2O on the cluster results in an increase of the calculated Fermi level energy to -3.89 eV (+0.24 eV) which is in qualitative agreement with experimental findings. It is interesting to observe the position of the LUMO and other affinity levels of gas phase PMDA in relation to the Fermi energy of the H_2O/Cu_{10} cluster. The LUMO of PMDA is found energetically to be more or less degenerate with the HOMO of the Cu_{10} cluster and below the HOMO of the H_2O/Cu_{10} cluster.

Based on the previous discussion, I would expect additional charge to be transferred from the metal to adsorbed PMDA forming a surface anion

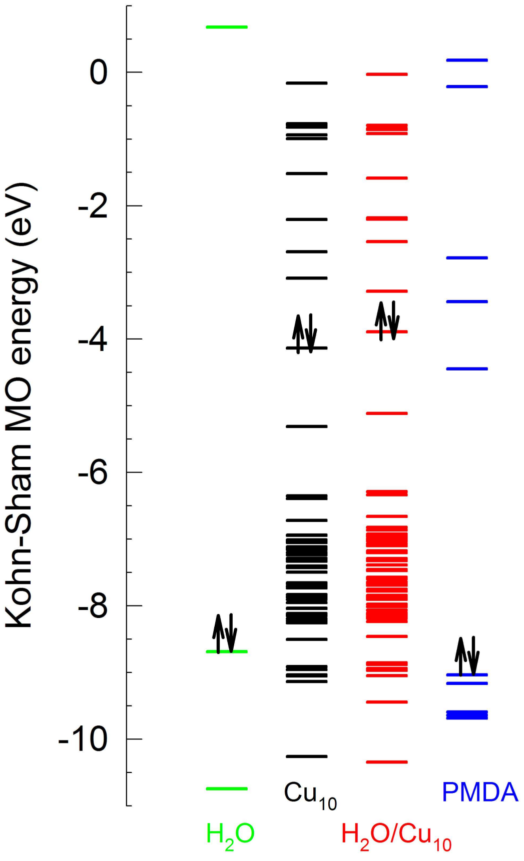

Figure 5.6: Energy level diagram derived from the Kohn-Sham orbitals for H_2O, Cu_{10}, Cu_{10}-H_2O, and PMDA.

during the chemisorption process in the presence of co-adsorbed H_2O. The resulting chemisorbate complex formed at the H_2O defects sites may then be regarded as an inorganic charge transfer complex of the form

$$\mathrm{Cu}^{\delta+}\mathrm{C}_{10}\mathrm{H}_2\mathrm{O}_6^{\delta-}$$

One should also expect that additional polarization of the charge transfer complex by increasing the negative charge population on the surface ligand would influence the intensity of the CT resonance. This would be the equivalent of increasing the negative potential on the electrode in the SERS electrochemical experiments. An analogous phenomenon is demonstrated in the H_2O coverage dependent study shown in Figure 5.3. A similar result may be obtained by changing the “molecular defect” to one that may be regarded as a better electron-donor, e.g. pyridine. By co-adsorbing pyridine with PMDA on Cu(111) at 110K, I observe similar electronic structure to the H_2O experiment as evidenced in Figure 5.7. Interestingly, in the 1960 study by Ferstandig [100] of molecular charge-transfer complexes of PMDA, he found there to be no interaction between pyridine and PMDA. The resulting absorption spectrum of the PMDA-pyridine complex was characteristic of the absorption of neutral PMDA. The results of Figure 5.7 demonstrate the formation of a charge-transfer complex for the condensed phase co-adsorbate system providing additional evidence for substrate-mediated charge transfer facilitating the formation of a surface anion of chemisorbed PMDA.

For alkali metal-benzoate salts [65], the carboxylate group vibrational

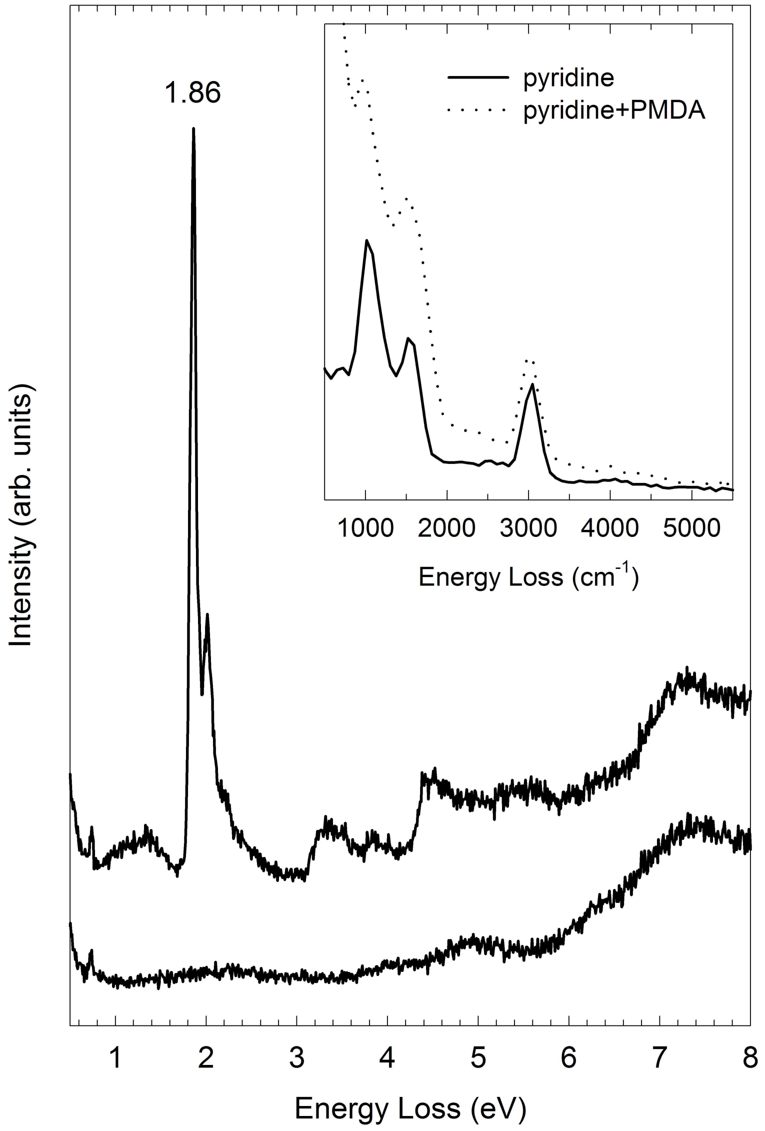

Figure 5.7: HREEL spectrum demonstrating the influence on the PMDA electronic excitation spectra with the co-adsorption of pyridine.

frequencies are observed at 1552-1561 cm^{-1} for the anti-symmetric ν_{as}(OCO) stretch and at 1380-1427 cm^{-1} for the symmetric ν_s(OCO) stretch, thus providing a reasonable explanation for the observation of similar bands in our HREEL and Raman spectra. The flat-lying adsorption geometry of PMDA also allows for a favorable interaction of the π^* orbitals localized on the anhydride ring with the polarized substrate charge density.

I seek to provide some insight as to the nature of the 1.85 eV charge transfer excitation responsible for the "first layer" SERS effect. The surface species, $\mathrm{Cu}^+\mathrm{C}_{10}\mathrm{H}_2\mathrm{O}_6^-$, appears in the form of a classic donor-acceptor charge transfer complex. Returning to the energy level diagram of Figure 5.6, there are several metal cluster affinity levels within 2 eV of the LUMO of PMDA which may act as electron acceptor states upon photo-excitation. However, there are also additional empty affinity levels that are localized on the isolated PMDA molecule which may serve as an electron acceptor state.

Dynamical charge transfer is generally discussed with respect to metal-adsorbate photon induced charge transfer, however, one should not limit the discussion to charger-transfer between just metal and adsorbate. Essentially, any photon induced redistribution of charge either inter- or intramolecular in nature should also be considered to be a dynamical process if it leads to normal coordinate displacements in the excited state. Hence, based on the simple diagram of Figure 5.6, I cannot yet rule out the possibility that the observed SERS-CT mechanism for PMDA adsorption originates from an intra-molecular excitation of the surface anion. The current results seem to point towards the formation of a stable surface anion and the SERS-CT mechanism is due to resonance Raman scattering from the intra-molecular electronic excitation of the anion. In the past, empty metal states or image potential states were believed to be involved and the SERS-CT was attributed to a molecule-to-metal CT excitation [18, 19]. Recent, 2PPE experiments [125] for D_2O/Cu(111) clearly indicate that the energetic position of the first image potential state is located at 2.9 eV above the Fermi level which is clearly well above the 1.9 eV SERS-CT energy. Considering the stark similarities in the experimental absorption spectrum of PMDA anion with the current EELS electronic excitation spectra for the co-adsorbate complex, it is more likely that the observed SERS for PMDA adsorbed on Cu(111) is due to the resonant excitation of a PMDA surface anion.

5.4 Conclusions.

The vibrational and electronic excitation spectra of ultrathin (2-12Å) PMDA films chemisorbed on clean and H_2O pre-covered Cu(111) surfaces at 110K have been measured using HREELS and surface Raman spectroscopy. Adsorption of PMDA on both surfaces at 110K is characterized by a ring-opening reaction of one of the anhydride groups producing a mono-dentate carboxylate and carbonyl moiety. The remaining anhydride ring is unperturbed and favors a flat-lying surface orientation. Sub-monolayer coverages of H_2O act a ‘molecular’ defect sites which alter the local structure of the carboxylate group through hydrogen bonding effects. The presence of H_2O

lowers the surface potential barrier allowing for electron transport across the interface from the Fermi level of the substrate to the lowest unoccupied MO of PMDA during chemisorption at 110K. The resulting surface complex may be regarded as a hydrated inorganic charge-transfer complex of the form

$$(\mathrm{H_2O})_n(\mathrm{Cu}^{\delta+}\mathrm{PMDA}^{\delta-}_{ads}).$$

The interaction between H_2O and PMDA on Cu(111) at 110K dramatically influences electronic excitation spectrum of PMDA characterized by an intense, narrow charge transfer resonance at 1.85 eV. Surface Raman experiments exhibit an enhanced scattering cross-section when exciting the co-adsorbate system at 647.2 nm which is attributed to the SERS-CT mechanism where a resonant Raman scattering process occurs due to an electronic transition to the first excited state of the chemisorbed PMDA surface anion. Observation of the SERS-CT state provides direct evidence for the so-called "first layer" SERS effect for nanometer thick PMDA films chemisorbed in the presence of H_2O. Indeed, the phenomenon is truly "chemical" in nature due to both the hydrogen-bonding interaction between chemisorbed PMDA and surface water cluster and the polarization of the substrate charge density by submonolayer coverages of H_2O facilitating the formation of a stable surface anion from chemisorbed PMDA. Photo-induced charge transfer is believed to proceed via

$$(\mathrm{Cu}^{\delta+}\mathrm{C_{10}H_2O_6^{\delta-}})\cdot(\mathrm{H_2O})_\mathrm{n} + \mathrm{h}\nu \rightarrow (\mathrm{Cu}^{\delta+}\mathrm{C_{10}H_2O_6^{*\delta-}})\cdot(\mathrm{H_2O})_\mathrm{n}$$

where the laser excitation energy of 1.92 eV is pre-resonant with the SERS-CT state observed by EELS at 1.85 eV.

Appendices

Appendix A

PMDA adsorption on Ag(111) at 110K

The adsorption of PMDA on a clean Ag(111) surface at 110K is shown in Figure A.1. As with PMDA adsorption on Cu(111) at 110K, five distinct vibrational losses are observed at 395, 714, 992, 1210 and 1795 cm^{-1}, increasing in intensity as the film thickness is varied. The first three features are readily identifed as the out-of-plane phenyl ring b$_{3u}$ defomation mode ϕ(C-C), the out-of-plane C=O deformation b$_{3u}$ mode γ(C-O), and the anti-symmetric anhydride ring b$_{1u}$ stretching mode ν_{as}(COC) of the parent molecule [63]. The medium intensity feature observed at 1210 cm^{-1} is assigned to the in-plane ν(C-C) b$_{2u}$ stretching mode which is shifted by about -28 cm^{-1} from the parent peak. At higher coverages, a weak feature near 1620 cm^{-1} can be assigned to the totally symmetric phenyl a$_g$ ring breathing mode ν(C-C). The strong peak centered at 1795 cm^{-1} is identified as the anti-symmetric carbonyl b$_{3g}$ stretching mode ν(C=O). A weak activation at 3048 cm^{-1} is observed at higher coverages in the C-H stretching region.

The above observations indicate the PMDA enjoy a similar π-bonded adsorption geometry on Ag(111) as on the Cu(111) surface, however, evidence for dissociative chemisorption has yet to be identified. Absent are the fre-

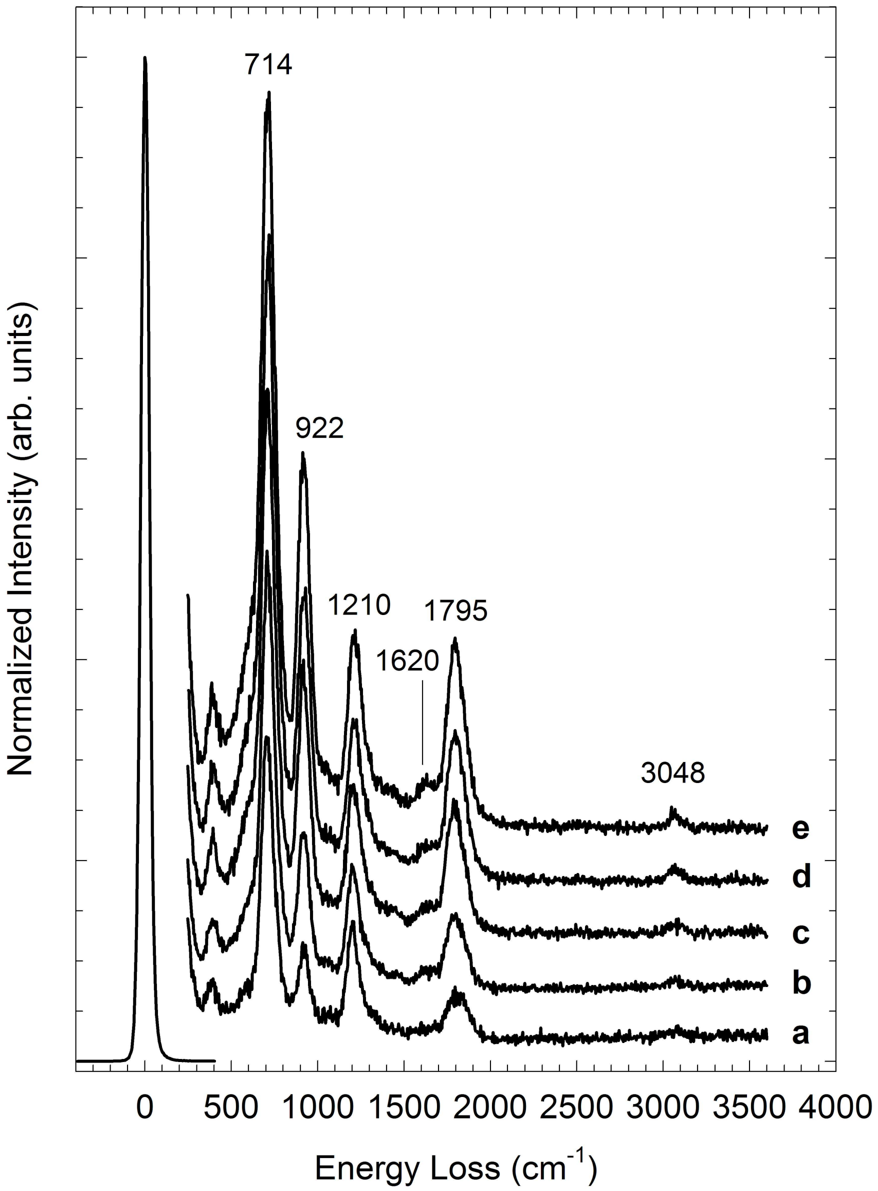

Figure A.1: HREEL spectra of pyromellitic dianhydride adsorption on Ag(111) at 110K. The corresponding coverages are (a) 1Å, (b) 3Å, (c) 5Å, (d) 8Å, and (e) 10Å.

quencies corresponding to surface carboxylate formation (1240 and 1640 cm^{-1} loss features observed on Cu(111)) as is the 1740 cm^{-1} band attributed to the C=O moiety at the β-position on the phenyl ring. Apparently, PMDA is less reactive on the silver surface at 110K, although it is noted that the π-interaction between the phenyl ring and metal electrons is stronger evidenced by the moderate red-shift of the in-plane ν(C-C) b_{2u} stretching mode (1210 cm^{-1}) and weak activation of the phenyl ring breathing mode (1620 cm^{-1}).

Although a thorough vibrational study of the co-adsorption of H_2O with PMDA on Ag(111) has yet to be perfomed, the influence of H_2O co-adsorption with PMDA on the surface electronic structure was surveyed. The electronic excitations of PMDA co-adsorbed with 0.09L H_2O on clean Ag(111) at 110K are shown in Figure A.2. The CT excitation is clearly observed at 1.85 eV on the Ag(111) surface implying that the previously observed SER spectrum for PMDA adsorption on Ag(111) [20] also results from co-adsorbate interactions on the surface. The relatively weaker vibronic peak seems to also suggest that the electronic coupling between the substrate and π-system of the adsorbate are stronger which leads to a decrease in the lifetime of the excited state.

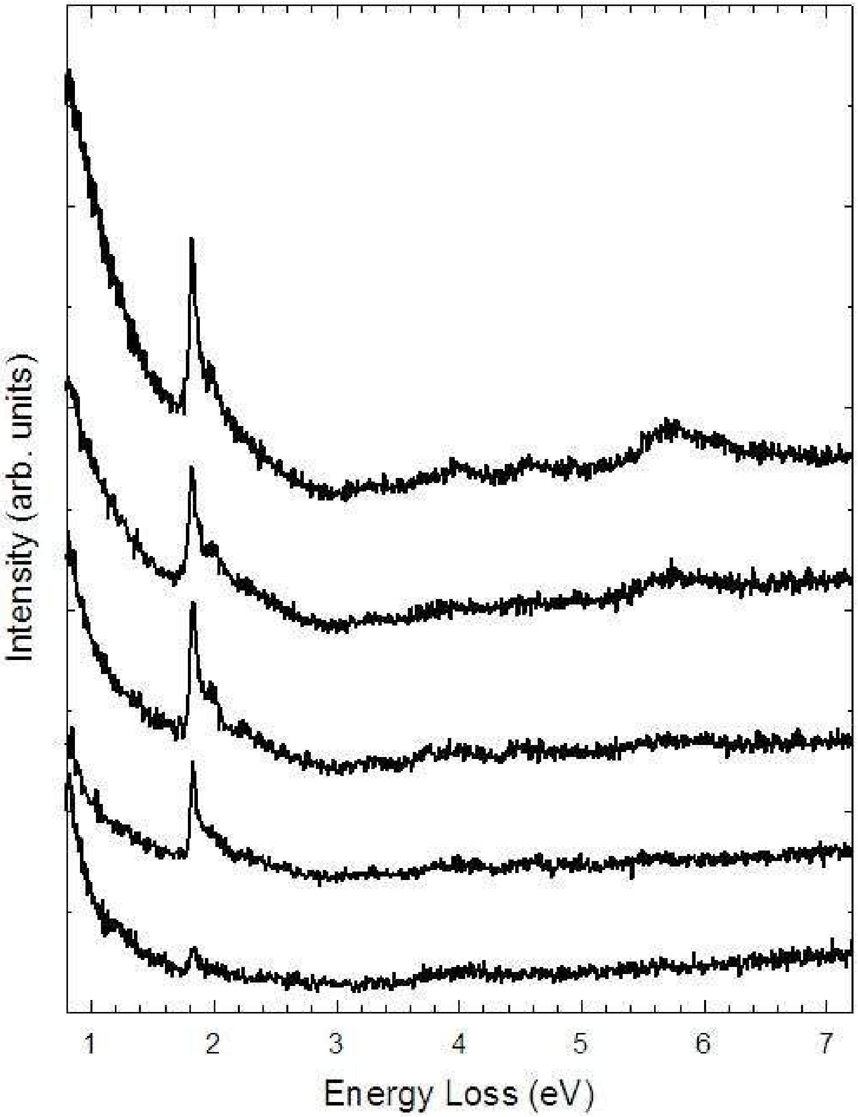

Figure A.2: HREEL spectra of pyromellitic dianhydride co-adsorption with 0.09L H_2O on Ag(111) at 110K. The corresponding PMDA coverages are (a) 1Å, (b) 3Å, (c) 5Å, (d) 8Å, and (e) 10Å.

Appendix B

The surface loss function

From the the theory of electron energy loss spectroscopy, it is well known that electrons are scattered inelastically by long-wavelength (optical) charge density fluctuations of the solid [128–130]. Therefore information regarding the complex dielectric constant, $\epsilon\,(q,\omega)$, may in priciple be determined from such experiments. Here, I have defined the dielectric constant in terms of wave vector, q, and frequency, ω. A general treatment for electron-surface interactions in the context of electron scattering processes has been presented by Mills [128–130]. According to the theory by Mills, the differential inelastic scattering cross-section in atomic units for small-angle scattering (dipole loss regime) from a semi-infinite solid is given by

$$\begin{aligned}\frac{d^2S}{d\Omega d\omega} &= \frac{m^2e^2v_\perp^2}{2\pi\cos\theta}\frac{k_s}{k_I} \\ &\times\frac{|v_\perp q_\parallel(R_s+R_I)+i(R_I-R_s)\left(\omega-\boldsymbol{v}_\parallel\cdot\boldsymbol{p}_\parallel\right)|^2}{q_\parallel^2\left[v_\parallel^2q_\parallel^2+\left(\omega-\boldsymbol{v}_\parallel\cdot\boldsymbol{p}_\parallel\right)^2\right]^2} \\ &\times P(\boldsymbol{q}_\parallel,\omega) \qquad \text{(B.1)}\end{aligned}$$

where $P(\boldsymbol{q}_\parallel,\omega)$ is the surface structure factor. In Equation B.1, R_s and R_I are defined as the complex elastic reflection coefficients for the diffraction-loss and loss-diffraction processes, respectively, $v_\parallel$ and $v_\perp$ define the parallel and perpendicular components of the initial electron velocity, and k_I and k_s are the electron wave vector before and after the inelastic event. The angle of incidence, θ, is measured relative to the surface normal.

For scattering from charge density fluctuations outside of a semi-infinite crystal occupying the half-space of $z < 0$ with complex frequency dependent $\epsilon(\omega)$, it has been shown that [128–130] for energy loss events with $\hbar\omega \gg k_B T$,

$$P(\boldsymbol{q}_{\|}, \omega) = \frac{2}{\pi} \Im \left(\frac{-1}{1 + \epsilon(\omega)} \right) \tag{B.2}$$

where the "surface loss function" is expressed as $\Im\left(\frac{-1}{1+\epsilon(\omega)}\right)$. The exciation of "bulk" losses is described by the 'bulk loss function" $\Im\left(\frac{-1}{\epsilon(\omega)}\right)$. For most scattering geometries, excluding grazing incident angles, it known that "bulk" and "surface" losses make approximately equal contributions to the scattering cross-section of Equation B.1.

Now, it is relatively trivial to express the energy loss functions in terms of the complex index of refraction, N, and use the experimenal frequency dependent optical paramters to plot the loss functions as a function of excitation energy. Expressing the complex frequency dependent dielectric function in terms N, we have

$$\epsilon(\omega) = \epsilon_1 + i\epsilon_2 = (n^2 - k^2) + i(2nk) \tag{B.3}$$

and expanding the following

$$\begin{aligned} \frac{-1}{1 + \epsilon(\omega)} &= \frac{-1 - \epsilon_1 + i\epsilon_2}{(1 + \epsilon_1)^2 + (\epsilon_2)^2} \\ &= \frac{-1 - (n^2 - k^2) + i2nk}{\left[1 + (n^2 - k^2)\right]^2 + 4n^2k^2} \end{aligned} \tag{B.4}$$

where $N = n + ik$ is the complex index of refraction. Therefore the surface loss function expressed in terms of n and k is simply

$$\Im\left(\frac{-1}{1+\epsilon(\omega)}\right) = \frac{2nk}{\left[1+(n^2-k^2)\right]^2 + 4n^2k^2}. \tag{B.5}$$

The calculated surface and bulk loss functions for silver and copper are plotted in Figures B.1 and B.2.

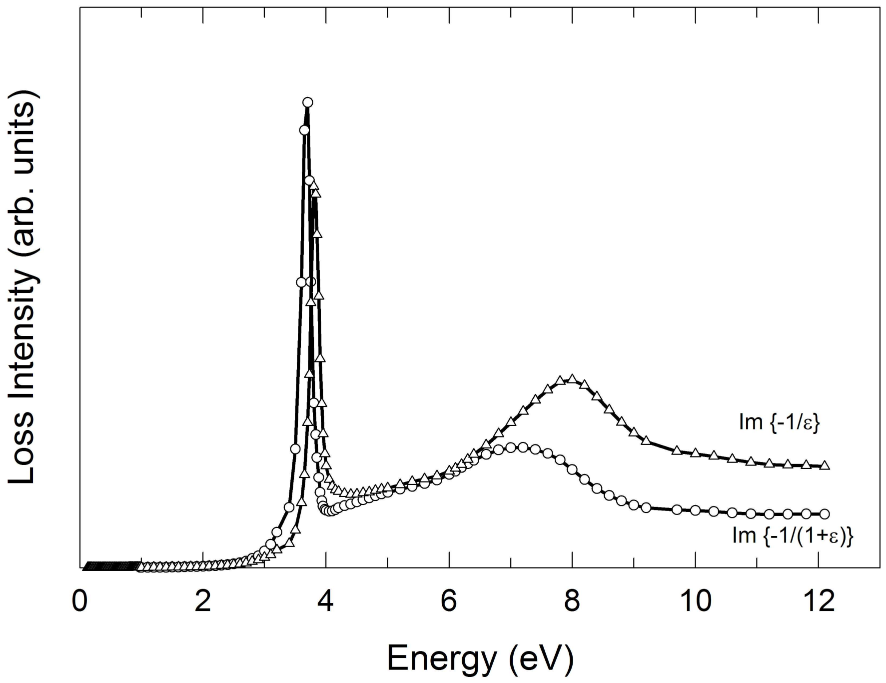

Figure B.1: Theoretical bulk and surface optical energy loss functions for silver determined from the experimental optical constants found in reference [131].

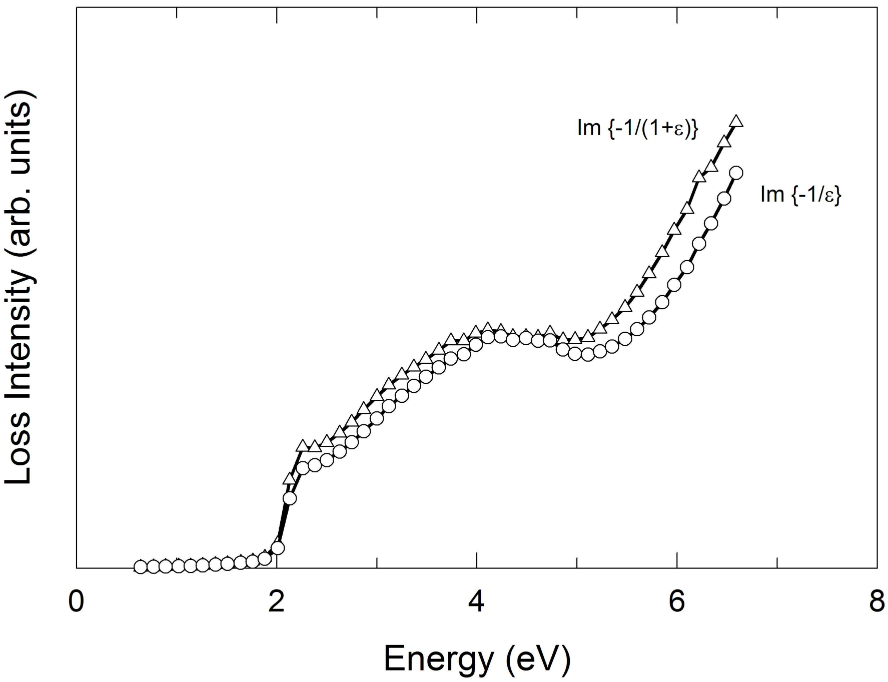

Figure B.2: Theoretical bulk and surface optical energy loss functions for silver determined from the experimental optical constants found in reference [131].

Bibliography

[1] Fleischmann, M.; Hendra, P. J.; McQuillan, A. J. *Chem. Phys. Lett.* **1974,** *26,* 163.

[2] Jeanmaire, D. L.; Duyne, R. P. V. *J. Am. Chem. Soc.* **1975,** *97,* 1699.

[3] Jeanmaire, D. L.; Duyne, R. P. V. *J. Electroanal. Chem* **1977,** *84,* 1.

[4] Albrecht, M. G.; Creighton, J. A. *J. Am. Chem. Soc.* **1977,** *99,* 5215.

[5] Albrecht, M. G.; Creighton, J. A. *Electrochim. Acta* **1978,** *23,* 1103.

[6] Moskovits, M. *J. Chem. Phys.* **1978,** *69,* 4159.

[7] Furtak, T. E. *Solid State Commun.* **1978,** *28,* 903.

[8] Pettinger, B.; Wenning, U. *Chem. Phys. Lett.* **1978,** *56,* 253.

[9] Pettinger, B.; Wenning, U.; Kolb, D. M. *Ber. Bunsenges. Phys. Chem.* **1978,** *82,* 1326.

[10] Campion, A.; Kambhampati, P. *Chem. Rev.* **1998,** *27,* 241.

[11] Otto, A. *Appl. Surf. Sci.* **1980,** *6,* 300.

[12] Persson, B. N. J. *Chem. Phys. Lett.* **1981,** *82,* 561.

[13] Arya, K.; Zeyher, R. *Phys. Rev. B: Condens. Matter* **1981,** *24,* 1852.

[14] Demuth, J. E.; Sanda, P. N. *Phys. Rev. Lett.* **1981,** *47,* 57.

[15] Billmann, J.; Kovacs, G.; Otto, A. *Surf. Sci.* **1980,** *92,* 153.

[16] Ivanecky, III, J. E.; Child, C. M.; Campion, A. *Surf. Sci.* **1994,** *325,* L428.

[17] Campion, A.; Ivanecky, III, J. E.; Child, C. M.; Foster, M. *J. Am. Chem. Soc.* **1995,** *117,* 11807.

[18] Kambhampati, P.; Child, C. M.; Campion, A. *J. Chem. Soc., Faraday Trans.* **1996,** *92,* 4775.

[19] Kambhampati, P.; Child, C. M.; Foster, M. C.; Campion, A. *J. Chem. Phys.* **1998,** *108,* 5013.

[20] Kambhampati, P.; Song, O. K.; Campion, A. *Phys. Stat. Sol. A* **1999,** *175,* 233.

[21] Otto, A. *Phys. Stat. Sol. A* **2001,** *188,* 1455.

[22] Zangwill, A. *Physics at Surfaces;* Cambridge University Press: Cambridge, 1988.

[23] Davis, L. E.; MacDonald, N. C.; Palmberg, P. W.; Riach, G. E.; Weber, R. E. *Handbook of Auger Electron Spectroscopy;* Physical Electronics Industrusies, Inc.: New York, 1978.

[24] Palmberg, P. W. *Anal. Chem.* **1973,** *45,* 549A.

[25] Penn, D. R. *Phys. Rev. B: Condens. Matter* **1976,** *13,* 5248.

[26] Ibach, H.; Mills, D. L. *Electron Energy Loss Spectroscopy and Surface Vibrations;* Academic Press: New York, 1982.

[27] Roy, D.; Carrete, J. D. *Appl. Phys. Lett.* **1970,** *16,* 413.

[28] Gadzuk, J. W. Excitation Mechanisms in Vibrational Spectroscopy of Molecules on Surfaces. In *Vibrational Spectroscopy of Molecules on Surfaces*; Yates, Jr., J. T.; Madey, T. E., Eds.; Plenum Press: New York, 1987.

[29] Palmer, R. E.; Rous, P. J. *Rev. Mod. Phys.* **1992,** *64,* 383.

[30] Moskovits, M. *Rev. Mod. Phys.* **1985,** *57,* 783.

[31] Pettinger, B. In Situ Raman Spectroscopy at Metal Electrodes. In *Adsorption of Molecules at Metal Electrodes*; Lipkowski, J.; Ross, P. N., Eds.; VCH Publishers: New York, 1992.

[32] Moskovits, M. *J. Chem. Phys.* **1982,** *77,* 4408.

[33] Mullins, D. R.; Campion, A. *J. Phys. Chem.* **1988,** *88,* 8.

[34] Lombardi, J. R.; Birke, R. L.; Lu, T.; Xu, J. *J. Chem. Phys.* **1986,** *84,* 4174.

[35] Jiang, J. D.; Burstein, E.; Kobayashi, H. *Phys. Rev. Lett.* **1986,** *87,* 1793.

[36] Yamada, H.; Nagata, H.; Toba, K.; Nakao, Y. *Surf. Sci.* **1987,** *182,* 269.

[37] Rosenberg, A.; DiLella, D. P. *Chem. Phys. Lett.* **1994,** *223,* 76.

[38] Osawa, M.; Matsuda, N.; Yoshii, K.; Uchida, I. *J. Phys. Chem.* **1994,** *98,* 12702.

[39] Rubim, J. C.; Corio, P.; Ribiero, M. C. C.; Matz, M. *J. Phys. Chem.* **1995,** *99,* 15765.

[40] Arenas, J. F.; Wooley, M. S.; Otero, J. C.; Marcus, J. I. *J. Phys. Chem.* **1996,** *100,* 3199.

[41] Arenas, J. F.; Tocon, I. L.; Otero, J. C.; Marcus, J. I. *J. Phys. Chem.* **1996,** *100,* 9254.

[42] Brolo, A. G.; Irish, D. E.; Lipkowski, J. *J. Phys. Chem. B* **1997,** *101,* 3906.

[43] Kudelski, A.; Burkowski, J. *Chem. Phys. Lett.* **1996,** *253,* 246.

[44] Avouris, P.; Demuth, J. E. *J. Chem. Phys.* **1981,** *75,* 4783.

[45] Adrian, F. J. *J. Chem. Phys.* **1982,** *77,* 5302.

[46] Ueba, H. *Surf. Sci.* **1983,** *129,* L267.

[47] Ueba, H. *Surf. Sci.* **1983,** *131,* 347.

[48] Mrozek, I.; Otto, A. *Appl. Phys. A* **1989,** *49,* 389.

[49] Desjonquères, M. C.; Spanjaard, D. *Concepts in Surface Physics;* Springer-Verlag: Berlin, 2nd ed.; 1996.

[50] Creighton, J. A. *Surf. Sci.* **1986,** *173,* 665.

[51] Perry, S. S.; Campion, A. *Surf. Sci.* **199,** *234,* L275.

[52] Perry, S. S.; Campion, A. *Surf. Sci.* **1991,** *259,* 207.

[53] Grunze, M.; Lamb, R. N. *Surf. Sci.* **1988,** *204,* 183.

[54] Mainka, C.; Wegner, H.; Schertel, A.; Wöll, C.; Grunze, M. *Zeit. für Phys. Chem.* **1997,** *198,* 221.

[55] Hahn, C.; Strunskus, T.; Grunze, M. *J. Phys. Chem.* **1994,** *98,* 3851.

[56] Ashton, M. R.; Jones, T. S.; Richardson, N. V.; Mack, R. G.; Unertl, W. N. *J. Elec. Spectr. Rel. Phenom.* **1990,** *54/55,* 1133.

[57] Richardson, N. V.; Frederick, B. G.; Unertl, W. N.; Farrach, A. E. *Surf. Sci.* **1994,** *307,* 124.

[58] Haq, S.; Bainbridge, R. C.; Frederick, B. G.; Richardson, N. V. *J. Phys. Chem. B* **1998,** *102,* 8807.

[59] Frederick, B. G.; Richardson, N. V.; Unertl, W. N.; Farrash, A. E. *Surf. Int. Anal.* **1993,** *20,* 434.

[60] Frederick, B. G.; Ashton, M. R.; Richardson, N. V.; Jones, T. S. *Surf. Sci.* **1993,** *292,* 33.

[61] Haq, S.; Richardson, N. V. *J. Phys. Chem. B* **1999,** *103,* 5256.

[62] Bartecki, A.; Skoze, J.; Varsanyi, G.; Vizesy, M. *Absorption Spectra in the Ultraviolet and Visible Region;* volume 20 Academic Press: New York, 1975.

[63] Hase, Y.; Kawai, K.; Sala, O. *J. Molec. Struct.* **1975,** *26,* 297.

[64] Boeyens, J. C. A.; Herbstein, F. H. *J. Phys. Chem.* **1965,** *69,* 2160.

[65] Lin-Vien, D.; Colthup, N. B.; Fateley, W. G.; Grasselli, J. G. *The Handbook of Infrared and Raman Characteristic Frequencies of Organic Molecules;* Academic Press: Boston, 1991.

[66] Dunning, T. H. *J. Chem. Phys.* **1971,** *55,* 3958.

[67] Huzinaga, S. *J. Chem. Phys.* **1962,** *42,* 1293.

[68] Dunning, T. H. *J. Chem. Phys.* **1970,** *53,* 2823.

[69] Lee, T. J.; Schaefer, H. F. *J. Chem. Phys.* **1985,** *83,* 1784.

[70] Dunning, T. H. *J. Chem. Phys.* **1989,** *90,* 1007.

[71] Woon, D. E.; Dunning, T. H. *J. Chem. Phys.* **1994,** *100,* 2975.

[72] Parr, R. G.; Yang, W. *Density-Functional Theory of Atoms and Molecules;* Oxford University Press: New York, 1989.

[73] Dreizler, R. M.; Gross, E. K. U. *Density Functional Theory: An Approach to the Quantum Many-Body Problem;* Springer-Verlag: Berlin, 1990.

[74] Koch, W.; Holthausen, M. C. *A Chemist's Guide to Density Functional Theory;* Wiley-VCH: Weinheim, 2000.

[75] Hohenberg, P.; Kohn, W. *Phys. Rev.* **1964,** *136,* B864.

[76] Kohn, W.; Sham, L. J. *Phys. Rev.* **1965,** *140,* A1133.

[77] Becke, A. D. *Phys. Rev. A* **1998,** *38,* 1988.

[78] Perdew, J. P. *Phys. Rev. B: Condens. Matter* **1986,** *33,* 8822.

[79] Lee, C.; Yang, W.; Parr, R. G. *Phys. Rev. B: Condens. Matter* **1988,** *37,* 785.

[80] Becke, A. D. *J. Chem. Phys.* **1993,** *98,* 5648.

[81] Frisch, M. J. *et al.* "Gaussian 03, Revision B.04", Gaussian, Inc., Wallingford, CT, 2004.

[82] Rogstad, A.; Klaboe, P.; Baranska, H.; Bjarnov, E.; Christensen, D. H.; amd O. F. Nielsen, F. N.; Cyvin, B. N.; Cyvin, S. J. *J. Molec. Struct.* **1974,** *20,* 403.

[83] Hase, Y.; Davanzo, C. U.; Kawai, K.; Sala, O. *J. Molec. Struct.* **1976,** *30,* 37.

[84] Mirone, P.; Chiorboli, P. *Spectrochim. Acta* **1962,** *18,* 1425.

[85] Lauro, C. D.; Califano, S.; Adembri, G. *J. Molec. Struct.* **1968,** *2,* 173.

[86] Foster, J. P.; Weinhold, F. *J. Am. Chem. Soc.* **1980,** *102,* 7211.

[87] Chen, E. C. M.; Chen, E. S. D. *The Electron Capture Detector and the Study of Reactions with Thermal Electrons;* John Wiley & Sons: Hoboken, 2004.

[88] Chen, E. C. M.; Wentworth, W. E. *J. Chem. Phys.* **1975,** *63,* 3183.

[89] Rösch, N.; Trickey, S. B. *J. Chem. Phys.* **1997,** *106,* 8940.

[90] Galbraith, J. M.; Schaefer, H. F. *J. Chem. Phys.* **1996,** *105,* 862.

[91] Rienstra-Kiracofe, J. C.; Graham, D. E.; Schaefer, H. F. *Molec. Phys.* **1998,** *94,* 767.

[92] Banerji, K. C. *Proc. Nat. Acad. Sci. India* **1956,** *Sect. A 25,* 115.

[93] Handy, N. C.; Cohen, A. J. *Molec. Phys.* **2001,** *99,* 403.

[94] Becke, A. D. *J. Chem. Phys.* **1996,** *104,* 1040.

[95] Casida, M. E. Time-Dependent Density Functional Response Theory for Molecules. In *Recent Advances in Density Functional Methods*, Vol. 1; Chong, D. P., Ed.; World Scientific: Singapore, 1995.

[96] Casida, M. E. Time-Dependent Density Functional Response Theory of Molecular Systems: Theory, Computational Methods, and Functionals. In *Recent Developments and Applications of Modern Density Functional Theory, Theoretical and Computational Chemistry*, Vol. 4; Seminario, J. M., Ed.; Elsevier: Amsterdam, 1996.

[97] Gross, E. K. U.; Kohn, W. *Adv. Quant. Chem.* **1990,** *21,* 255.

[98] http://webbook.nist.gov,.

[99] Shida, T.; Iwata, S.; Imamura, M. *J. Phys. Chem.* **1974,** *78,* 1974.

[100] Ferstandig, L. L.; Toland, W. G.; Heaton, C. D. *J. Am. Chem. Soc.* **1961,** *83,* 1151.

[101] Bernardo, C. G. P. M.; Gomes, J. A. N. F. *J. Molec. Struct.* **2003,** *629,* 251.

[102] Gomes, J. R. B.; Gomes, J. A. N. F.; Illas, F. *J. Molec. Catal. A: Chem.* **2001,** *170,* 187.

[103] Ignaczek, A.; Gomes, J. A. N. F. *J. Electroanal. Chem.* **1997,** *420,* 71.

[104] Wang, G.; Jiang, L.; Pang, X.; Cai, Z.; Pan, Y.; Zhao, X.; Morikawa, T.; Nakamura, J. *Surf. Sci.* **2003,** *543,* 118.

[105] Jiang, L.; Wang, G.; Cai, Z.; Pan, Y.; Zhao, X. *J. Molec. Struct.* **2004,** *710,* 97.

[106] Ruuska, H.; Pakkanen, T. A.; Rowley, R. L. *J. Phys. Chem. B* **2004,** *108,* 2614.

[107] Stener, M.; Fronzoni, G.; Francesco, R. D. *Chem. Phys.* **2005,** *309,* 49.

[108] Miletic, M.; Gland, J. L.; Hass, K. C.; Schneider, W. F. *Surf. Sci.* **2003,** *546,* 75.

[109] Almeida, A. L.; Martins, J. B. L.; Longo, E.; Taft, C. A.; Murgich, J.; Jalbout, A. F. *J. Molec. Struct.* **2003,** *664,* 111.

[110] Mikheeva, E. P.; Kachurovskaya, N. A.; Zhidomirov, G. M. *Kinet. Catal.* **2002,** *43,* 223.

[111] Lopez, N.; Illas, F. *J. Phys. Chem. B* **1998,** *102,* 1430.

[112] Okamura, K.; Ishii, H.; Kimura, Y.; Niwano, M. *Surf. Sci.* **2005,** *576,* 45.

[113] Nicholson, K. T.; B.Holl, M. M. *Phys. Rev. B: Condens. Matter* **2001,** *64,* 155317.

[114] Wang, Z. H.; Cao, Y.; Xu, G. Q. *Chem. Phys. Lett.* **2001,** *338,* 7.

[115] Casanovas, J.; Illis, F.; Pacchioni, G. *Chem. Phys. Lett.* **2000,** *326,* 523.

[116] Limtrakul, J.; Tantanak, D. *Chem. Phys.* **1996,** *208,* 331.

[117] Lide, D. R. *CRC Handbook of Chemistry and Physics;* CRC press: Boca Raton, 79th ed.; 1998.

[118] King, D. A.; Woodruff, D. P. *The Chemical Physics of Solid Surfaces, Phase Transitions, and Adsorbate Reconstructuring at Metal Surfaces;* volume 7 Elsevier: Amsterdam, 1994.

[119] Hay, P. J.; Wadt, W. R. *J. Chem. Phys.* **1985,** *82,* 270.

[120] Hariharan, P. C.; Pople, J. A. *Theoret. Chimica. Acta* **1973,** *28,* 213.

[121] Francl, M. M.; Petro, W. J.; Hehre, W. J.; Brinkley, J. S.; Gordon, M. S.; DeFree, D. J.; Pople, J. A. *J. Chem. Phys.* **1982,** *77,* 3654.

[122] Adamo, C.; Lelj, F. *J. Molec. Struct.* **1997,** *389,* 83.

[123] Thiel, P. A.; Madey, T. E. *Surf. Sci.* **1987,** *7,* 211.

[124] Hinch, B. J.; Dubois, L. H. *J. Chem. Phys.* **1992,** *96,* 3262.

[125] Bovensiepen, U.; Gahl, C.; Wolf, M. *J. Phys. Chem. B* **2003,** *107,* 8706.

[126] Ribarsky, M. W.; Leudtke, W. D.; Landman, U. *Phys. Rev. B: Condens. Matter* **1985,** *32,* 1430.

[127] Zylka, G.; Otto, A. *Surf. Sci.* **2001,** *475,* 118.

[128] Evans, E.; Mills, D. L. *Phys. Rev. B: Condens. Matter* **1972,** *5,* 4126.

[129] Evans, E.; Mills, D. L. *Phys. Rev. B: Condens. Matter* **1973,** *7*, 853.

[130] Mills, D. L. *Surf. Sci.* **1975,** *48*, 59.

[131] Palik, E. D. *Handbook of Optical Constants of Solids;* Academic Press: New York, 1985.

Vita

Robert Jason Scharff was born in Longview, Texas, the son of Davis Ladd Scharff and Marsha Ann Parsons on Novenber 18, 1971. He received the Bachelor of Science degree in Chemistry from The University of Texas at Austin (UT) in Austin, Texas, in 1994. At UT as an undergraduate, he performed research experiments for Professor Alan Campion regarding the adsorption and reaction of alkylsilanes on the silicon (100) surface using high-resolution electron energy loss spectroscopy. He began graduate studies in 1995 at the Univerity of Pittsburgh in Pittsburgh, Pennsylvania, and he received the Master of Science degree in Physical Chemistry in 1999. At Pittsburgh, his research was supervised by Professor John T. Yates, Jr., regarding the thermal and photochemical behavior of molecular oxygen adsorbed on the vicinal platinum (335) surface using temperature programmed desorption techniques and high-resolution electron energy loss spectroscopy. Although he was a doctoral candidate already, he left Pittsburgh and re-enrolled in the doctoral program at The Univerisity of Texas at Austin. Once more under the supervision of Professor Alan Campion, he worked on the role of co-adsorbate interactions at metal surfaces on surface-enhanced Raman scattering by the chemical enhancement mechanism using Raman scattering and high-resolution electron energy loss spectroscopy. In June of 2003, he married Jacqueline Marie Veauthier in Youngstown, OH, the daughter of Nicholas and JoAnn Veauthier. In

May 2005, he received the Doctor of Philosophy degree in Chemical Physics from The University of Texas at Austin and currently resides in Los Alamos, New Mexico.

Permanent address: 2111 34th Street, Unit B
Los Alamos, New Mexico 87544

This dissertation was typeset with LaTeX[†] by the author.

[†] LaTeX is a document preparation system developed by Leslie Lamport as a special version of Donald Knuth's TeX Program.